Longitudinal Momentum Distributions of ^{8}B and ^{19}C: Signatures for One-Proton and One-Neutron Halos

Thomas Baumann

Darmstadt, November 1999

19th November 1999

This is an updated version of the
"Inaugural Dissertation zur Erlangung
des Doktorgrades der Naturwissenschaften",
which was presented to the
Justus-Liebig Universität Gießen (Fachbereich Physik)
by Thomas Baumann in February 1999.

Zusammenfassung

Halo-Kerne sind ein besonderes Phänomen der Kernstruktur, das seit ein paar Jahren mit großem Interesse untersucht wird. Unter den vielen teilchengebundenen aber instabilen Kernen fallen die Halo-Kerne durch ihre ungewöhnlich große räumliche Ausdehnung auf. Halo-Kerne sind aus verschiedenen Gründen interessante Studienobjekte. Zum einen spielen sie eine wichtige Rolle bei der Erforschung der Grenzen der Teilchenstabilität, auf der anderen Seite sind sie die einzigen experimentell verfügbaren Systeme, an denen sich die Frage, wie sich Kernmaterie bei geringen Dichten verhält, untersuchen läßt.

Die Entdeckung dieser neuartigen Kernstruktur war erst durch die in den letzten Jahren entwickelten Anlagen zur Produktion und Separation von Strahlen exotischer, d.h. instabiler Kerne möglich [29, 27].

Die Nukleonen im Kern sind durch die Kernkraft gebunden, welche eine Reichweite hat, die etwa dem Durchmesser der Nukleonen entspricht. Aus diesem Grund sollten die Atomkerne recht kompakt oder aber ungebunden sein. Der Kern läßt sich in erster Ordnung durch freie Nukleonen in einem Potentialtopf beschreiben. Betrachtet man nun Kerne nahe der Protonen- oder Neutronen-Abbruchkante, die sehr schwach gebunden sind, so befinden sich Nukleonen an der oberen Grenze des Potentialtopfes. Hier treten besondere Phänomene auf, die der herkömmlichen Idee der Kernmaterie als inkompressible Flüssigkeit mit nahezu gleichbleibender Dichte widersprechen. Aufgrund der geringen Bindungsenergie können die Valenznukleonen nämlich in einen Bereich tunneln, der stark gebundenen Nukleonen nicht zugänglich ist. Dieses Phänomen wurde erstmals im ^{11}Li entdeckt und ist seit Ende der achtziger Jahre unter dem Begriff „Halo“ bekannt [36, 33, 66]. In diesem Sinn ist der Halo ein rein quantenmechanischer Effekt, der nur durch die Wahrscheinlichkeitsverteilung der Valenznukleonen im Ortsraum verstanden werden kann.

Ein Halo-Kern besitzt ein oder mehrere schwach gebundene Nukleonen, die einen Kern normaler Dichte (*Core-Nukleus*) mit einer räumlich ausgedehnten Wolke geringerer Dichte umgeben. Die Grundvoraussetzung für die Ausbildung eines Halos ist eine kleine Bindungsenergie der Valenznukleonen. Nur dann besteht eine Wahrscheinlichkeit, daß diese Teilchen zu großen Radien hinaus tunneln können. Darüberhinaus ist ein kleiner Bahndrehimpuls für die Schale, in der sich das Valenznukleon befindet, eine weitere Bedingung. Eine Zentrifugal-Barriere würde die Tunnel-

Wahrscheinlichkeit verringern. In gleichem Maße wirkt eine zusätzliche Coulomb-Barriere auf den Halo, weshalb Protonen-Halos weniger ausgeprägt sind.

Ausgeprägte Halo-Strukturen existieren jedoch in der Nähe der Neutronen-Abbruchkante. Zu den experimentell und theoretisch am besten untersuchten Halo-Kernen zählen der Zwei-Neutronen-Halo ^{11}Li und der Ein-Neutronen-Halo ^{11}Be. Diese Halo-Systeme lassen sich theoretisch sehr gut als Drei- bzw. Zwei-Teilchen-Cluster beschreiben, in denen ^{9}Li bzw. ^{10}Be den jeweiligen Core-Nukleus bilden. Bei den schwereren Kernen enfernt sich die Neutronen-Abbruchkante immer weiter von den stabilen Kernen, so daß hier mögliche Halo-Kerne bereits einen Core mit großem Neutronen-Überschuß haben. Der schwerste Halo-Kern, der bis jetzt experimentell nachgewiesen wurde, ist ^{19}C [14, 50, 13, 10].

Der Fall eines Protonen-Halos wurde erstmals im protonenreichen ^{8}B experimentell nachgewiesen [52, 70]. Dieser Kern liegt an der Protonen-Abbruchkante, und auch das nächst-schwerere Bor-Isotop, ^{9}B, ist ungebunden. Die Bindungsenergie des Valenzprotons im ^{8}B beträgt nur 137 keV – dies ist eine bemerkenswert schwache Bindung, selbst im Vergleich mit etablierten Neutronen-Halos wie ^{11}Be und ^{11}Li. Allerdings wurde der Protonen-Halo in ^{8}B kontrovers diskutiert, weil nicht alle nachfolgenden Experimente zwingend auf eine Halo-Struktur schließen ließen [55, 60].

Die schwach gebundenen Systeme ^{8}B und ^{19}C, die beide Ein-Teilchen-Halos sind, wurden anhand der experimentellen Bestimmung der longitudinalen Impulsverteilungen nach der Abspaltung des Halo-Nukleons bei relativistischen Energien untersucht. Diese Impulsverteilungen spiegeln die intrinsische Impulsverteilung des entfernten Nukleons wider. Über die Heisenbergsche Unschärferelation läßt sich von einer schmalen Impulsverteilung, wie sie für die Fragmente aus dem Aufbruch von Halo-Kernen gemessen wird, auf eine ausgedehnte räumliche Verteilung schließen.

Die Experimente wurden am Fragmentseparator der Gesellschaft für Schwerionenforschung durchgeführt [28]. Vom Schwerionen-Synchrotron SIS auf 1.0–1.5 GeV/u beschleunigte Primärstrahlen erzeugten durch Fragmentation in Beryllium-Produktionstargets die radioaktiven Sekundärstrahlen von ^{8}B und ^{19}C. Der Fragmentseparator wurde als zweistufiges Energieverlust-Spektrometer betrieben, in dessen dispersiver Mittelebene das Aufbruchtarget installiert war. Durch die Verwendung des Energieverlust-Modus kann die Impulsänderung, die durch die Aufbruchreaktion verursacht wird, trotz der um mehrere Größenordnungen größeren Impulsunschärfe des Sekundärstrahls gemessen werden.

Der Bestimmung der longitudinalen Impulsverteilung des ^{7}Be Core-Fragments aus dem Aufbruch von ^{8}B liegt, verglichen mit der ersten Untersuchung der Impulsverteilungen von Aufbruch-Fragmenten des ^{8}B [70], ein in mehreren Punkten verbessertes Experiment zugrunde. Es wurden im Rahmen dieser Doktorarbeit entwickelte ortsempfindliche Detektoren erstmals am FRS eingesetzt, die zu einer besseren Auflösung beitrugen. Der durch die Messung abgedeckte Impulsbereich wurde ausgedehnt, was die

Aussagekraft der Impulsverteilungen im Vergleich mit theoretischen Rechnungen entscheidend verbessert. Desweiteren konnte eine um ein Vielfaches verbesserte Statistik erziehlt werden. Zugleich wurden die alten Ergebnisse in den wesentlichen Punkten durch die neue Messung bestätigt.

Die longitudinale Impulsverteilung der ^{7}Be Fragmente aus dem Aufbruch von ^{8}B in einem Kohlenstoff-Target zeigt eine Breite (FWHM) von 95 ± 5 MeV/c. Die Form der Verteilung weicht sowohl von einem reinen Gauss-Profil als auch von einer Lorentz-Kurve ab. Im vorgestellten Experiment wurde parallel zu den Messungen der Impulsverteilung auch der partielle Wirkungsquerschnitt für den Ein-Protonen-Verlustkanal zu 98 ± 6 mb bestimmt. Dieser Wert ist mehr als fünfmal größer als der entsprechende Querschnitt für den stabilen Kern ^{10}B.

Theoretische Rechnungen, die von komplementären Ansätzen ausgehen, kommen für den ^{8}B-Kern zu einem übereinstimmenden Ergebnis: Um die experimentellen Impulsverteilungen zu reproduzieren, muß eine räumlich ausgedehnte Wellenfunktion für das schwach gebundene Proton im ^{8}B angenommen werden.

Für den Kern ^{19}C, der als schwerster Ein-Neutronen-Halo großes Interesse hervorgerufen hat, waren die experimentellen Ergebnisse bislang zu dürftig um endgültige Aussagen über dessen Kernstruktur zu treffen. Die hier vorgestellte Messung der longitudinalen Impulsverteilung nach dem ^{19}C-Aufbruch bei relativistischen Energien wurde kontrovers diskutiert, da sie mit den Ergebnissen, die bei einer ähnlichen Untersuchung mit sehr viel niedrigeren Strahlenergien gefunden wurden, nicht übereinstimmt [14, 10]. Die Diskrepanz könnte verschiedene Ursachen haben. Zum einem sind der abgedeckte Impulsbereich und die Statistik der hier vorgestellten Messung viel größer als in Ref. 14, zum anderen wird aber auch die Möglichkeit einer Energieabhängigkeit der Impulsbreite diskutiert [74].

Für die Breite der longitudinalen Impulsverteilung von ^{18}C-Fragmenten nach dem Aufbruch von ^{19}C in einem Kohlenstoff-Target wurde ein Wert von 69 ± 3 MeV/c (FWHM) ermittelt, wobei die Verteilung einer Lorentz-Kurve entspricht. Die gemessene Impulsverteilung wird durch verschiedene Theorien gut beschrieben. Die theoretischen Rechnungen zeigen, daß Effekte wie die dynamische Core-Polarisierung des ^{18}C-Cores durch das zusätzliche Neutron in diesem Kern bereits eine wichtige Rolle spielen.

Die im Rahmen dieser Arbeit untersuchten Kerne, ^{8}B und ^{19}C, stellen im Moment zwei wesentliche Grenzpunkte auf dem Gebiet der Halo-Kerne dar: ^{8}B ist derzeit der einzige experimentell nachgewiesene Fall eines Grundzustands-Protonen-Halos, und ^{19}C ist der bis jetzt schwerste Neutronen-Halo, der experimentell untersucht wurde. Die experimentellen und theoretischen Ergebnisse, die mit dieser Arbeit präsentiert werden, zeigen, daß sich in den beiden genannten Kernen ein Übergangsbereich von einer einfachen, separablen Struktur zwischen Core-Nukleus und Halo-Nuleon zu komplexeren Formen andeutet.

Contents

List of Figures

List of Tables

"Haloes, it seems, are not just for saints and angels but for some species of atomic nuclei as well."

W. Gelletly [30]

Chapter 1

Introduction

1.1 Halo nuclei

Halo nuclei are still quite a young phenomenon of nuclear structure. Among the large number of particle-bound but unstable nuclei, halo nuclei stand out with their unusually large spatial expansion.

The classical, or trivial case of a nuclear halo, although it was not called a halo at the time when it was first investigated in nuclear breakup reactions, is the loosely bound deuteron, a system of one proton and one neutron bound by only 2.225 MeV. To give a comparison, the protons and neutrons of an α particle (two protons and two neutrons), are bound roughly ten times stronger. The weak binding of the deuteron leads to a rather large proton–neutron distance of about 4 fm, compared to the range of the nuclear force of 1.2–1.4 fm.

The peculiar properties of many-body systems with weak binding are not limited to nuclei consisting of protons and neutrons, and they may include exotic particles, as the *hypertriton* does, which has a Λ halo [35].

Weakly bound systems of larger scale are, for instance, *Rydberg atoms*, atoms with an electron in a highly excited state. These systems, however, are bound by the long-ranging Coulomb force, and therefore are not directly comparable to the nuclear halo systems. On the other hand, in *deeply bound pionic states* in heavy nuclei, which have been discovered recently [84], the pion is bound by the interplay between the Coulomb force and the nuclear force of the core nucleus, which causes a halo-like state.

Other halo analogues can be found in systems with potentials that decrease faster than the Coulomb potential, as is the case for an electron bound in the weak dipole field of a neutral molecule [49] or for noble gas molecules that are bound by the short ranging van der Waals force. An overview of nuclear halos and their atomic and molecular counterparts can be found in review articles by P. G. Hansen [33] and K. Riisager [66].

Before we take a closer look at special cases of nuclear halos, it is necessary to point out what actually is called a halo state and what the preconditions for its formation are.

1.1.1 What is a nuclear halo state?

The nucleons of a nucleus are bound together by the nuclear force, which has only a range of a few femtometer. Therefore a nucleus should be rather compact – or unbound. The dependence of the charge radii on the nucleon number deduced from electron scattering data supports the idea that the nucleus is made of some sort of *incompressible fluid* with the volume proportional to the number of nucleons. This led to the well-known relation for the charge radius $R = r_0 A^{1/3}$ with $r_0 = 1.21$ fm, that also gives a good estimate on the nuclear matter radius for spherical nuclei, because protons and neutrons should be equally distributed in the nuclear core.

Not all nuclei, however, fit into this picture. If the nucleons fill the nuclear potential-well up to the limit, as is the case for nuclei close to the drip lines, threshold effects can appear. For a bound state close to the continuum, the nuclear binding energy can be so small that it allows the nucleon to tunnel into the surrounding space, leading to a probability to find a nucleon outside the nuclear core. Such a state is generally called a nuclear state with a large spatial expansion, or, for the more prominent cases, a *halo state*. In this case, the nuclear radius will be significantly increased and the density distributions for protons and neutrons will differ considerably.

The term "halo" refers to the weakly bound nucleon or nucleons forming a cloud of low density around a core of normal density. This term was borrowed from the luminous rings surrounding the moon or the sun, which one can see under certain conditions, because it pictures quite well the situation of the peculiar nuclear state. It appeared first in a paper by P. G. Hansen and B. Jonson in 1987 [36]. Since then it has become the label for a few light exotic nuclei with weakly bound nucleons in spatially extended states where the radius of the halo system is significantly larger than the normal nuclear radius.

Because nuclear halos are of genuine quantum mechanical origin, they can only be understood by considering the probability distributions of the least bound nucleons either in coordinate or momentum space. The most important, but not the only precondition for a nucleus to form a halo state is a small nuclear binding energy. A small orbital angular momentum of the state is also necessary, as an additional centrifugal barrier lowers the probability of tunneling to larger radii. Therefore, halo states are expected to appear most likely in s- and p-states. In the same way, a Coulomb barrier would hinder the formation of a halo state. For this reason, proton halos should be less pronounced than neutron halos.

Although the term "halo state" has been around for some time now, there is no precise definition of exactly when a nuclear state should be called a halo state. The main points are that the matter radius should be significantly larger than the standard nuclear radius, and that the halo system divides into clusters that have a larger distance from each other than in usual nuclei. This formation of clusters makes it possible to describe the

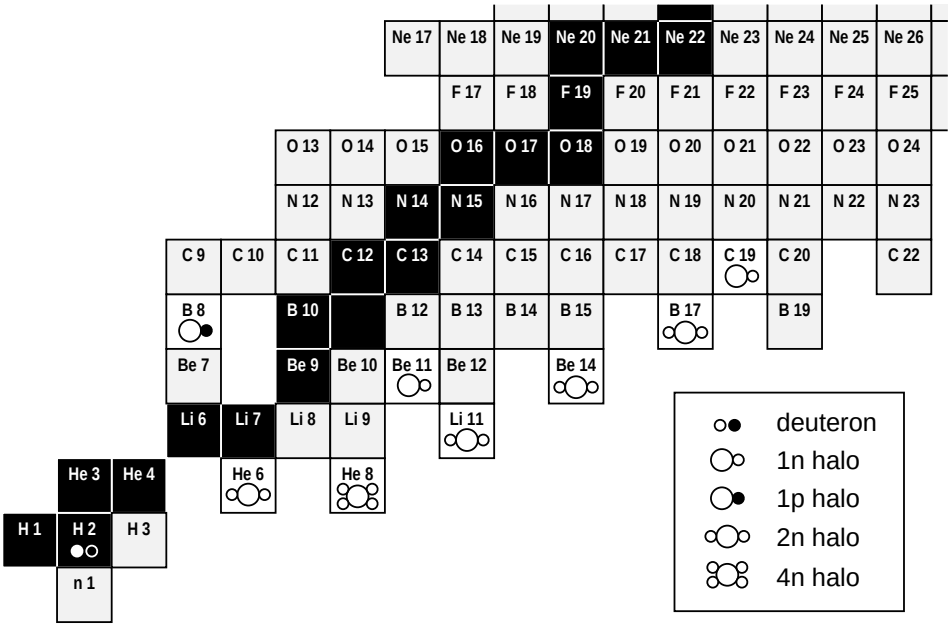

Figure 1.1: Chart of nuclei up to element 10. The ground state halo nuclei that have beed observed so far are indicated according to the symbols defined in the box.

halo nucleus as a two- or few-body system.

Halo nuclei that have been observed so far include a variety of configurations. The most basic one is the one-neutron halo. This is a two-body system consisting of the core and one neutron. But a halo can also consist of more than one nucleon, as is the case for a two-neutron halo. This three-body system benefits from the pairing of the two neutrons, while each subsystem, core plus one neutron or the di-neutron, is unbound. Even a four-neutron halo has been observed, but this also could be called a neutron *skin*, as the neutrons form an outer layer around the α-core. A skin merely indicates a difference of proton and neutron radius, like for an excess of neutrons with a normal density at the nuclear surface [78]. Although one-proton halos are not very probable, there is evidence for their existence. The halo nuclei observed so far are marked in Fig. 1.1.

Besides the different configurations of valence nucleons and core there are other characteristics to be distinguished. Halo structures can also develop in excited states, where the separation energy becomes small enough, e.g. in ^{17}F [54]. Furthermore, it is possible that the core of a halo system is in an excited state, or that there is an interaction between the halo nucleons and core degrees of freedom, like the dynamical core polarization of the ^{18}C core in ^{19}C [10]. These effects become important in heavier halo nuclei where the core nucleus is already far from stability.

The variety of characteristics makes clear that there is no simple definition for a halo nucleus. The experiments presented here and also theoretical calculations indeed indicate a transitional behaviour characterized by ad-

mixtures of of nuclear many-body effects, as for example in the case of core polarization, into the few-body dynamics of a pure halo configuration.

1.1.2 The Motivation to investigate halo nuclei

One of the main topics in experimental nuclear physics since the 1930s is to explore the chart of nuclei towards the driplines to find out where the limits of nuclear binding are. With the modern technologies of heavy-ion accelerators and radioactive beam facilities the aim is to gain detailed information on these exotic nuclei far from the valley of stability. This information is a crucial test of the available nuclear structure theories, and the discovery of the novel structures of halo nuclei is one of the best examples for this.

But there are also other reasons besides searching the limits of particle stability and looking for special cases of nuclear structure. The question how nuclear matter behaves at very high densities, something that is investigated for example in heavy-ion collisions at high energies, prompts also the question how it behaves at low densities. The halo surrounding a core is the only example of dilute nuclear matter available to experiments at this time.

The nucleus ^{8}B, so far the only ground state proton halo, takes part in the PPIII chain during the process of hydrogen burning in the sun with the reaction ^{7}Be(p,γ)^{8}B. The halo structure of this nucleus has an important influence on the proton capture cross section. Due to the large spatial expansion of the proton wave function in ^{7}Be, the capture can take place already at quite large distances, yielding an enhanced cross section for this reaction. In the following β^{+} decay of ^{8}B, a high-energy neutrino is emitted, which is important for testing the standard solar model that describes how the sun works, because this neutrino is most efficiently detected.

Unstable nuclei, and among them some halo nuclei, play a key role in the nucleosynthesis, the process that is held responsible for the existence of us and the universe around us. An example is the nucleus ^{17}F, that has a proton halo in its first excited state. The reaction ^{16}O(p,γ)^{17}F links different parts of the CNO-cycle and gives a link to heavier elements through further (p,γ)-reactions.

Astrophysics relies on nuclear structure data and nuclear theory to explain processes in stars, where nuclear matter exists under conditions which are very different from those found in stable nuclei.

If one compares a nuclear chart that lists all isotopes that had been observed and investigated thirty years ago with the chart of nuclei of today, it is evident that much progress has been made. In these unstable nuclei, novel structures like halo states were observed for the first time. However, the neutron drip line has only been reached experimentally for the lightest elements, and many isotopes at the proton drip line still need to be investigated.

The investigations that are presented in this work focus on the one-

nucleon halos ^{8}B and ^{19}C, both of which set new limits to the field of halo nuclei: ^{8}B as the only ground state proton halo observed so far and ^{19}C as the heaviest halo nucleus up to now. Both nuclei also indicate a transition between the halo structure and normal nuclear structure since simple cluster models can not properly describe the experimental findings of this work.

1.2 The history of halo nuclei

Given here is a brief list of some key-events in the history of halo nuclei, following a presentation by Björn Jonson at the "Joint Study Weekend on Drip-Line Nuclei" in Lisbon, 1998.

1936
- Discovery of ^{6}He [16]

1951
- The first on-line mass separation [43]

1966
- ^{11}Li was shown to be bound [62]

1969
- First spectroscopic study of ^{11}Li [41]

1979
- First fragmentation experiments at Berkeley [75, 82]

1983
- Measurement of a very large $E1$ transition in ^{11}Be [51]

1985
- Measurements of the total reaction cross-section for ^{11}Li disclose a remarkably large matter radius [77, 76]

1988
- Narrow transverse momentum width of ^{9}Li after dissociation reactions of ^{11}Li [42]

1990
- Narrow transverse momentum width of neutrons after dissociation reactions of ^{11}Li [4]
- Beta-delayed deuteron emission from ^{6}He [67]

1992
- Quadrupole moment of ^{11}Li [7]
- Charge changing cross-sections of ^{8,9,11}Li [17]
- Interplay between structure and reaction mechanisms in the dissociation of ^{11}Be [3]
- Proton halo of ^{8}B disclosed by its large quadrupole moment [52]

1993
- Beta-decay to the proton halo state in ^{17}F [19]
- Neutron decay of the unbound nucleus ^{10}Li [45]

1994
- Investigation of the unbound nucleus ^{10}He
- Density distributions of ^{6,8}He from proton elastic scattering in inverse kinematics

1995
- The proton halo in ^{8}B is observed by a narrow longitudinal momentum distribution [70]
- One-neutron halo of ^{19}C [14]
- Structure of ^{10}Li from stripping reactions of ^{11}Li and ^{11}Be [86]

1996
- Coulomb excitation of ^{11}Be [56]
- Investigation of the unbound nucleus ^{11}N [9]
- Spectroscopy of ^{11}Li with ^{11}Li + p reactions [44]

1997
- Invariant-mass spectroscopy of ^{10}Li and ^{11}Li [85]
- Spin alignment of unbound ^{5}He fragments [21]
- α–n correlations in fragmentation of ^{6}He [2]

1998
- The ^{19}C case [13, 10, and this work]

Chapter 2

The momentum of a halo nucleon

The questions of how matter and motion is distributed inside the nucleus have been experimentally investigated for a long time. Both questions are rooted in the quest for the nucleons' wave functions inside a nucleus. The measurement of the momentum of the remaining fragment after a one-nucleon removal reaction yields the momentum of the removed nucleon and was already used to study momentum distributions in stable nuclei [37]. For the investigation of halo nuclei this type of measurement provides a method to gain information on the wave function of the halo nucleon.

2.1 Nuclear structure information from experiments with secondary nuclear beams

There are different quantities that can be measured in order to investigate the halo structure of nuclei. From the measurement of total interaction cross sections, the nuclear radius can be deduced and a halo structure should be detectable. This type of measurement led to the discovery of the remarkably large radius of ^{11}Li by I. Tanihata *et al.* [77], which started the large interest in halo nuclei that continues today.

The measurements of magnetic dipole and electric quadrupole moments give information on nuclear deformations and on the proton distribution in the nucleus [6]. With this information, a large interaction cross section can be linked to either a deformation or a long tail in the matter distribution.

Measurements of the charge-changing and one-neutron removal cross sections also can resolve the difference between a deformation and a halo state [17]. In the case of a neutron halo, only the neutron-removal cross section is increased, whereas the charge-changing cross section of the halo nucleus and the corresponding core should be comparable.

For a proton halo, a measurement of the total interaction and one-proton removal cross sections of the halo nucleus and the corresponding core should contain a clear signature. The one-proton removal cross section

should be significantly increased, compared to the core nucleus, and this increase should roughly equal the difference of the total interaction cross sections of these two nuclei [78, 18].

Another approach is the measurement of the momentum distribution of the core fragments after a breakup of the halo nucleus, which gives information about the halo wave function in the system before the breakup.

2.2 Measurement of the halo wave function

The intrinsic momentum distribution of a nucleon inside a nucleus is directly connected to its wave function. The momentum distribution can be obtained by a Fourier transform of the squared wave function. A large spatial distribution results in a narrow distribution in momentum coordinates, as described by Heisenberg's uncertainty principle.

Therefore, the measurement of the halo nucleon's momentum distribution is a unique tool to directly obtain nuclear structure information. Experimentally, however, it is simpler to measure the momentum distribution of the core fragment. The advantages are a higher detection efficiency and a better definition of the reaction channels. This method was already used to study the momentum distribution on the surface of stable nuclei, as described in, e.g., Ref. 37.

The first experiment in which a surprisingly narrow distribution was observed studied the transverse momentum distribution of ^{9}Li fragments from the breakup of ^{11}Li [42], which gave further evidence for the neutron halo in ^{11}Li.

For a one-nucleon halo the link between the momentum of the halo nucleon and the core momentum is, as illustrated in Fig. 2.1, rather simple: regarding the core and the halo nucleon in the rest frame of the halo system, the momenta $\mathbf{p}_{\mathrm{halo}}$ and $\mathbf{p}_{\mathrm{core}}$ add up to zero and consequently

$$\mathbf{p}_{\mathrm{halo}} = -\mathbf{p}_{\mathrm{core}} \,. \tag{2.1}$$

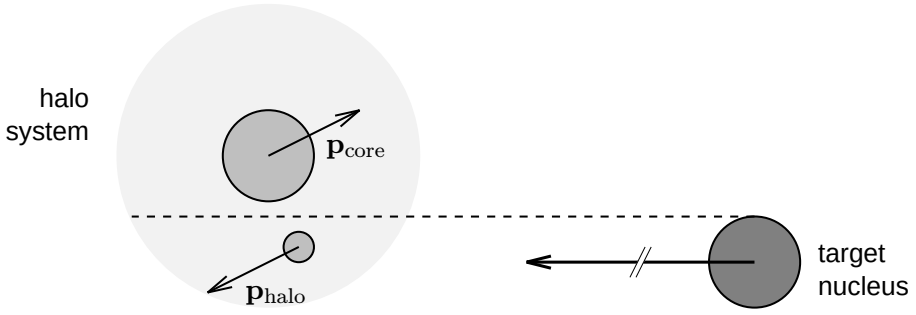

Figure 2.1: This drawing gives a schematic view of the breakup of a halo system in the reference frame of the halo system (projectile co-moving frame). In an idealized nuclear reaction the halo nucleon is removed by the target nucleus leaving the core nucleus undisturbed.

After removing the halo nucleon in a nuclear reaction, the momentum of the core can be measured.

Measuring the momentum distribution of the core, we obtain the momentum distribution of the halo nucleon and from this we can deduce the wave function – but there are limitations to this conclusion!

The identification of the measured momentum distribution as the ground state momentum distribution of the removed halo nucleon is only valid if the removal reaction was nuclear stripping and if the target nucleus basically is transparent to the core-fragment. This assumption is called the *transparent limit of the Serber model* and was applied to the theoretical description of the neutron production by deuteron stripping reactions [71].

Since there are other breakup mechanisms and since the approximation of a transparent target nucleus is not always valid, refinements to the Serber model are necessary in most cases.

2.2.1 The breakup mechanism

There are different reasons for the disturbance of the direct link between the core momentum in the center-of-mass frame of the halo system after the breakup and the momentum of the halo nucleon:

- the interactions between the three particles involved, which are target nucleus, projectile core, and halo nucleon;
- possible excitations of the target and/or the projectile core;
- the fact that the projectile core has to survive in order to measure its momentum and, as a consequence of this, the *shadowing* of the halo wave function.

First, one needs to understand how the halo nucleon is removed in the breakup reaction. In a simplified picture, this reaction can be divided into two different cases. In the case of small impact parameters, the halo nucleon can be removed in a *stripping reaction*, where the target either absorbs or scatters away the halo nucleon [71]. In the other case, inelastic scattering of the projectile or Coulomb interaction with the target can lead to an excitation into an unbound state and the subsequent breakup of the halo nucleus. This is called *diffraction dissociation* or *Coulomb dissociation*. The Coulomb dissociation is caused by high energy photons that are created in the quickly changing electric field of the target nucleus which is seen by the projectile. Coulomb dissociation is especially important for targets with a large number of protons, as the reaction probability is proportional to the square of the target charge [15].

Each of these mechanisms will have a different impact on the core momentum that can be measured after the breakup. In addition, one has to take final state interactions, i.e. interactions between the particles after the breakup reaction, into account, as for instance the Coulomb deflection of the core fragment by the target nucleus.

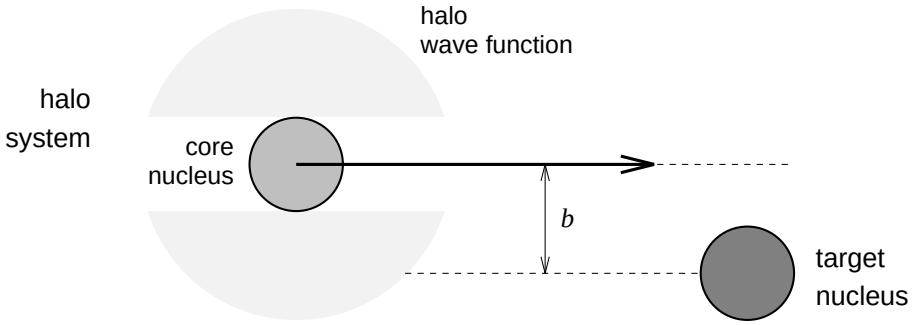

Figure 2.2: This schematic picture shows the area of the wave function that is mapped by a halo-nucleon removal (shaded area) in a simplified way. For impact parameters b smaller than the sum of core and target radius, the core nucleus can not be detected in the exit channel. In experiments that rely on the detection of the core fragment, no information of the halo wave function can be obtained for these reactions.

The second point of the above list depends on the system that is investigated. If the projectile core has no excited states that are bound, its excitation is irrelevant as the core fragment will not be detected. In general, energy that is used to excite either the projectile core or the target nucleus will be missing in the exit channels.

The last point of the list addresses the problem that the halo nucleon can be removed only from the surface of the projectile since the core has to stay intact in order to measure its momentum. In a simple picture, one could argue that all reactions with an impact parameter smaller than the sum of core and target radius will most probably destroy the core (core breakup), therefore the cylindrical area of the wave function that overlaps with the core is not sampled. This simple picture, also called the *black-disk model* [25], can be used if projectile energies are high and scattering terms are negligible. Figure 2.2 illustrates the black disk model.

2.2.2 Consequences for the measurement

The perturbing effects of the breakup mechanism on the core fragment's momentum can be partly avoided or minimized by choosing optimum conditions for the measurement.

In experiments it has been shown that the transverse components of the core momentum are more affected by the breakup mechanism through diffraction dissociation and final state Coulomb deflection. These effects cause a broadening of the tranverse momentum distribution of the core fragments.

The longitudinal momentum distribution, which is measured in the experiments described in this work, is less disturbed by the breakup reaction and therefore a better tool for the investigation of the halo [34]. Furthermore, at energies in the range of 1.0–1.5 GeV/u, projectile velocities are much larger than the intrinsic velocities in the halo system and the sudden

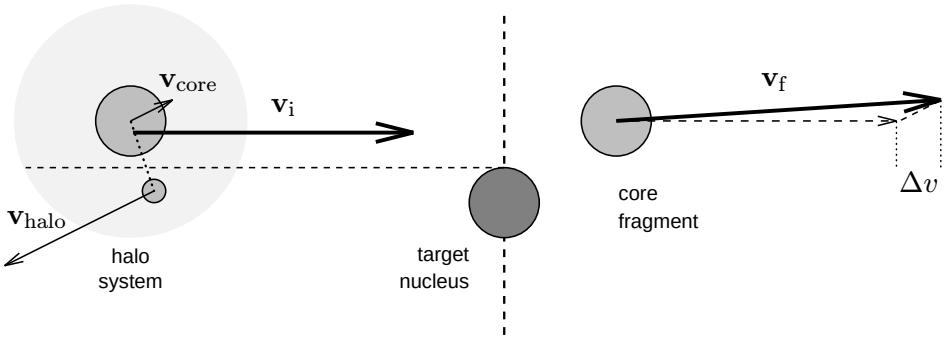

Figure 2.3: The kinematics of the halo breakup. Shown here, in contrast to Fig. 2.1, are the velocity vectors before and after a breakup reaction by nuclear stripping. Measuring the velocity change parallel to the projectile axis, Δv, the longitudinal core momentum can be deduced.

approximation can be used.

For light targets, nuclear stripping plays a dominant role in the one nucleon removal, while targets with a large number of protons mainly contribute to the Coulomb dissociation cross section. The measurement of breakup reactions in different target materials can give further insight into this question and is therefore an interesting topic of investigation.

2.2.3 The kinematics

The momentum of the halo core becomes available, as was described in the beginning of Sec. 2.2, in a breakup reaction at high beam energies. The next question that has to be answered is how to measure this momentum. The momentum vector $\mathbf{p}_{\mathrm{core}}$ can be split into two components, one parallel to the path of the incident projectile and one perpendicular to it. There should be no difference in the longitudinal and transverse momentum distributions, however the transverse momentum is more likely to be affected by the breakup reaction and by Coulomb deflection than the longitudinal component, as discussed above. The longitudinal momentum can be obtained from the difference of the velocities of the incident projectile and the outgoing core fragment, projected onto the projectile axis. The difference in velocities is not affected by the mass-loss in the breakup reaction. In a momentum measurement, the different masses of the projectile and the breakup fragment have to be taken into account.

Because exotic projectiles at high energy are only available as a secondary beam, one faces the problem that the momentum spread of the projectiles is orders of magnitude larger than the intrinsic momentum that needs to be measured. The solution for this problem, the use of a magnetic spectrometer in energy-loss mode, will be described in the next chapter.

Chapter 3

The magnetic spectrometer FRS

In this chapter I will discuss the ion-optical aspects of the measurements of longitudinal momentum distributions. A detailed derivation of the equations needed for the transformation of the measured positions into the longitudinal momentum is given in Appendix A. Here, I will focus on the application of the energy loss mode for the measurement of longitudinal momentum distributions.

But first, I need to describe the tool that was used, the *projectile fragment separator* (FRS).

3.1 The fragment separator

The fragment separator FRS is a high-resolution forward spectrometer designed for research studies with relativistic heavy ions [28]. As part of the high-energy, heavy-ion research facility at GSI, it started operation in 1990. Providing the possibility of the production of secondary radioactive beams via projectile fragmentation and their efficient separation, it is now the key-instrument for the radioactive beam program at GSI.

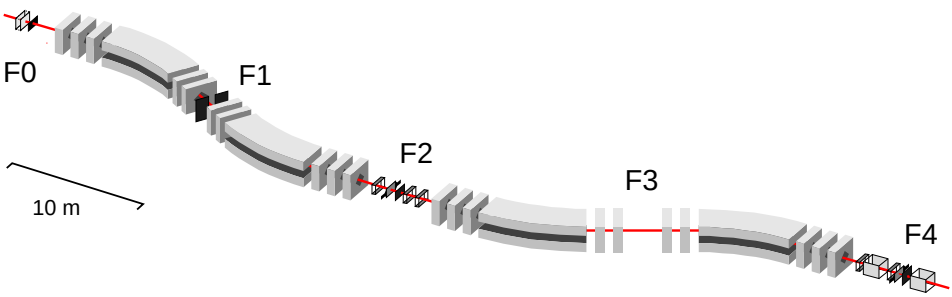

Figure 3.1: This plot schematically shows the dipole and quadrupole magnets of the FRS. F0 denotes the entrance of the spectrometer, F1 through F4 mark the four focal planes.

The FRS comprises four independent stages. Each stage consists of a 30° dipole magnet and sets of quadrupole magnets in front of and behind the dipoles. The quadrupoles provide first-order focussing and the proper illumination of the dipoles' field volume. To correct second order aberrations, sextupole magnets are placed directly in front of and behind each dipole. There are four focal planes, as indicated in Fig. 3.1. In the achromatic mode of the FRS, we have point-to-point imaging in x-direction, i.e. in the direction of the dispersion, at each focal plane.

The momentum resolving power $p/\Delta p$ of the FRS is 1500 at an emittance of $20\,\pi$ mm mrad and a transmission of $\pm 1\%$ in $\Delta p/p$. Heavy-ion beams with magnetic rigidities ranging from 3 Tm to 18 Tm can be analyzed.

3.2 The energy-loss mode

The energy loss mode is a special ion optical setting of a two-stage spectrometer where the combination of both stages is an achromatic system, while each stage by itself is dispersive. This is also called *dispersion matched mode* because the dispersion of the first stage is compensated by the dispersion of the second stage. The energy loss in a target that is inserted before the second stage, however, can be measured with the dispersion of the second stage. In this way the energy loss measurement is independent

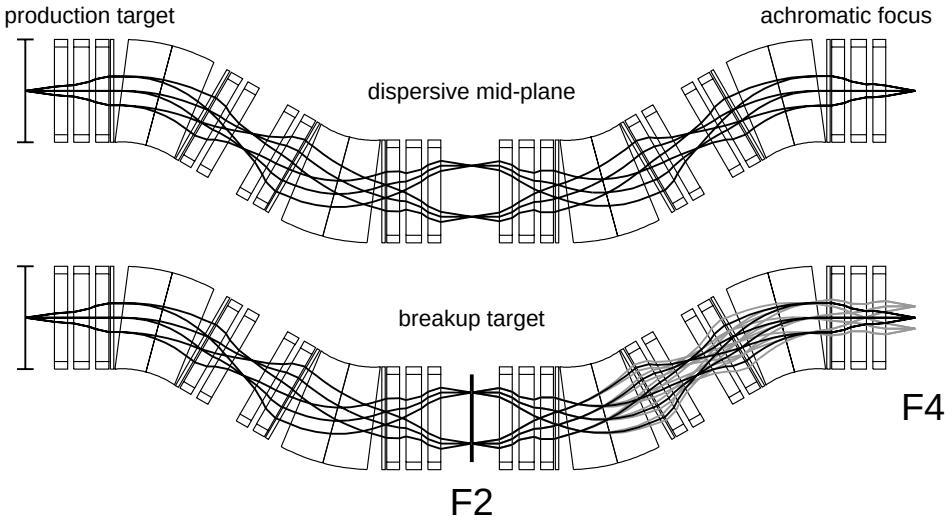

Figure 3.2: These ion optical plots of the FRS display the function of the energy loss mode. The upper plot shows the achromatic system with a dispersive mid-plane F2. Beams of three angles and two energies enter the spectrometer from the left. The two energies are separated at the mid-plane and focussed back at the final focal plane F4. In the lower plot, a reaction target is inserted at the dispersive mid-plane F2. The additional energy spread due to the reactions in the target is indicated by the grey beams, which are dispersed at F4.

of the energy spread of the incoming beam.

The energy loss spectrometer was first proposed by C. Schaerf and R. Scrimaglio in 1964 as a new magnetic analyzer for scattering experiments [68]. With the use of secondary beams produced in nuclear fragmentation, the energy loss spectrometer became an ideal tool for measurements with exotic beams.

With a secondary beam of exotic nuclei that have small production cross sections, it is desirable to make use of the full acceptance of the spectrometer. For the FRS this means a momentum spread of 2%. The effect that we want to study, the additional momentum induced by the breakup reaction, is at relativistic energies two orders of magnitude smaller and therefore requires the use of the energy-loss mode. Using the energy-loss mode, the momentum change in the breakup reaction can be measured independently of the initial momentum spread of the secondary beam.

3.3 Determination of the longitudinal momentum

The energy-loss mode enables us to translate the momentum change in the breakup target into a position distribution that can be measured by position sensitive detectors. The momentum change, however, has three origins. The first is the change of the particle mass in the one-nucleon removal reaction, and the second is the addition of the intrinsic momentum of the removed nucleon. One also has to take into account that there is an atomic energy loss in the breakup target. If the acceptance of the second spectrometer stage would be large enough, one could detect the particles that undergo a breakup reaction and those which do not suffer a nucleon removal in one measurement. But the change in magnetic rigidity for, e.g., a one-neutron removal from ^{19}C is with more than 5% already far outside the acceptance of the FRS. Therefore the change of the particle mass and the atomic energy loss in the breakup target is taken into account by adjusting the magnetic rigidity of the second spectrometer stage to the emerging core fragment.

In the following, I will describe how the longitudinal momentum after the breakup reaction can be calculated for a single particle that moves through the spectrometer. The following description refers to an idealized case of breakup reaction, since the target is assumed to be infinitely thin. The atomic slowing down and angular straggling of the projectile before the breakup and of the core fragment after the breakup reaction, which can not be avoided in a realistic measurement, is not considered at first. A second method, that was actually used for the momentum analysis, takes the energy loss in the breakup target into account. The question of the absolute value of the momentum will be discussed in Sec. 4.6.2.

The longitudinal momentum of the core fragment after the breakup reaction, p_{F2}, can be calculated from the velocity of the incident projectile,

Table 3.1: This table lists ion optics variables and gives their definitions

x_{F2}	particle x-position at the mid-plane	x_{F4}	particle x-position at the final focus
v_{F0}	particle velocity in front of the breakup target	v_{F2}	particle velocity behind the breakup target
γ_{F0}	Lorentz factor of particle in front of the breakup target	γ_{F2}	Lorentz factor of particle behind the breakup target
p_{F0}	total longitudinal momentum in front of the breakup target	p_{F2}	total longitudinal momentum behind the breakup target
p_{A}	momentum of the reference particle in the first spectrometer stage A	p_{B}	momentum of the reference particle in the second spectrometer stage B
q_{A}	particle charge in front of the breakup target	q_{B}	particle charge behind the breakup target
m_{A}	particle rest mass before the breakup target	m_{B}	particle rest mass behind the breakup target
χ_{A}	reference magnetic rigidity of the first spectrometer stage A	χ_{B}	reference magnetic rigidity of the second spectrometer stage B
D_{A}	dispersion of the first spectrometer stage A	D_{B}	dispersion of the second spectrometer stage B

v_{F0}, and the velocity change in the breakup reaction, Δv (see Fig. 2.3):

$$\begin{aligned} p_{F2} &= \gamma_{F2} m_{B} v_{F2} \\ &= \gamma_{F2} m_{B} (v_{F0} + \Delta v) \,, \end{aligned} \tag{3.1}$$

Here, $\gamma_{F2} m_{B}$ is the relativistic mass of the core fragment. The velocity change Δv is given in reference to the laboratory frame. In order to extract the information about the intrinsic momentum of the core fragment before the breakup reaction, this velocity change needs to be transformed into the momentum of the core fragment in the halo-system's rest frame. To obtain this, we can later transform the total momentum p_{F2} into the projectile co-moving frame that moves with the velocity v_{F0}.

Employing the condition for the dispersion matched mode,

$$D_{B} = -(x|x)_{B} D_{A} \,, \tag{3.2}$$

the momentum p_{F2} can be expressed in a first order approximation using the momentum of the reference particle in the second spectrometer stage, $\gamma_{F2} m_{B}\, v_{B}$ (see Appendix A.4).

$$p_{F2} = \gamma_{F2} m_{B}\, v_{B} \left(1 + \frac{x_{F2}}{D_{A}} + \frac{x_{F4}}{D_{B}} \right) \,, \tag{3.3}$$

where D_{A} and D_{B} are the dispersion of the first and the second spectrometer stage. A complete list of the variables used here is given in Table 3.1. Please

note that in the case of the energy-loss mode the dispersion D_{A} is negative. With the definition of the magnetic rigidity, $\chi_{\mathsf{B}} = \gamma_{\mathsf{F2}} m_{\mathsf{B}}\, v_{\mathsf{F2}}/q_{\mathsf{B}}$, we obtain

$$p_{\mathrm{F2}} = q_{\mathsf{B}}\chi_{\mathsf{B}} \left(1 + \frac{x_{\mathrm{F2}}}{D_{\mathsf{A}}} + \frac{x_{\mathrm{F4}}}{D_{\mathsf{B}}}\right) . \tag{3.4}$$

To get the longitudinal momentum transformed into the rest frame of the halo system, $p_{\parallel}$, which moves with the velocity v_{F0}, we have to do a Lorentz transformation of the momentum p_{F2}.

Using the total energy in the laboratory frame of reference,

$$E_{\mathrm{F2}} = \sqrt{p_{\mathrm{F2}}^2 c^2 + m_{\mathsf{B}}^2 c^4}\,, \tag{3.5}$$

and with $\beta_{\mathrm{F0}} = v_{\mathrm{F0}}/c$ and $\gamma_{\mathrm{F0}} = (1 - \beta_{\mathrm{F0}}^2)^{-1/2}$, one can use the equation

$$p_{\parallel} = \gamma_{\mathrm{F0}} \left(p_{\mathrm{F2}} - \beta_{\mathrm{F0}} \frac{E_{\mathrm{F2}}}{c}\right) \tag{3.6}$$

to calculate the corresponding momentum $p_{\parallel}$ in the projectile co-moving reference frame.

In Appendix A it is pointed out that the momenta and velocities in the ion optical equations refer to the components in the direction of the beam axis. So the longitudinal momentum $p_{\parallel}$ calculated in Eq. 3.6 in principle needs to be corrected for the incident angle of the projectile. However, the angles of the incoming projectiles are very small and this correction would be much smaller than the other uncertainties in this measurement.

In practice, it is advantageous to use a slightly simplified method for calculating the momentum distribution, and there are good reasons to do so. To get the proper momentum distribution with the method described above, it is essential to do a Lorentz transformation according to the velocity v_{F0} of each single particle. The velocities and positions of the particles at the breakup target have to be known precisely in addition to the information collected at the final focal plane.

Since the energy-loss mode already yields a distribution that corresponds to the change in momentum caused by the breakup reaction, which is in fact what we want to measure, we do not need to calculate the actual total momentum of the breakup fragments.

This way the momentum determination does not depend on the position information at the breakup target, thereby minimizing uncertainties. And we can use a simpler Lorentz tranformation as will be seen later.

Using the dispersion of the second spectrometer stage, D_{B}, the measured position x_{F4} corresponds to a change in momentum

$$\Delta p_{\mathrm{F2}} = q_{\mathsf{B}}\chi_{\mathsf{B}} \left(\frac{x_{\mathrm{F4}}}{D_{\mathsf{B}}}\right) . \tag{3.7}$$

However, this is the momentum change in the laboratory reference frame. To do the Lorentz transformation into the co-moving system, one can add

the momentum p_{B} of the reference particle in the second spectrometer stage. In short, this method corresponds to the ideal case where the incoming projectiles have no momentum distribution, i.e. the position x_{F2} is zero for all projectiles. Due to the energy-loss mode, there is no difference in the position distributions at the final focus, since they do not depend on the momentum distribution of the projectile. Therefore the position information at F2 is not needed in this case.

The momentum

$$\begin{aligned} p_{\mathrm{F2}}^{\mathrm{ideal}} &= p_{\mathsf{B}} + \Delta p_{\mathrm{F2}} \\ &= q_{\mathsf{B}} \chi_{\mathsf{B}} \left(1 + \frac{x_{\mathrm{F4}}}{D_{\mathsf{B}}} \right) \end{aligned} \tag{3.8}$$

can then be transformed into the projectile co-moving frame. For an infinetely thin target one would transform to the projectile velocity v_{F0}, as mentioned before. In the experiment, a relatively thick breakup target is used. To account for the slowing down of the projectile (and also of the breakup fragment, see Sec. 4.6.2) in the breakup target, the velocity of non-reacting projectiles *behind* the breakup target, let us call it $\beta_{\mathrm{F2}}^{\mathrm{pro}} = v_{\mathrm{F2}}^{\mathrm{pro}}/c$ is usually used. This velocity is measured in a separate setting, where the non-reacting projectiles are transmitted to the final focal plane. The advantage of this method is that only position information at the final focal plane is required.

The Lorentz transformation to the system moving with $v_{\mathrm{F2}}^{\mathrm{pro}}$ looks like this:

$$p_{\parallel}^{\mathrm{ideal}} = \gamma_{\mathrm{F2}}^{\mathrm{pro}} \left(p_{\mathrm{F2}}^{\mathrm{ideal}} - \beta_{\mathrm{F2}}^{\mathrm{pro}} \frac{E_{\mathrm{F2}}^{\mathrm{ideal}}}{c} \right) , \tag{3.9}$$

with

$$E_{\mathrm{F2}}^{\mathrm{ideal}} = \sqrt{(p_{\mathrm{F2}}^{\mathrm{ideal}})^2 c^2 + m_{\mathsf{B}}^2 c^4} \, .$$

One should keep in mind, however, that the spread in velocities at the breakup target causes differences in the energy loss. How big this effect is, depends on the projectile energy. For the energies used in the measurements described here, this is a small effect (see Eq. 4.1).

Employing Eq. 3.6 or Eq. 3.9, the longitudinal momentum of each single breakup fragment can be calculated in the projectile co-moving frame. The prerequisite for this is the determination or measurement of the unknown variables, which will be described in the following chapter.

Chapter 4

Measuring the longitudinal momentum distribution

Having described the fragment separator and the energy loss mode in Chapter 3, I will focus on the process of measuring longitudinal momentum distributions at the FRS in this chapter.

4.1 The necessary information

From Eqs. 3.6 & 3.9, that were introduced in the previous chapter, we can see which variables have to be determined or measured in order to obtain the longitudinal momentum for each particle and finally a momentum distribution.

First of all we have to be sure *which* nuclei are measured, which means that we have to have a particle identification. Details about the way the particles were identified are given in Sec. 4.4. With the particle identification, $m_{\mathsf{A}}, q_{\mathsf{A}}, m_{\mathsf{B}}$, and q_{B} are fixed. The magnet setting of the spectrometer will give us the magnetic rigidities χ_{A} and χ_{B}. The dispersions D_{A} and D_{B} have to be known as well as the absolute x-positions of the particles at F2 and F4. Here, the variable x_{F4} and the dispersion of the second spectrometer stage, D_{B}, play a key role because they have the largest contribution in determining the longitudinal momentum distribution. If all the above mentioned variables are known, the longitudinal momentum change of the core fragment $p_{\parallel}$ in the breakup target can be calculated.

Because the measured momentum change Δp is, as pointed out in Appendix A.1, the projection of the momentum change onto the central beam axis of the spectrometer, it is not equal to the longitudinal momentum change for projectiles that enter the breakup target at an angle to the reference axis. These angles are very small due to the high forward velocities of the beam particles. But to check this, the angles of the incoming projectiles should be measured. It was found that the angular deviation from the central beam axis has no noticeable effect on the longitudinal momentum distribution and can therefore be neglected.

The measurement of angles has yet another application. The momentum range transmitted through the spectrometer is not constant over the complete interval of angles with which the breakup fragments emerge from the target. For the larger angles, the transmission is reduced to a smaller momentum range. If the angles are known, they can be limited to values that give a full transmission of momenta. A detailed description of this possibility will be given in Sec. 5.2.

4.2 The detectors

Before going into the details of the measurement, I will briefly describe the detectors that were employed and the kind of information they give.

4.2.1 Time projection chamber

For the determination of the particle positions in x- and y-direction, newly developed time projection chambers (TPC) [12] were employed. These detectors have a resolution better than 0.5 mm in x- and y-direction. They also have a very small amount of matter in the active area. This is important because these detectors are mounted at the dispersive mid-plane, and every layer of matter at this position worsens the achievable resolution of the spectrometer and acts as a breakup target.

Technical layout

The TPC is a gas filled detector. When an ionizing particle penetrates the detector, electrons that are created along the track drift in a vertical electric field into the proportional chambers that surround each anode wire.

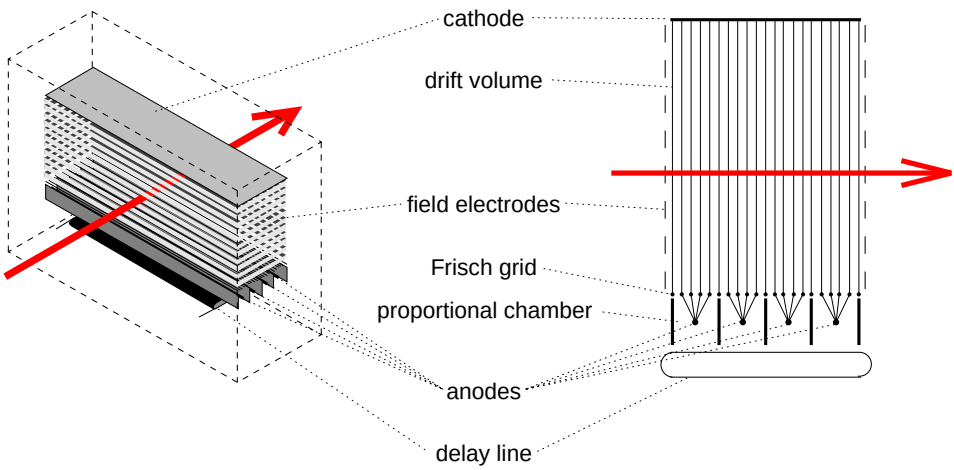

Figure 4.1: Schematic layout of the time projection chamber (TPC). A perspective view (left) and a cross-sectional side view (right) are shown.

Through the measurement of the electron drift time the vertical (y-) position of the particle beam can be deduced. The horizontal (x-) coordinate is recorded by a delay line placed below the anodes. The induced pulse is transmitted to the left and the right end of the delay line and the time difference of these two signals gives the x-position of the particle.

The schematic layout of this detector is depicted in Fig. 4.1. The dimensions are as follows: 240 mm delay line width, corresponding to 1500 ns delay time; 65 mm vertical drift length with a maximum vertical electron drift time of about 1150 ns; field electrodes are mylar strips of 25 μm with 0.5 μm aluminum coating on both sides, the strips are 3 mm wide and have a 5 mm pitch. Because the field electrodes are aligned horizontally, their matter is distributed homogeneously along the dispersive x-axis of the magnetic spectrometer. The delay line consists of a copper wire of 0.13 mm diameter wound with a pitch of 0.18 mm. The detector is operating in a 90% Ar + 10% CH_4 atmosphere (P10 gas) at room temperature and normal pressure.

Position determination

An additional reference timing signal is needed to measure the drift time and delay times that are used for the determination of the beam position. For this, plastic scintillators are used. Figure 4.2 illustrates the way the drift time and delay times are measured: A common start signal is created in the plastic scintillator (position A). The beam particle then moves on towards the TPC. In the TPC (position B), electrons are released through the ionisation of the detector gas. The electrons drift to the anode and create the stop signal in the anode (C). The induced signal in the delay line travels to the left (D) and the right (E) and gives the stop signals of the delay line. There are six times measured for each TPC: two delay line times, t_{dl} (left) and t_{dr} (right), and four anode times, t_{a1}, t_{a2}, t_{a3}, and t_{a4}.

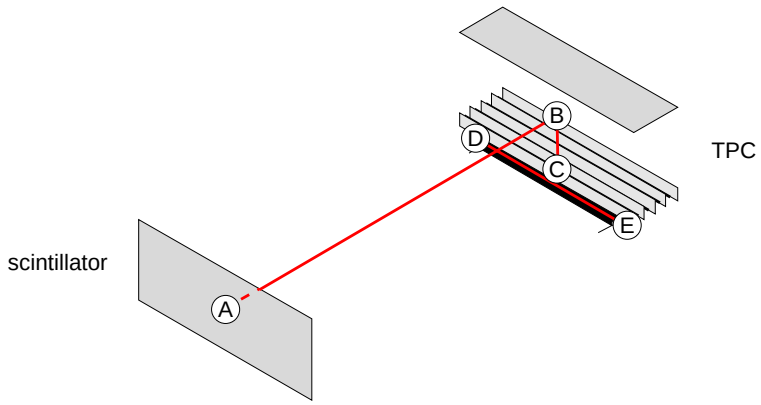

Figure 4.2: This figure illustrates the way of determining the x- and y-position of a charged particle beam passing through the TPC. A description is given in the text

The anode time directly yields the electron drift time plus an offset from the time it takes the particle to travel the distance A–B, which is constant for all particles if the beam angles are small. From the difference of t_{dl} and t_{dr}, the x-position can be deduced. The total delay line length is a constant that can be used to check the time signals. The *control sum*

$$t_{\mathrm{cs}i} = t_{\mathrm{dl}} + t_{\mathrm{dr}} - 2t_{\mathrm{a}i} = \mathrm{const.}$$

should equal the total delay line length and can be computed for each of the four anode times $t_{\mathrm{a}i}$ $(i = 1, 4)$ separately. Noise signals very unlikely fulfill this condition and can be discarded by its application.

4.2.2 Multiple sampling ionisation chamber

The *multiple sampling ionization chamber* (MUSIC) is designed for the charge determination of heavy ions [61] by measuring the energy deposition in the detector gas. The MUSIC is a parallel-plate ionization chamber filled with P10 gas (90% Ar, 10% CH_4) at normal pressure and room temperature. The active area of the detector has a cross section of 276 mm by 280 mm, the 4 signal anodes have a length of 100 mm each, corresponding to 17.11 mg/cm^2 P10 gas. A schematic view of the detector is given in Fig. 4.3. An ionizing particle that penetrates the detector gas generates a cloud of gas ions and free electrons. The number of released electrons in the gas is to first order proportional to the square of the charge of the penetrating particle. In the electric field, the electrons drift towards the segmented anode. Charge sensitive preamplifiers convert the charge of the collected electrons into a signal amplitude which is proportional to the number of collected electrons.

The specific energy loss $-dE/ds$ (s is in the path length the particle travels in the absorber) of charged particles in a material is, in first order Born approximation, described by the Bethe formula

$$-\frac{dE}{ds} = \frac{4\pi Z_{\mathrm{p}}^2}{m_e v^2}\left(\frac{e^2}{4\pi\varepsilon_0}\right)^2 Z_{\mathrm{t}} N_{\mathrm{t}} L \tag{4.1}$$

with the stopping number

$$L = \ln\frac{2m_e v^2}{I} - \ln(1-\beta^2) - \beta^2 \,.$$

Here, Z_{p} and v are the proton number and velocity of the particle, Z_{t} and N_{t} are the proton number and particle density of the penetrated material, m_e is the electron rest mass, and e is the electronic charge. The parameter I denotes the mean excitation energy of the material, in this case that of the detector gas. From this formula one derives that the energy loss (and therefore the number of released electrons) depends on the charge and on the velocity of the particle. For velocities with $0.03 < \beta < 0.95$, dE/ds

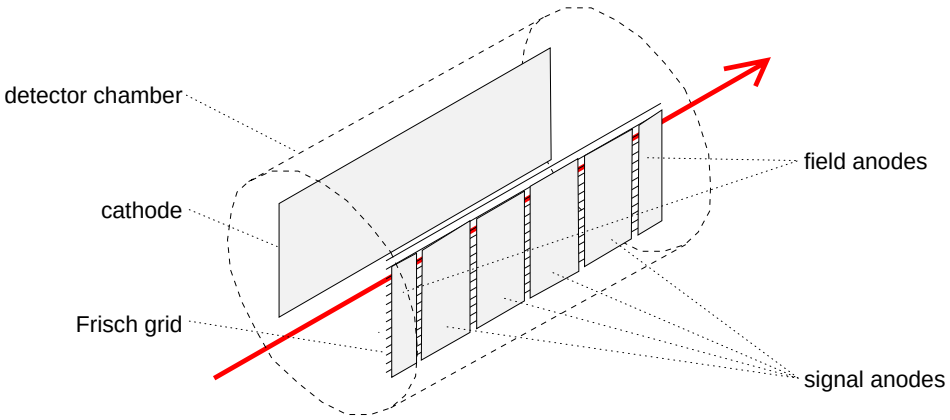

Figure 4.3: Schematic view of the multiple sampling ionization chamber MUSIC.

decreases with roughly $1/\beta^2$, but for relativistic particles with $\beta \gtrsim 0.95$, dE/ds increases again.

It should be noted that the MUSIC of course does not measure the energy loss, but the ionization in the detector gas, which is related to the *energy deposition*. The energy loss and the energy deposited inside the detector can differ from each other due to the fact that at very close encounters of the beam particle with the gas atom δ rays are created. These δ rays are energetic electrons that can create further ions – or leave the active volume of the detector. In the latter case, the deposited energy is smaller than the energy loss of the beam particle. This reduction of deposited energy depends on the geometry of the detector volume. A simple approximation to account for this effect was described by M. Pfützner *et al.* [61]. In addition to the maximum energy which can be imparted to an electron in a collision,

$$E_{\mathrm{M}} = \frac{2m_e c^2 \beta^2}{1-\beta^2}\,, \tag{4.2}$$

they employ the restricted energy loss E_{d}. The result is the *truncated Bethe-Bohr model*, which I present here in a slightly rewritten form:

$$\Delta = s\,\frac{4\pi Z_{\mathrm{p}}^2}{m_e c^2 \beta^2}\left(\frac{e^2}{4\pi\varepsilon_0}\right)^2 N_{\mathrm{t}} Z_{\mathrm{t}}\left[\frac{1}{2}\ln\frac{E_{\mathrm{M}} E_{\mathrm{d}}}{I^2} - \beta^2\right]\,, \tag{4.3}$$

where Δ is the mean energy deposition in the detector gas and s the active length (thickness) of the gas volume. For $E_{\mathrm{d}} = E_{\mathrm{M}}$, this equation is equivalent to Eq. 4.1. The parameter E_{d} is empirical and depends on the dimensions of the absorber. The measured velocity dependence of the energy loss of a ^{12}C beam at around 1.5 GeV/u is plotted in Fig. 4.8.

4.2.3 Plastic scintillator

Plastic scintillators are mainly used as timing detectors at the FRS. In scintillation detectors, a fraction of the kinetic energy that a charged par-

ticle loses in the scintillator is converted into fluorescent energy. Besides a fast rise time of the light pulse, the light-output is also proportional to the energy loss of the particle. This makes scintillation detectors also suited for the identification of the particle charge. Photomultiplier tubes convert the light pulse into an electric pulse. The scintillation detectors mounted at the FRS employ BC420 plastic scintillator of 5 mm thickness and are fitted with at least two photomultipliers, one on the left and one on the right side, to improve the time resolution and to give position information as well.

4.3 Experimental setup

The standard setup at the FRS had to be extended in order to measure all quantities necessary for the determination of the longitudinal momentum distribution, as listed in Sec. 4.1. Modifications at the central focal plane (F2) were necessary to achieve a complete tracking of the beam particles because the beam position at the focus as well as the angles of the incoming and outgoing particles were needed. At the final focus (F4), an additional reaction target was installed to investigate charge changing cross sections.

4.3.1 Setup at the dispersive mid-plane

Three time projection chambers were mounted at the dispersive mid-plane F2. The detectors and the breakup target at F2 were not mounted in vacuum. The beam line was fitted with vacuum windows at the entrance and exit of the F2 area. Not mounting the TPC detectors in vacuum is technically a much simpler solution, besides this, vacuum windows for each detector were avoided. The total of air, in mass per cross section, roughly equals four additional vacuum windows that would have been necessary for an installation of the TPCs in vacuum. The setup at F2 is schematically

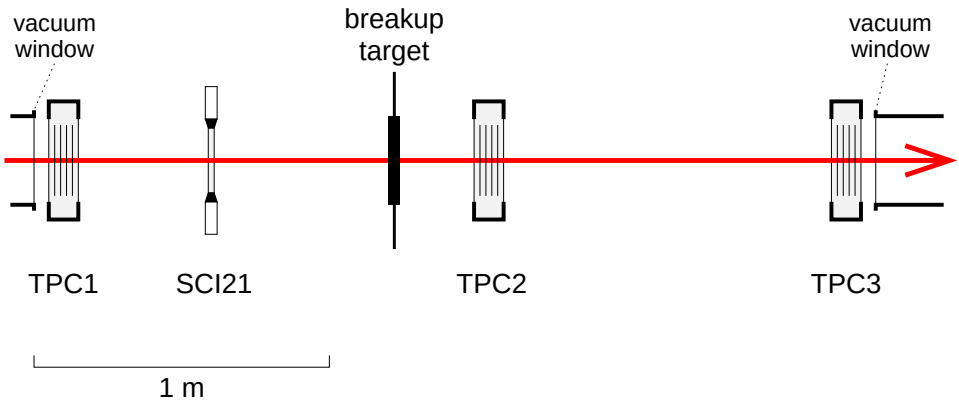

Figure 4.4: Schematic picture showing the detector setup at the dispersive mid-plane F2.

depicted in Fig. 4.4.

The secondary beam entered the F2-area through a 0.1 mm steel vacuum window (78.7 mg/cm^2). The first detector was TPC1 for the determination of the particle position before the breakup target. The timing detector SCI21 at F2, a 5 mm plastic scintillator (516 mg/cm^2), was mounted behind TPC1. This plastic scintillator also allowed a charge identification of the incoming beam particles. The breakup targets were mounted in a target ladder following the scintillator. Targets of carbon, lead, and polyethylene with thicknesses of 4–8 g/cm^2 were used in these experiments. Behind the breakup target, the combination of TPC2 and TPC3 measured the position and the angle of the emerging particles. Through tracking back from TPC2 and TPC3 onto the target plane and using TPC1, the angle of the incoming particles was determined. With a spatial resolution of 0.5 mm in the TPCs, the angular resolution is limited to approximately 0.5 mrad. The vacuum window at the exit of the F2-area was a 0.2 mm titanium foil (90.8 mg/cm^2).

4.3.2 The setup at the final focus

The detector setup at the final focus, see Fig. 4.5, was mounted behind a 0.2 mm titanium vacuum window. Two TPCs, TPC4 and TPC5, measure position and angle of the beam particles. With the information of the position and the angle, the x-distributions can be projected onto the image plane at F4, as in most cases the image plane does not fall onto a detector. An ionization chamber (MUSIC1) furnishes charge determination. The stop detector, SCI41, was placed behind TPC5 and provided the common time signal for the TPCs at F4. With the detectors SCI21 and SCI41, the time of flight of the particles in the second spectrometer stage was measured. The time of flight is used for the full particle identification and for the velocity correction of the MUSIC signals.

Additional to the setup necessary for the measurement of the momentum distribution, a reaction target ladder and a second ionization chamber

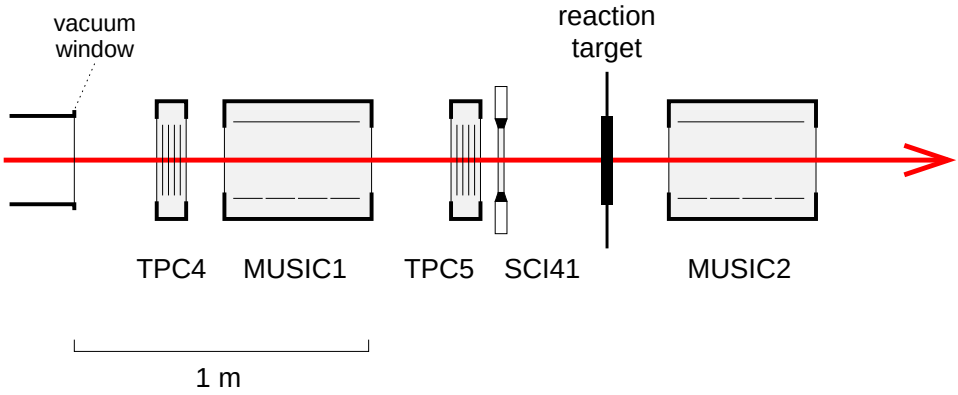

Figure 4.5: Detector setup at the final focal plane F4.

(MUSIC2) were placed at the end of the detector setup. With the MUSIC1 and MUSIC2, we could measure the nuclear charge changing cross sections for the inserted reaction target.

4.4 Particle identification

The identification of the particles plays an important role in determining the momentum distribution. Each stage of the magnetic spectrometer, taken separately, can only provide a selection of the magnetic rigidity, so a variety of different nuclei arrives at the breakup target and at the final focus. These nuclei have to be identified to obtain clean conditions for the momentum distributions.

4.4.1 Partial identification at F2

The energy signal of the plastic scintillator SCI21 in front of the breakup target was used to put a condition gate on the proton number of the incoming projectile. The measurement of the energy deposition in the scintillator depends on the position at which the particle penetrates the scintillator (see Fig. 4.6). A correction of this dependence with the position measured by the scintillator considerably improved the energy resolution. A measured spectrum of the energy loss in the scintillator SC21 can be found in Fig. 5.2.

4.4.2 Complete identification at F4

At the final focus, a determination of proton number and neutron number of the fragments was necessary. The resolution had to be sufficient for a clean in-flight identification. A look at the definition of the magnetic

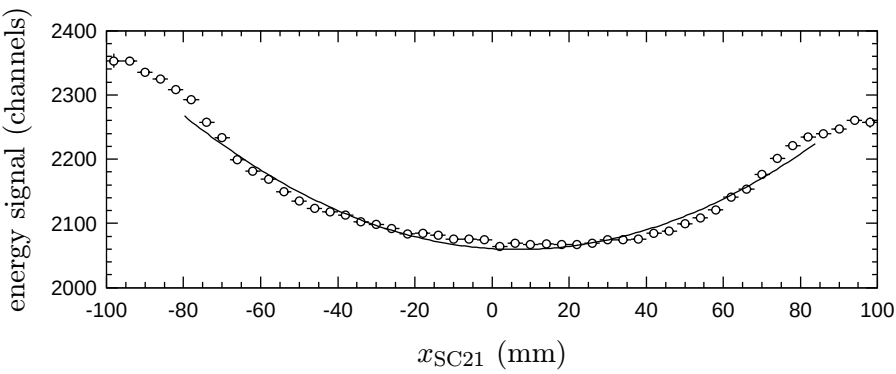

Figure 4.6: Raw energy signal of ^{40}Ar particles in scintillator SCI21 in dependence of the x-position of the beam. For particles penetrating the scintillator close to the edges, the light attenuation is smaller and the energy signal larger. The solid line shows a 2nd order fit that is used for a position correction.

rigidity,

$$\frac{\gamma m_0 v}{q} = \chi \,,$$

shows which variables have to be known in order to gain the charge q and the mass m_0 of the particle. At the relativistic energies that were employed in these measurements the fragments are completely ionized. In this case, the nuclear charge Ze with the proton number Z and the electron charge e equals the ion charge q.

The particle charge, or proton number, was determined with the MUSIC. The factor γ was deduced from the particle velocity v that needed to be measured. A position measurement together with the knowledge of the magnetic rigidity yielded the rigidity χ of each particle, complementing the complete identification.

Particle velocity

The particle velocity was obtained from a time-of-flight measurement between the scintillators SC21 and SC41, which were located at the mid-plane F2 and at the final focal plane F4.

Instead of the velocity, we use the ratio $\beta = v/c$, which can be calculated from the time of flight t if the time of flight in units of the speed of light, t_0, is known:

$$\beta = \frac{t_0}{t} \,.$$

The velocity of the particles also had to be known for the correction of the MUSIC energy signal.

Determination of the proton number

The energy signal of a particle penetrating an ionization chamber is roughly proportional to the square of the particle charge (see Sec. 4.2.2). For fully ionized heavy ions, the square root of the energy signal is therefore nearly proportional to the proton number. The MUSIC gives four energy signals, one for each anode. After subtracting an individual offset, which was deduced from the raw energy spectra, the geometric average of the four raw signals was calculated. Because the charge collection of the anodes decreases with the distance of the particle track to the anode, the energy signal is not constant over the x-range of the detector. The x-dependence of the averaged energy signal is plotted in Fig. 4.7. From this plot, we obtained a third order fit that was used to correct for the signal shift in dependence of the particle position.

We used the primary beam to calibrate the energy signal of the MUSIC. There are no contributions from different charge states at the energies where we performed these measurements, i.e. all ions we had to identify were fully stripped [69]. From the offset-corrected energy signal and the proton

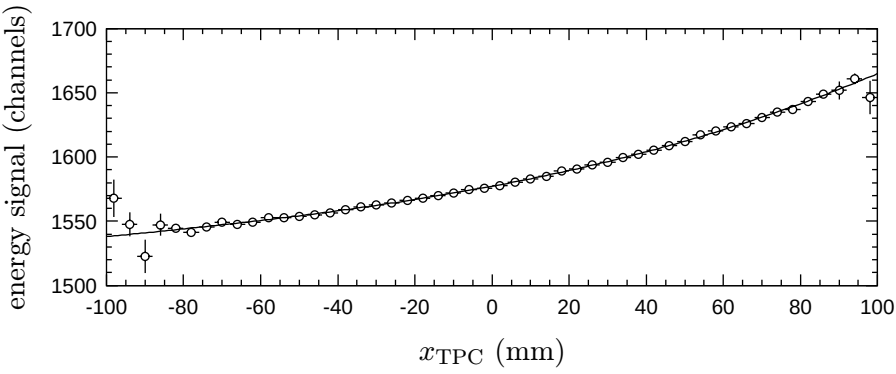

Figure 4.7: Energy signal of ^{40}Ar primary projectiles in MUSIC1 in dependence of the x-position of the beam. The solid line shows a third order fit that is used for a position correction.

number of the primary beam particle, we directly gained the calibration constant. But as pointed out in Sec. 4.2.2, the energy loss of the beam particles is velocity-dependent. We had to take this into account for the identification of the secondary beam particles.

For the velocity correction we used the primary beam with three different velocities that were achieved by changing the beam energy with different combinations of production and breakup targets. The three measurements gave the energy signal of the MUSIC for the primary beam particle in dependence of the velocity, as plotted in Fig. 4.8.

We employed the truncated Bethe-Bohr model (Eq. 4.3) for the extrapolation to other velocities. All the parameters that determine the shape of this curve were known, so it only had to be scaled to the measured data.

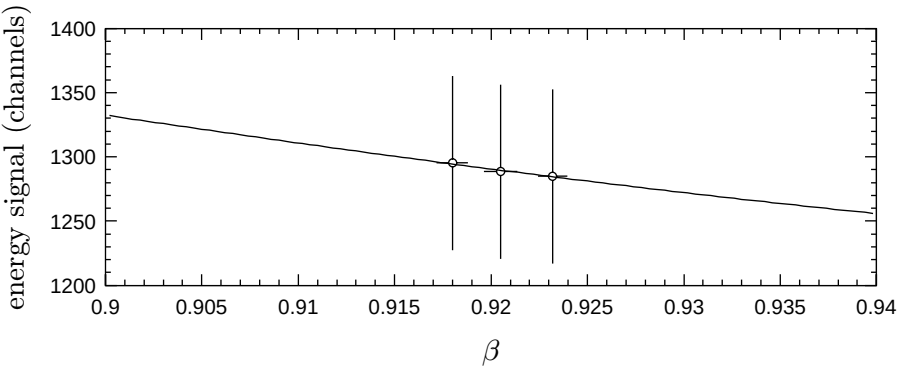

Figure 4.8: Energy signal of ^{12}C ions measured at three different velocities. The energy deposition according to the truncated Bethe-Bohr model (see Eq. 4.3) is fitted to the data points and plotted as a solid line.

Using a scale factor k, Eq. 4.3 can be abbreviated to

$$\Delta = k\beta^{-2}\left[\ln\frac{2m_e c^2 E_\mathrm{d}}{I^2} + 2\ln\beta - \ln(1-\beta^2) - 2\beta^2\right] .$$

Inserting the electron mass, $m_e c^2 = 0.511$ MeV/c^2, the ionization potential for argon (main constituent of the detector gas P10), $I = 188$ eV [1], and the empirical parameter $E_\mathrm{d} = 180$ keV [61] into Eq. 4.3, we can calculate the energy signal in dependence of β,

$$\Delta = k\beta^{-2}\left[15.46510 + 2\ln\beta - \ln(1-\beta^2) - 2\beta^2\right] . \tag{4.4}$$

With k determined by the measurements with the primary beam, Eq. 4.4 was used to correct the energy signal for slower particles.

Measurement of the mass-to-charge ratio

The mass-to-charge ratio is determined using the Lorentz equation, which describes the motion of charged particles in magnetic dipole fields,

$$F = qvB = \frac{mv^2}{\rho} = \frac{\gamma m_0 v^2}{\rho} ,$$

where ρ is the radius of the circular path of the particle in the magnetic field with the flux density B perpendicular to the direction of the particle motion. Solving for the mass-to-charge ratio m_0/q, we obtain

$$\frac{m_0}{q} = \frac{B\rho}{\gamma\beta c} , \tag{4.5}$$

where the magnetic rigidity $\chi = B\rho$ needs to be measured. To obtain values for the effective radii of the dipole magnets, a centered primary beam with its well defined energy and charge state was used. The magnetic fields of each dipole were measured with Hall probes and also could be deduced from the electric current of the power supplies using known field maps. With the effective radii and the magnetic field values, the magnetic rigidity χ_B of the particles on the central trajectory in the second spectrometer stage was calculated. Using the dispersion of the second spectrometer stage, $D_\mathsf{B} = (x|\delta)_\mathsf{B}$, and the measured particle positions at F2 and F4, x_F2 and x_F4, the fractional momentum deviation δ_F2, as defined in Eq. A.3, was determined for all particles that arrived at F4 (see Eq. A.8):

$$\delta_\mathrm{F2} = \frac{1}{D_\mathsf{B}}\left[x_\mathrm{F4} - (x|x)_\mathsf{B} x_\mathrm{F2}\right] . \tag{4.6}$$

It should be noted that at this stage of the analysis only theoretical values for the dispersion and the location of the image plane at F4 were available. For the particle identification, this was sufficient.

Solving

$$\delta_\mathrm{F2} = \frac{p - p_\mathsf{B}}{p_\mathsf{B}} = \frac{\chi - \chi_\mathsf{B}}{\chi_\mathsf{B}} \quad (\text{with} \quad q = q_\mathsf{B})$$

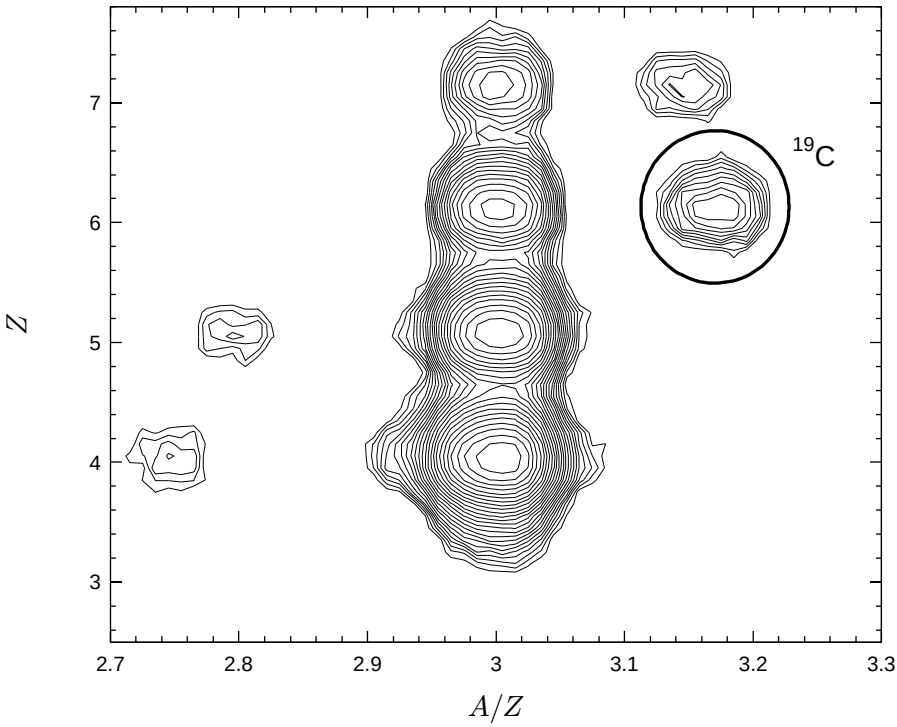

Figure 4.9: Two dimensional particle identification spectrum on a logarithmic scale. This spectrum was recorded with a setting for ^{19}C fragments from an ^{40}Ar primary beam. In order to facilitate the identification of the nuclei, the axes are labeled with A/Z and Z.

for the magnetic rigidity, we obtain

$$\chi = (1 + \delta_{\mathrm{F2}})\chi_{\mathrm{B}} \,. \tag{4.7}$$

Inserting into Eq. 4.5 finally yields

$$\frac{m_0}{q} = \frac{\chi_{\mathrm{B}}}{\gamma\beta c}(1 + \delta_{\mathrm{F2}}) \,. \tag{4.8}$$

Knowing the proton number and the mass-to-charge ratio, the particles are fully identified. A two-dimensional spectrum where the proton number Z is plotted versus the ratio of mass number and proton number, A/Z, was used in the analysis to apply a software-condition and separate the desired fragment (see Fig. 4.9).

Having described the selection of a specific fragment, we can move on to the next step of the analysis, the measurement of the x-distribution of the secondary beam particles and their breakup fragments.

4.5 Measurement of the position distribution

The measurement of the position distribution is the crucial step towards obtaining a momentum distribution as the latter is a mere transformation

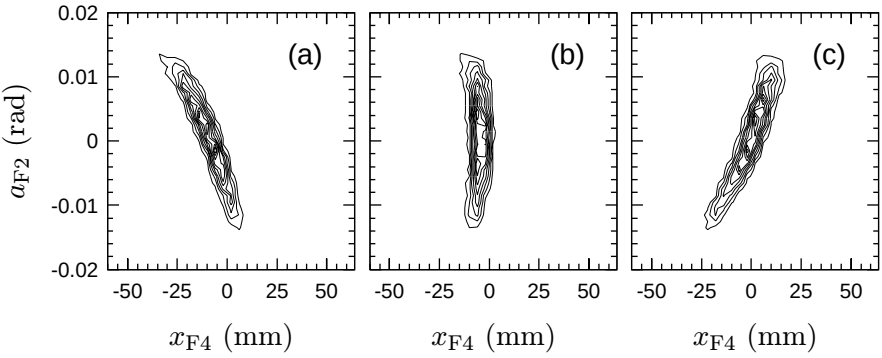

Figure 4.10: The three phase-space plots show the correlation between a_{F2} and x_{F4} for three different locations, 1 m before the image plane (a), at the image plane (b), and 1 m behind the image plane (c). The ellipse should be upright at the image plane, indicating that the x-position is not depending on the incident angle a_{F2}. This plot also shows aberrations of higher order that bend the ellipse and reduce the resolution. These spectra were recorded with a ^{19}C secondary beam.

of the position distribution. In order to measure x_{F4}, the particle positions recorded in TPC4 and TPC5 had to be projected onto the image plane. The image plane usually was not located at either one of the two detectors. For the identification of the magnetic rigidity described in the last section, the theoretical value for the location of the image plane was sufficient. But in order to yield the highest possible resolution for the momentum measurement, the image plane had to be determined from the experimental data.

4.5.1 Location of the image plane

To find the proper image plane, we should look for a definition that can be verified by our measurement. In Sec. A.4 it is pointed out that for a system with point-to-point imaging the matrix element $(x|a)$ has to be zero. This is the condition for the image plane. It means that the x-position at the image plane is independent from the incident angle of the beam, in this case the beam angle behind the breakup target. In order to investigate this, we plotted a_{F2} versus x_{F4} at different locations z at the F4-area. This plot showed a narrow ellipse, which was upright where the condition $(x|a) = 0$ was fulfilled. Consequently, the x-distribution was narrowest at this z-position. To look for the narrowest x-distribution of the beam is much simpler than an analysis of the ellipses. Figures 4.10 and 4.11 illustrate this.

4.6 Determination of the particle momentum

When the x-position of the breakup fragments at the image plane is known, the dispersion of the second spectrometer stage is, in principle, the missing

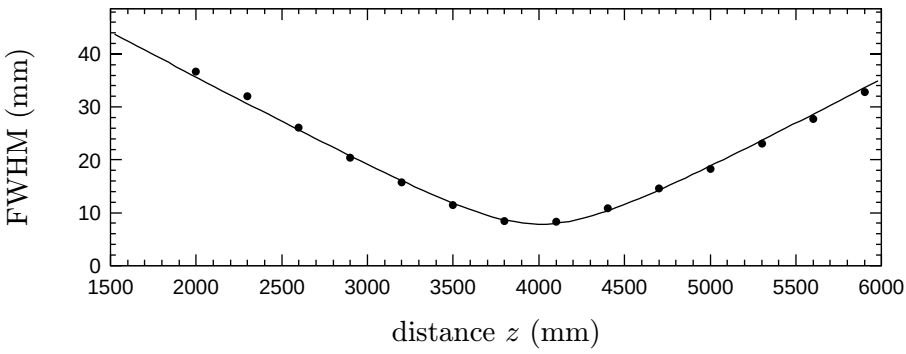

Figure 4.11: This plot shows the FWHM of the x-distribution at different locations z, measured from the last quadrupole magnet. The hyperbolic fit (solid line) is used to determine the position of the waist, which was found at around 4 m, in correspondence to the location of the image plane that is shown in Fig. 4.10.

link to the momentum. Due to the fact that the momentum $p_{\|}$ is determined to a large extent by the term $x_{\mathrm{F4}}/D_{\mathsf{B}}$ (see Eq. 3.6), x_{F4} and the dispersion D_{B} have to be known with a high precision. For this reason, the dispersion D_{B} was determined in a separate measurement.

4.6.1 Measuring the dispersion

The dispersion of the second spectrometer stage, i.e. from the mid-plane F2 to the image plane at F4, was measured with the secondary beam transmitted to the final focal plane. Two settings for the magnetic rigidity, χ_{B} and $\widetilde{\chi}_{\mathsf{B}}$, were used. Measuring the resulting positions of the beam, x_{F4} and $\tilde{x}_{\mathrm{F4}}$, the dispersion can be calculated applying Eq. 4.6:

$$\delta_{\mathrm{F2}} - \tilde{\delta}_{\mathrm{F2}} = \frac{1}{D_{\mathsf{B}}}(x_{\mathrm{F4}} - \tilde{x}_{\mathrm{F4}})\,, \tag{4.9}$$

$$D_{\mathsf{B}} = (x_{\mathrm{F4}} - \tilde{x}_{\mathrm{F4}})\frac{\chi_{\mathsf{B}}\widetilde{\chi}_{\mathsf{B}}}{\chi(\widetilde{\chi}_{\mathsf{B}} - \chi_{\mathsf{B}})}\,.$$

The variable χ denotes the mean value of the magnetic rigidity of the secondary beam particles.

This becomes much simpler if the beam is centered for one of the settings, the magnetic rigidity of the beam particles has to be measured anyway. So in the case where $\chi_{\mathsf{B}} = \chi$, x_{F4} is zero and we get

$$D_{\mathsf{B}} = -\tilde{x}_{\mathrm{F4}}\frac{\widetilde{\chi}_{\mathsf{B}}}{\widetilde{\chi}_{\mathsf{B}} - \chi_{\mathsf{B}}}\,. \tag{4.10}$$

Because the dispersion has to be measured at the image plane, and because it is not trivial to find the image plane for a beam with a broad distribution (as we did have for the breakup fragments), the dispersion was determined at various z-positions behind the spectrometer. Then, using the offset and the slope of the dispersion line, the actual value of the dispersion could be calculated at any position z.

4.6.2 Transformation into momentum space

Using the Eq. 3.9, the position of each particle that arrived at the final focal plane and that was properly identified was transformed to the longtudinal momentum of the breakup fragment in the projectile co-moving frame.

The momentum scale

It should be stated clearly that in the analysis performed here, the goal was to obtain the shapes and the widths of the momentum distributions. For this, the accurate determination of the *relative* momenta is sufficient. To obtain the momentum distributions on an absolute momentum scale is only possible if the velocity of the projectile at the position of the breakup is known. But with the atomic slowing down of the projectile in the relatively thick target, this can not be determined directly. Therefore, the experimental momentum distributions presented in this work are given on a momentum scale relative to the velocity of the emerging projectile that did not suffer a breakup reaction. In consequence, distributions that stem from a one-neutron removal are slightly shifted to negative momenta, due to the energy loss in the breakup reaction, while distributions from a one-proton removal are shifted to positive momenta because of the difference in slowing down for the projectile and the breakup fragment.

To finally obtain a momentum distribution, special care had to be taken to make sure that the transmission was constant within the covered range of momentum. The maximum momenta that are transmitted are smaller for fragments with large angles in the dispersive direction. This problem will be discussed in Sec. 5.2.

4.7 Limits of the momentum resolution

The momentum resolution that can be achieved in these measurements is defined by various factors, which are the resolution of the spectrometer itself, the quality of the primary beam (spot size and angular alignment), the amount of matter at the mid-plane that causes angular energy straggling, and the resolution of the position sensitive detectors.

Altogether, these influences vary the x-position of the particles at the image plane and limit the momentum resolution that can be achieved. Most of these contributions were quantified by a simple method: by transmitting the beam of those particles that do not react in the breakup target up to the final focal plane, the x-distribution measured reflects the system resolution, including the effects of the primary beam spot size, the ion-optical abberations, and the atomic straggling in the vacuum windows, detectors, and the breakup target itself. Also, the broadening due to differences in energy loss for particles of different energies is included. Such a measurement is presented in Fig. 4.12. The only effect which is not included is the *location straggling* that occurs in the breakup reaction.

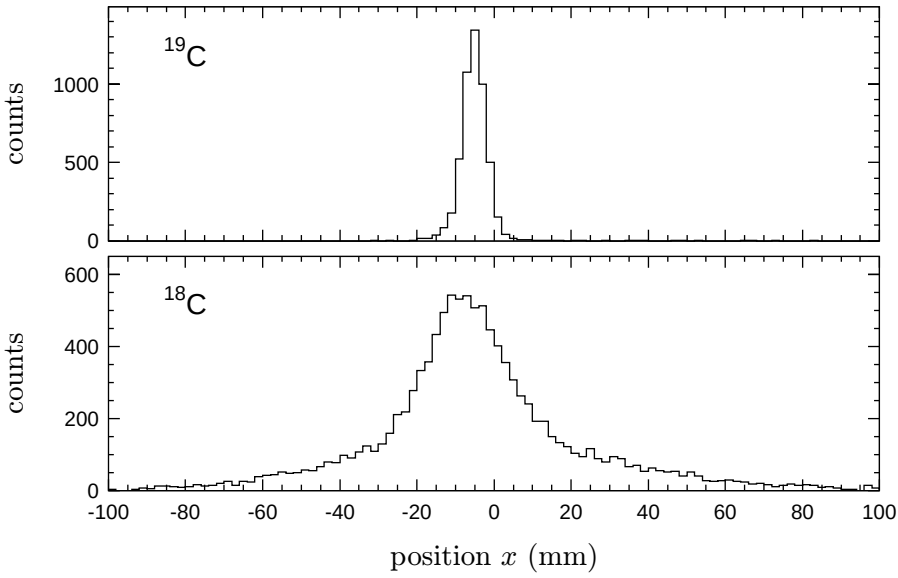

Figure 4.12: Measured x-position distributions of ^{18,19}C nuclei at the image plane F4. The top panel shows the position distribution of ^{19}C nuclei that passed through the breakup target without breakup reaction and reflects the system resolution. The bottom panel shows the distribution that was measured with the second spectrometer stage set for the ^{18}C breakup fragments.

Location straggling

Location straggling is the broadening of the energy distribution of the breakup fragments in thick targets. Because the stopping power dE/ds per nucleon is different for the projectile and the breakup fragment, the energy of the emerging fragment depends on where on the path through the target the breakup occured. Since the measurement of the system resolution described above did not include the breakup reaction, the effect of location straggling had to be calculated and added to the width of the measured resolution.

Figure 4.13 illustrates the effect of the location straggling for the case of a one-neutron removal from ^{19}C and also for the case of a one-proton removal from ^{8}B. It is clear that in cases where the measured resolution width is much larger than the width caused by location straggling, as is for the one-neutron removal, the effect of the location straggling can be neglected.

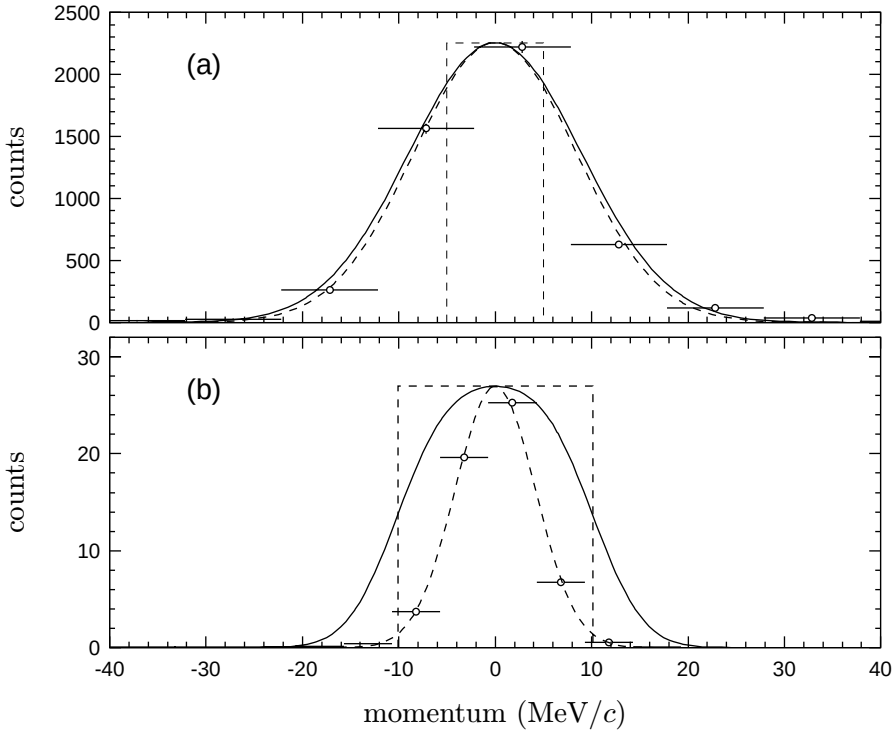

Figure 4.13: The two panels show the measured resolutions, transferred to a co-moving momentum scale, for the case of ^{19}C (a) and ^{8}B (b). A Gaussian fit to the data is plotted as dashed line. The calculated location straggling in a carbon target of about 4.4 g/cm^2 thickness is represented by the dashed step-function. The convolution of this step function and the Gaussian curve yields the total resolution and is plotted with a solid line.

Chapter 5

Analysis of the measured momentum distributions

While the last chapter described how the longitudinal momentum of each particle was obtained, this chapter will focus on the details of combining the information from many breakup reactions in order to produce a momentum *distribution*.

5.1 Definition of the reaction channel

In order to obtain a momentum distribution that has its origin in a specific breakup reaction, the reaction channel needs to be uniquely defined. In principle, this would demand a full particle identification in front of and behind the breakup target. Because of the limited acceptance of the spectrometer, and because we restrict ourselves to one-nucleon removal reactions, a full identification in front of the target is not necessary. A full particle identification is however needed at the final focus. The technical aspects of this are described in Sec. 4.3.2. I will further illustrate the definition of the reaction channel using the one-neutron removal from ^{19}C as an example.

In the case of ^{19}C, an ^{40}Ar primary beam was used and fragmented in a beryllium production target. In the fragmentation of ^{40}Ar, a considerable number of various nuclei is created. Because of the similar mass-to-charge ratio of some fragments, like ^{19}C and ^{22}N, and because of their broad velocity spread they are transmitted together with ^{19}C through the first spectrometer stage.

Because all particles arriving at the final focus can be fully identified, we only need to consider those secondary nuclei that can produce ^{18}C in the breakup target. In Fig. 5.1, panel (a), all isotopes that can fragment to ^{18}C are plotted versus their magnetic rigidity as they are emitted from the production target. These distributions were obtained in a Monte-Carlo simulation using the ion optical code MOCADI [38].

The carbon isotopes ^{18,19,20}C are plotted with solid lines, ^{19}C with a

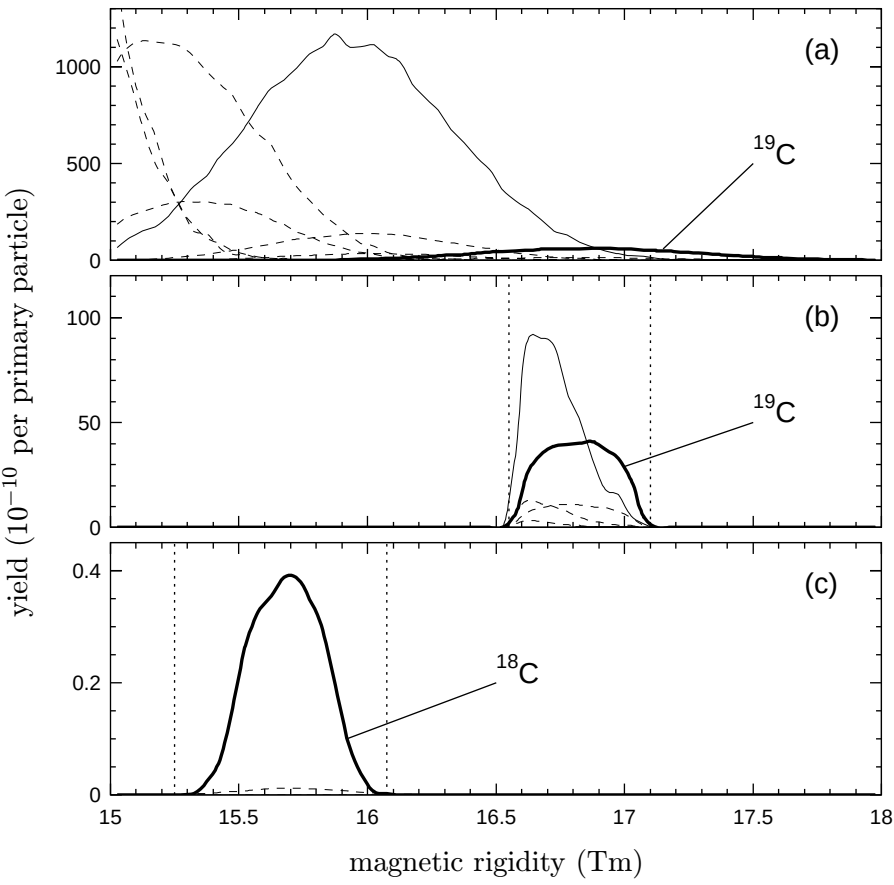

Figure 5.1: A MOCADI simulation illustrates how the reaction channel of the breakup reaction is defined. The distributions of those secondary nuclei which can fragment to ^{18}C in the breakup target are plotted on identical scales of magnetic rigidity at different positions: directly behind the production target (a), in front of the breakup target (b), and at the final focal plane (c). Solid lines denote the carbon isotopes ^{18,19,20}C, while dashed lines represent $^{19–22}$N and $^{22–24}$O. The thick solid line in panel (c) refers to the ^{18}C breakup fragments of ^{19}C.

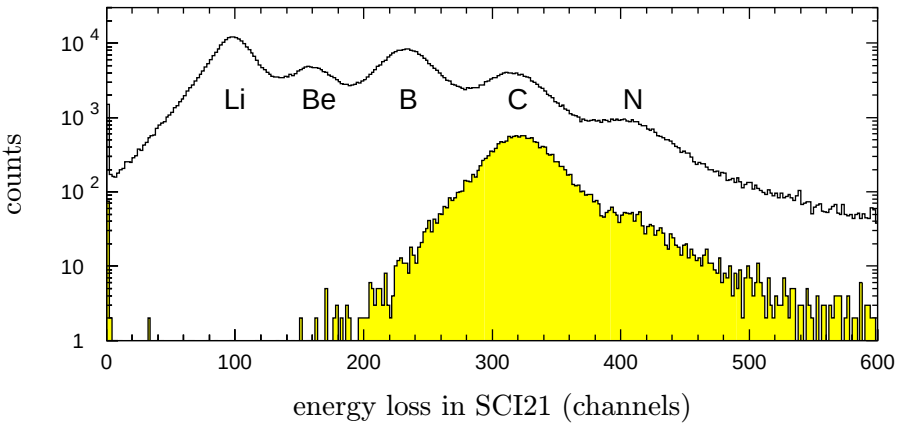

Figure 5.2: Spectrum of the energy loss in the scintillator before the breakup target (SCI21). The shaded spectrum represents those particles that are identified as ^{18}C at the final focus. There is only a small contribution from the fragmentation of nitrogen in the right tail of the carbon peak.

thick solid line, whereas the dashed lines represent $^{19–22}$N and $^{22–24}$O. Other isotopes that possibly could fragment to ^{18}C were found to have a negligible contribution. Panel (b) shows the situation in front of the breakup target. The dotted lines mark the limits of acceptance in the first spectrometer stage, corresponding to a setting for ^{19}C. Here, the major contaminant is ^{18}C (thin solid line) arriving from the production target.

In a one-neutron removal, however, the mass-to-charge ratio of ^{19}C is changed by more than 5%. Therefore, the ^{18}C nuclei from the production target that pass through the breakup target with no nuclear reaction lie well outside the magnetic rigidity window for the ^{18}C breakup fragments. Consequently, no ^{18}C fragments that arrive at the breakup target together with ^{19}C can reach the final focal plane. In the same way, ^{18}C reaction products from carbon isotopes other than ^{19}C are not transmitted through the second spectrometer stage.

However, this is not true for ^{18}C that stems from the fragmentation of ^{22}N. Because the production cross section of ^{22}N is much lower than that of ^{19}C, this caused only a contribution of few per cent in the measured ^{18}C momentum distribution (see Fig. 5.2). Using the Z-identification of the scintillator in front of the breakup target as described in Sec. 4.3.1, this contamination could be completely suppressed.

An equivalent investigation was necessary for the other breakup reactions that were studied, to make sure that the measured momentum distribution is not affected by contaminants.

5.2 Phase space acceptance considerations

In order to measure a momentum distribution, it is important that the transmission of particles is constant over the complete range of momentum that is covered, otherwise the shape of the distribution does not correspond to the momentum distribution of the fragments emerging the breakup target.

5.2.1 Limiting the phase space

Due to the limited apertures, the transmitted momentum range is reduced for particles with large angles. This becomes clearly visible in a plot of the angles a_{F2} (in x-direction) and b_{F2} (in y-direction) behind the breakup target versus the longitudinal momentum measured at the final focal plane, as shown in Fig. 5.3 for the transmission of ^{7}Be breakup fragments from ^{8}B. The transmitted areas display the shape of a polygon, or of a parallelogram with cut corners.

To preserve the shape of the momentum distribution, the angular range over which was integrated and the momentum range had to be limited. Two-dimensional plots of the kind presented in Fig. 5.3 provided a clear picture how the limits in angle and momentum had to be set. Figure 5.3 shows besides the complete area that was transmitted (filled grey boxes) also the areas that were accepted for the projection onto the momentum axis (filled and open black boxes). To extend the range of momentum that was covered by the measurement, the measurements with different settings of the magnetic rigidity were combined. This will be described in the following section.

5.2.2 Extending the momentum range

By scaling the magnetic rigidity of the second spectrometer stage, the acceptance window can be shifted along the momentum axis. Combining two (or more) measurements with different settings of the magnetic rigidity yields a momentum distribution with an extended momentum range. There are two aspects that have to be observed, the matching of the separate distributions in momentum space and the normalization of the count rates.

Matching the momentum scale

The formula that was used to compute the momentum (Eq. 3.6) takes the magnetic rigidity settings of the two spectrometer stages into account since it transforms the measured momentum into the projectile co-moving frame, which does not change with the different settings of the second spectrometer stage. Distributions that were taken at different settings "automatically" have matching momentum scales. This is shown in Fig. 5.4, where measured

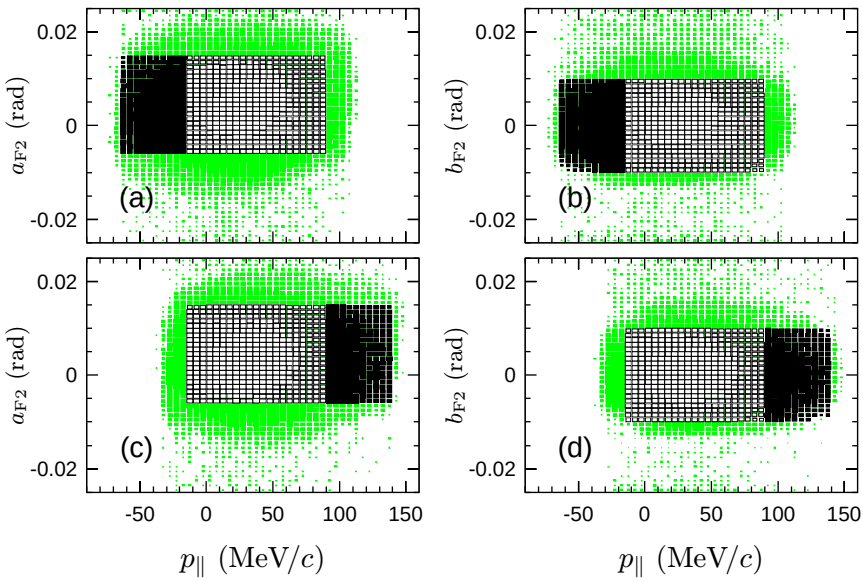

Figure 5.3: Shown here are two-dimensional spectra that visualize the acceptance windows of the second spectrometer stage. Plotted are the angles a_{F2} (left panels) and b_{F2} (right panels) vs. the longitudinal momentum of ^{7}Be fragments steming from the breakup of ^{8}B. Spectra (a) and (b) were recorded at a centered spectrometer setting, while the magnetic rigidity of the second spectrometer stage was scaled by 0.6% for spectra (c) and (d). The accepted area for the combined momentum distribution consists of three parts: the left wing, marked with filled black boxes in (a) and (b); the central part, which contains the overlap of the two settings and plotted with open boxes; and the right wing, represented by the filled black boxes in (c) and (d).

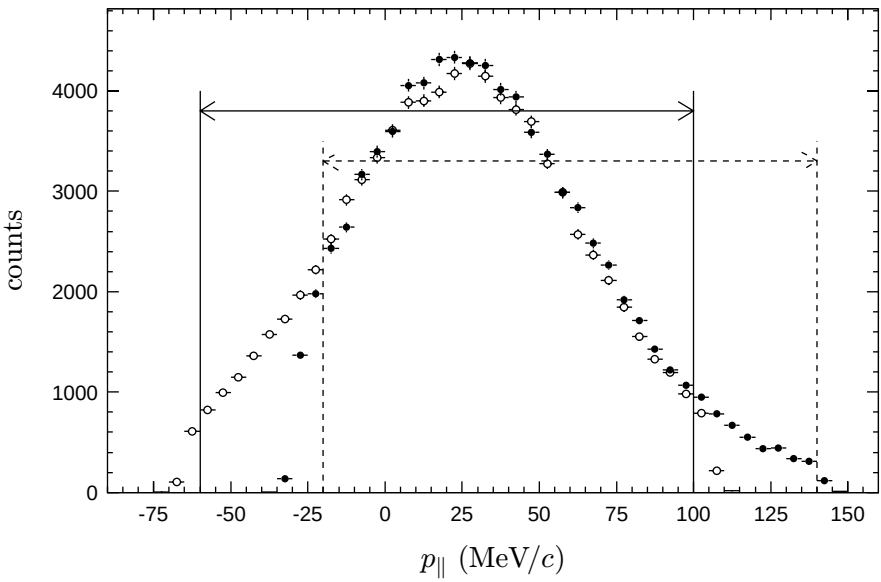

Figure 5.4: Momentum distributions of ^{7}Be fragments after ^{8}B-breakup from measurements at two spectrometer settings. The open symbols represent the distribution that was recorded at a centered setting; for the distribution marked by filled symbols, the magnetic rigidity of the second spectrometer stage was increased by 0.6%. The double-arrows indicate the corresponding acceptance windows. The data of the low-momentum setting (open symbols) and the high-momentum setting (filled symbols) were scaled to match in number of incoming projectiles.

momentum distributions from two different settings are plotted on top of each other.

Because the acceptance window was shifted only by small amounts, there is a large overlap between the two measurements. The boundary between the low-momentum setting and the high-momentum setting could be set anywhere within the overlap. To find the optimal position of this cut, the statistics in each setting should be considered.

In the described case, one would take the low-momentum distribution up to a certain momentum value, and the high-momentum distribution for the momentum intervall above this value. This method was applied in the case of the measurement of ^{18}C fragments from the ^{19}C breakup (please see Fig. 6.2).

Looking at the one-dimensional momentum distributions that have to be combined (as plotted in Fig. 5.4), a better solution is obvious, namely adding the statistics of the overlap region and thus making use of the full statistics accumulated in both spectrometer settings.

In this approach, the total distribution is a combination of *three* parts: the low-momentum wing from the first setting, the central part which is the sum of the distributions from both settings, and the high-momentum wing from the second setting. This is illustrated in Fig. 5.3, where the distri-

butions are shown in two-dimensional histograms that make the accepted area in the angle-versus-momentum planes visible.

Using a certain momentum value as a boundary yields a straight vertical cut in the angle–momentum planes, as can be seen in Fig. 5.3. But the two-dimensional spectra offer more advanced possibilities by employing graphical cuts.

A more complicated case

For one of the measurements of the longitudinal momentum distribution of ^{7}Be fragments from the breakup of ^{8}B, a modified ion-optics was used that is characterized by a smaller dispersion at the image plane. This produced a smaller image of the momentum distribution and as a result the acceptance area was not cut by the detector size.

On the other hand, the momentum-acceptance was strongly dependent on the angle and it was difficult to find a momentum range with a good transmission for a reasonable range of angles. For this reason, the method using certain momentum values as boundaries of the different distributions, like in Fig. 5.3, would have been inefficient. Employing graphical cuts which follow the acceptance windows was in this case advantageous.

Figure 5.5 shows how the boundaries were matched to the acceptance area in the a_{F2}-vs.-$p_{\parallel}$ plane (left column). Here it should be noted that the statistics in the tails of the distribution, i.e. distributions displayed in panels (c) & (e), are better than in the central region. This was taken into account by maximizing the contribution of the spectra (c) and (e). However, the statistics in the overlapping regions were not added.

Another specialty of this measurement is the fact that three settings were used, with the magnetic rigidity of the second spectrometer stage incremented in steps of 1%, each extending the momentum range by about 65 MeV/c in the projectile reference frame. These three distributions were combined to a momentum distribution with an unequaled momentum range (see Fig. 5.6).

Normalizing the distributions

It is clear that the different spectra had to be normalized before combining them to one momentum distribution. The fact that the first spectrometer stage, i.e. the elements from the production target up to the breakup target, were not changed and had an identical setting for each of the measurements that needed to be combined, provided a rather simple way of determining a normalization factor.

This factor was obtained by just taking the total number of particles that arrived at the mid-plane, as counted by the scintillator SCI21 in front of the production target, as a norm. Because the ratio of different nuclei transmitted through the first spectrometer stage was constant, no particle identification was needed to obtain the normalization factor, and thus the scaler values from the free trigger of SCI21 could be used. They needed,

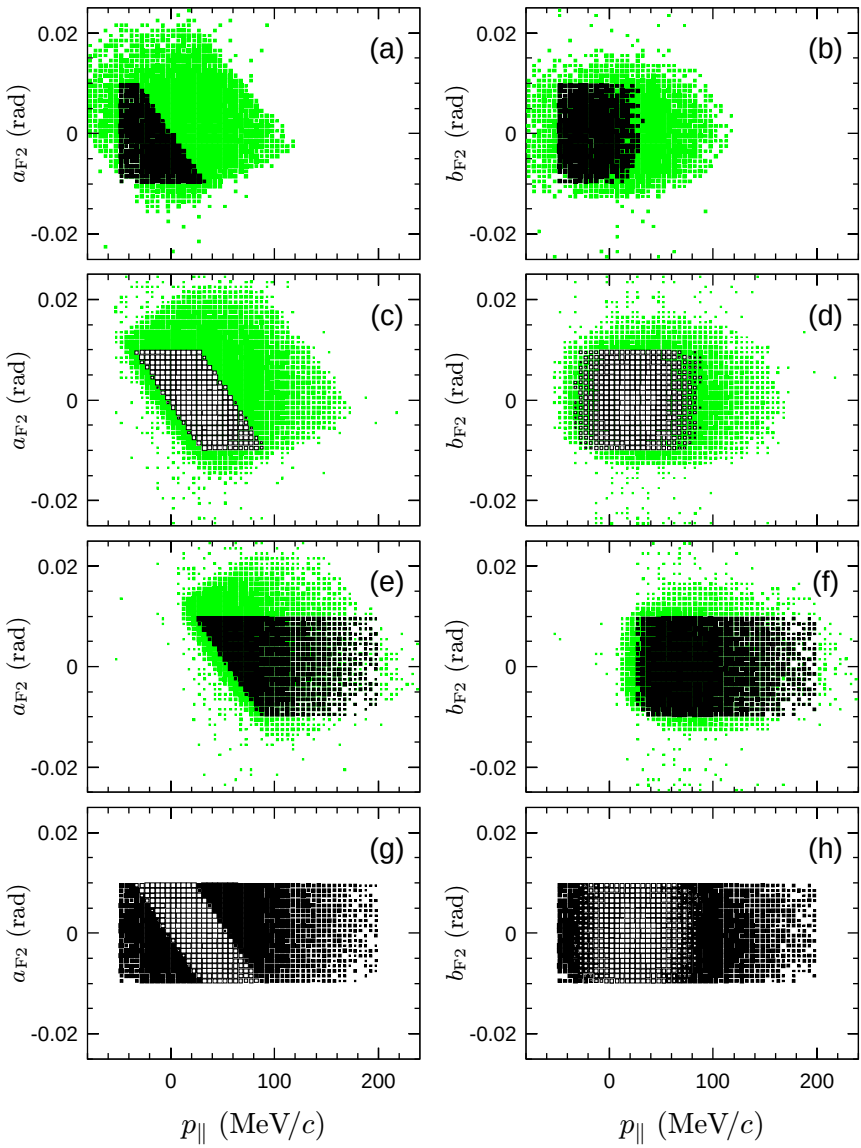

Figure 5.5: Acceptance windows in the angle-vs.-momentum planes for a measurement of ^{7}Be fragments from the ^{8}B breakup that was done in three steps. The left column shows plots of the x-angle a_{F2} behind the breakup target vs. the longitudinal momentum, while in the right column plots of the y-angle b_{F2} vs. $p_{\|}$ are shown. The three settings are displayed in the 1st, 2nd, and 3rd row. The panels (g) & (h) in the fourth row show the areas that are covered by the combination of all three settings.

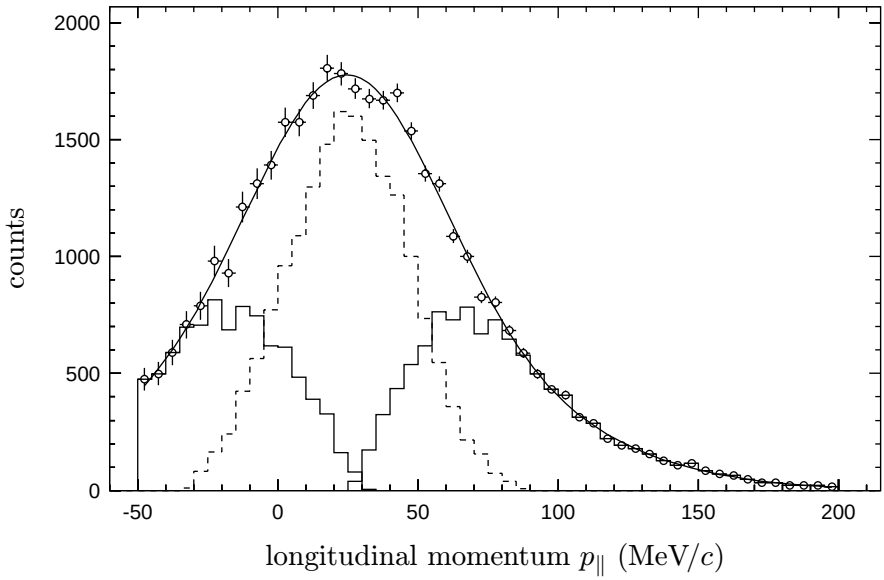

Figure 5.6: The histograms show the gated momentum distributions of ^{7}Be breakup fragments from ^{8}B, measured at three different settings of the magnetic rigidity in the second spectrometer stage. The sum of these histograms yields the complete distribution, as is demonstrated in Fig. 5.5, and is marked with open circles.

however, to be corrected for the dead time of the data acquisition system, as this varied with the beam intensity. Two distributions from different spectrometer settings that were normalized to the SCI21 free scaler are shown in direct comparison in Fig. 5.4.

5.3 System resolution

In Sec. 4.7, it was discussed how to determine the resolution of the system, including the measured effects and the calculated location straggling. The obtained function can be regarded as a *response function* of the system, meaning that all measured momentum distributions are broadened by the convolution with this response function.

The question now is how to deal with this response function in the analysis. The straight-forward method would be, of course, to unfold the measured spectra. Then one would obtain the "true" momentum distribution of the breakup fragment, which would be very nice. However, in this case the straight-forward method is quite complicated, and one should reconsider if it is advantageous to correct the measured data points. A deconvolution of a discrete set of data, including the statistical errors, is not trivial, and the result is not always satisfying. Therefore, from my point of view, it is much better to leave the measured distribution untouched and fold the theoretical distribution before comparing with the experimental

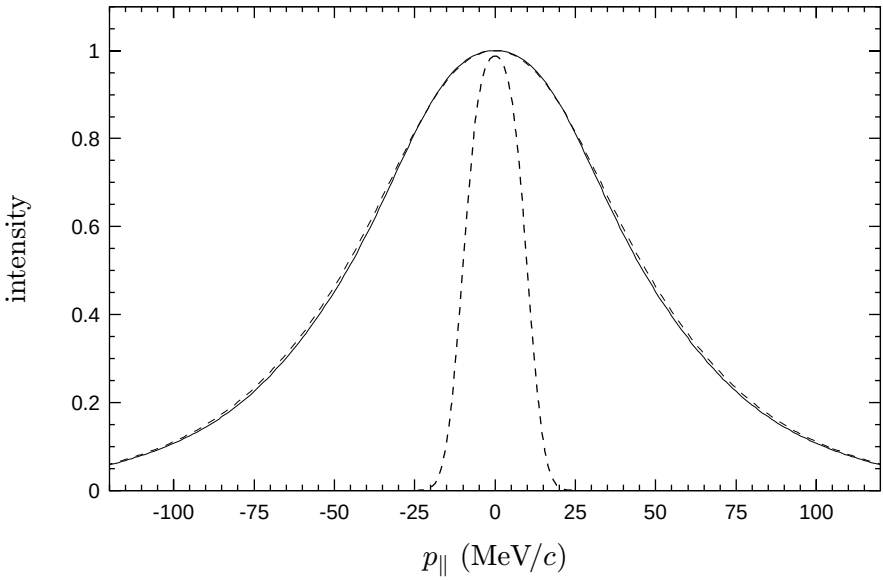

Figure 5.7: The plotted curve (solid line) is a calculated momentum distribution for the core fragments of a ^{8}B one-proton removal. The narrow dashed curve gives the measured system resolution convoluted with the location straggling contribution. To obtain a momentum distribution that can be compared with the measured one, the calculated curve needs to be folded with the system resolution. The result is the dashed distribution which is slightly broader than the pure theoretical distribution.

data. In any case, the effect of the response function is small, as a look at Fig. 5.7 proves.

In cases where not the complete distribution, but only the value of its width is needed, a simple correction for the resolution by quadratic subtraction of the variances can be done.

Chapter 6

Results on ^{19}C

The methods described in this work in the Chapters 2 to 5 were applied to investigate the nucleus ^{19}C, which has been reported to be a one-neutron halo nucleus [14,13]. Together with ^{19}C, the heaviest bound carbon isotope with odd neutron number, we also investigated ^{17}C, the next neighbor with odd neutron number, and the tightly-bound ^{12}C.

This chapter will present the results that were collected on longitudinal momentum distributions and compare them with other measurements as well as theoretical calculations [10, 11].

6.1 ^{19}C – a special case

The nucleus ^{19}C has attracted much attention since narrow momentum distributions, that were measured for the ^{18}C breakup fragments [14] as well as for the neutrons [50], were taken as evidence for a one-neutron halo structure.

Before these findings, only one case of a one-neutron halo had been confirmed experimentally, namely ^{11}Be [3]. The nucleus ^{11}Be has also been

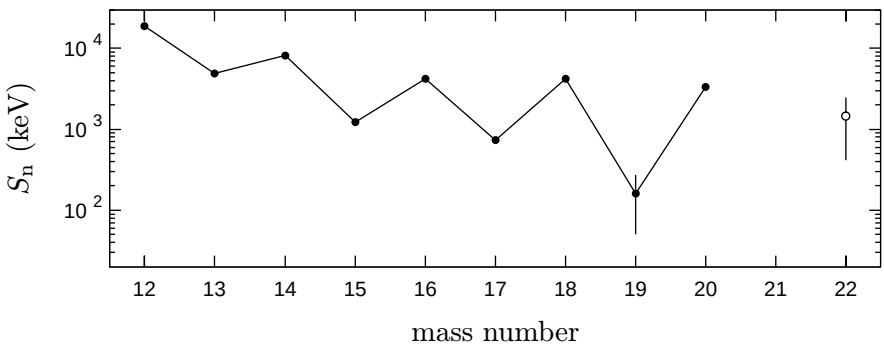

Figure 6.1: One neutron separation energies S_n for the neutron-rich carbon isotopes [8].

subject to extensive theoretical studies [5,26,80,34,59] and has provided a theoretical testing ground for one-neutron halo states.

In this context, ^{19}C is indeed a very interesting case to study. Its one-neutron separation energy of 162±112 keV is one order of magnitude smaller than that of the core, ^{18}C, which is 4184 ± 35 keV (values are from the NUBASE evaluation [8]). It is the smallest one-neutron separation energy of all carbon isotopes and, even though it is not known very accurately, it appears to be smaller than the 503 ± 6 keV of ^{11}Be.

So far the theoretical investigations have been hampered by the sparse experimental data that is available and could not reach final conclusions for the structure of ^{19}C [63,64].

6.2 The experiment

We produced secondary beams of ^{17}C and ^{19}C by fragmentation of an ^{40}Ar primary beam at 1.0 GeV/u. The primary beam was delivered by the heavy-ion synchrotron SIS with an intensity of about 8×10^9 particles per spill. The production target used was beryllium with a thickness of 6.33 g/cm^2. The experimental setup is shown in Figs. 3.1, 4.4, and 4.5.

The secondary beam of ^{19}C had an energy of 911 ± 10 MeV/u at the breakup target, while ^{17}C arrived there with 903 ± 10 MeV/u. The energy spread at the breakup target is limited to about 4% (full width) by the acceptance of the first spectrometer stage. Both nuclei impinged on a carbon breakup target of 4.45 g/cm^2 thickness.

6.2.1 Longitudinal momentum distribution from the breakup of ^{19}C

The longitudinal momentum distribution of ^{18}C fragments from the breakup of ^{19}C was measured with two different settings of the spectrometer stage behind the breakup target. Besides the centered setting, we scaled the magnetic rigidity by 0.5% in order to extend the measurement to higher momenta. The data obtained at the second setting were scaled and added to form the complete momentum distribution, as described in Sec. 5.2.2. The complete longitudinal momentum distribution is shown in Fig. 6.2.

The measured momenta are transformed into the projectile co-moving frame. The distribution can be described well by a Lorentzian curve with a full width at half maximum (FWHM) of 71 ± 3 MeV/c. The measured system resolution folded with the location straggling in the relatively thick breakup target results in a FWHM of 19.9 MeV/c. In this case, the contribution of location straggling is actually negligible. A correction of the measured width for the determined resolution (by quadratic subtraction of the variances) yields a FWHM of 69 ± 3 MeV/c.

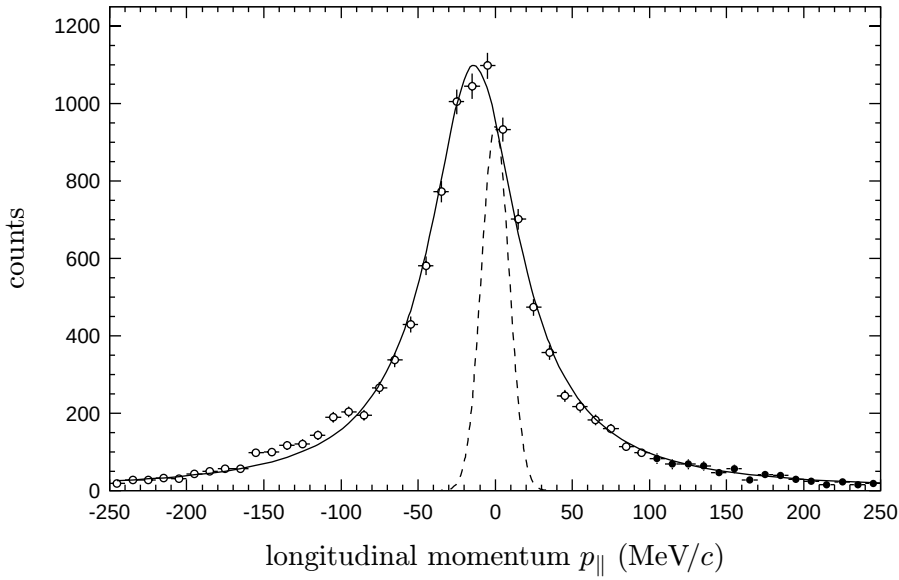

Figure 6.2: Longitudinal momentum distribution of ^{18}C fragments from the breakup of ^{19}C on a carbon target. The distribution is transformed into the projectile frame. Filled circles mark those data that were added to the distribution by the second spectrometer setting. A Lorentzian fit to the distribution is plotted as a solid line. The FWHM of the fit is 71 ± 3 MeV/c. The dashed profile represents the measured system resolution with a FWHM of 19.9 MeV/c.

6.2.2 Longitudinal momentum distribution for ^{17}C

For the measurement of the longitudinal momentum of ^{16}C fragments after a one-neutron removal from ^{17}C nuclei, only one setting was used. The observed momentum distribution follows neither a Lorentzian nor a Gaussian curve. However, fitting with the sum of two Gaussian components, the experimental data can be described satisfactorily and a FWHM value of 145 ± 6 MeV/c is extracted. Taking the resolution of 18.5 MeV/c (FWHM) into account, a corrected width of the ^{16}C momentum distribution of 143 ± 6 MeV/c can be stated. The plot of the measured distribution together with the fit is presented in Fig. 6.3.

6.2.3 Comparison of the results

The measured longitudinal momentum distribution for the ^{19}C breakup is narrow compared to the ^{17}C case – in fact, it is about half as wide. This directly reflects the difference in binding energy for the last neutron, which is 728 ± 17 keV in the case of ^{17}C, but only 162 ± 112 keV for ^{19}C.

A comparison with the tightly-bound nucleus ^{12}C, which is well-described by simple theories, is very interesting as it shows the validity of the extracted momentum distributions and the special character of the loosely bound systems ^{17}C and ^{19}C. We measured the breakup of ^{12}C nuclei at

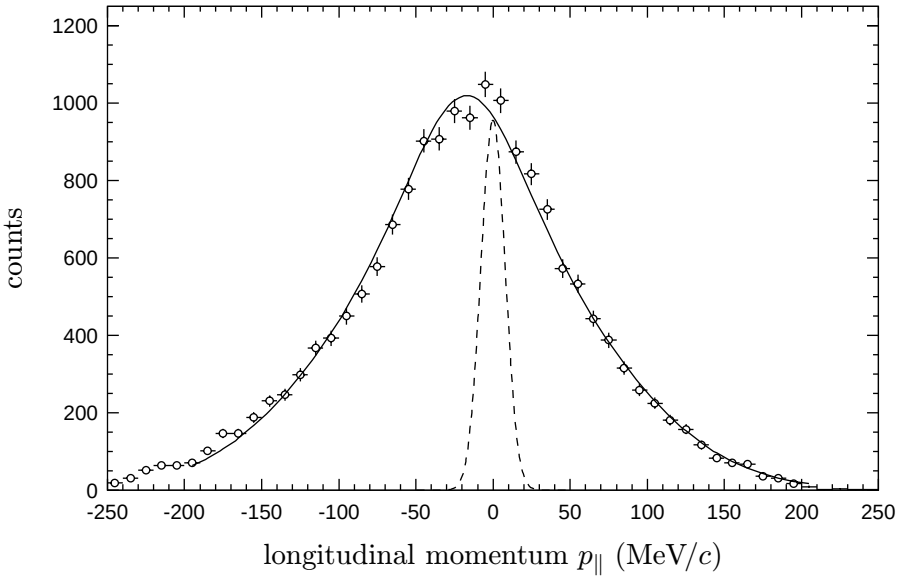

Figure 6.3: Longitudinal momentum distribution of ^{16}C measured after the one-neutron removal from ^{17}C in a carbon target. The momentum distribution is transformed into the projectile frame. The solid line is a double-Gaussian fit to the data that has a FWHM of 145 ± 6 MeV/c. As a dashed curve, the profile of the system resolution with a FWHM of 18.5 MeV/c is shown.

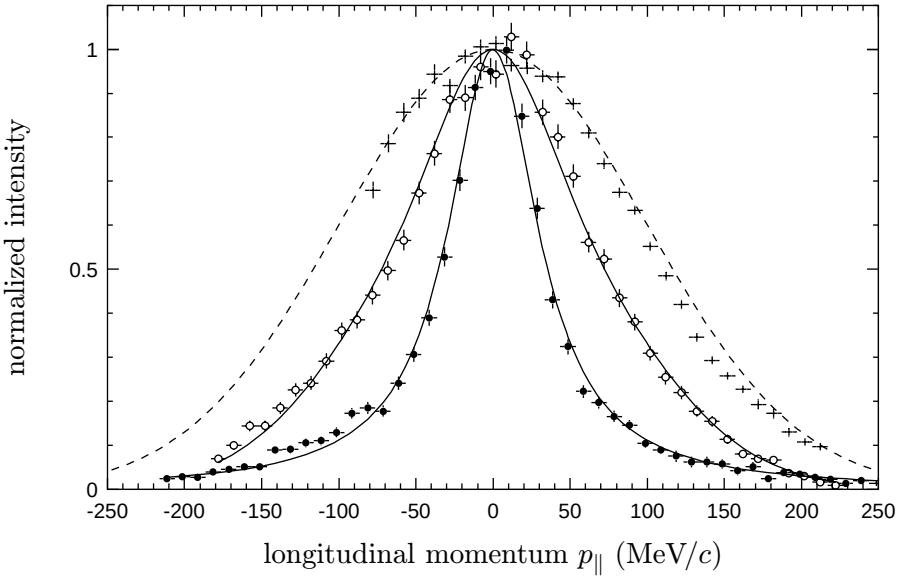

Figure 6.4: Longitudinal momentum distributions of breakup fragments from the one-neutron removal reactions in ^{17}C (open symbols) and ^{19}C (filled symbols), both measured on a carbon target. The crosses mark the measured momentum distribution for the breakup of ^{12}C in a CH_2 target that agrees nicely with Goldhaber systematics (dashed line). All distributions are normalized at the maxima and centered for the comparison of shapes.

1460 MeV/u in a CH_2 target (polyethylene) using the same setup. The longitudinal momentum distribution was analyzed in the same manner as for the ^{17,19}C nuclei. The obtained momentum distribution has a FWHM of 220 ± 12 MeV/c and agrees nicely with the 233 MeV/c that the Goldhaber model predicts [31], using a Fermi-momentum of $p_F = 221$ MeV/c from Ref. 53. The three measured distributions, normalized to the maxima, are plotted together with the Gaussian momentum distribution given by the Goldhaber model (dashed curve) in Fig. 6.4.

Figure 6.5 shows a comparison of the momentum distributions for the case of ^{12}C and ^{19}C, this time on an absolute scale. The integrals of the analytic functions that describe the measured data were scaled to the corresponding one-neutron removal cross sections in order to quantitatively compare the distributions. For this rough comparison, I took the one-neutron removal cross section for ^{12}C on a carbon target of 44.7 ± 2.8 mb that was measured at 1.05 GeV/u [40]. The one-neutron removal cross sections of ^{17}C and ^{19}C were measured together with the longitudinal momentum distributions. For ^{17}C and ^{19}C, values of $\sigma_n = 129 \pm 22$ mb and 233 ± 51 mb, respectively, were deduced [22].

This plot shows nicely how the increased cross section and the small

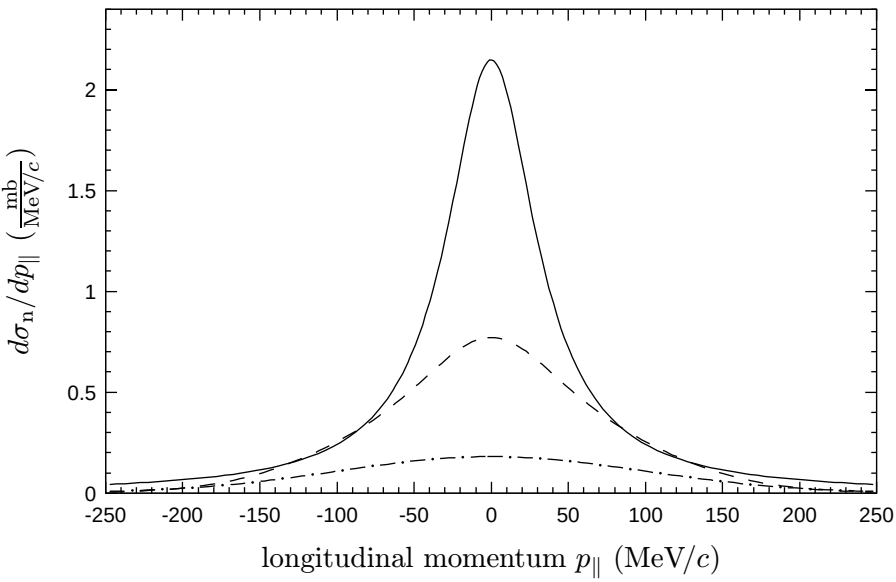

Figure 6.5: Momentum distributions from the ^{17,19}C and ^{12}C breakup reactions on carbon targets on an absolute scale of the one-neutron removal cross section. The curves are the fits to the measured data, scaled with measured cross sections. For the one-neutron removal cross section of ^{12}C (dot-dashed line), a value of 44.7 ± 2.8 mb was taken from Ref. 40. The one-neutron removal cross sections of approximately 130 mb for ^{17}C (dashed line) and 230 mb for ^{19}C (solid line) were deduced in this measurement. For information on the cross section measurement, see Appendix B.

width that is observed in breakup reactions of loosely bound systems form a prominent momentum distribution compared to tightly bound nuclei.

6.3 Comparison with other measurements

Although the amount of experimental data on ^{19}C is small, at least two measurements of momentum distributions exist momentarily that our data can be compared with.

6.3.1 Breakup at lower energies: the MSU results

The first measurement of the longitudinal momentum distribution of ^{18}C fragments from the breakup of ^{19}C was undertaken at Michigan State University (MSU) in 1995 and started the large interest in this nucleus, because a very narrow momentum width of only 44.3 ± 5.9 MeV/c was stated [14]. The data was later re-analyzed and the value that should be quoted is 42 ± 4 MeV/c in the center-of-mass frame [13]. This measurement was done with a projectile energy of 77.2 MeV/u and a beryllium breakup target, using the magnetic spectrometer A1200 of the National Superconducting Cyclotron Laboratory.

The nucleus ^{17}C was investigated at MSU as well, at a beam energy of 84 MeV/u [13]. For the ^{16}C fragments from the breakup of ^{17}C in a

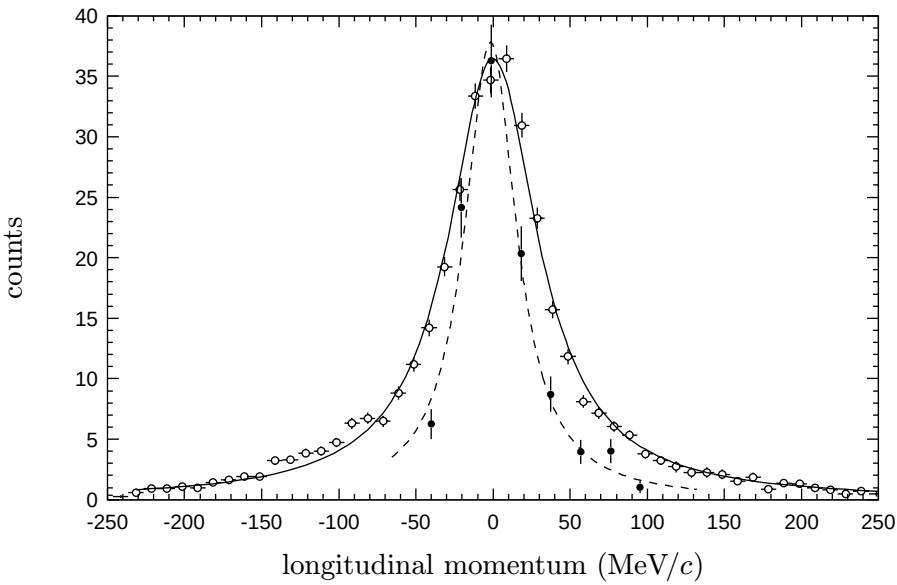

Figure 6.6: Data from the breakup of ^{19}C on a beryllium target at 77.2 MeV/u measured at MSU (filled symbols) [14, 13] in comparison with the distribution obtained in this work (open symbols). Both distributions were centered and our data is scaled to the MSU data. A pure Lorentzian with a FWHM of 41 MeV/c is plotted as a dashed line.

beryllium target, a FWHM of the parallel momentum distribution of 145 ± 5 MeV/c (c.m. system) was measured.[1] This result is in perfect agreement with our measurement.

The ^{18}C distribution in Ref. 13 is given on an absolute momentum scale. In order to compare it with our distribution measured at much higher energies, it was transformed into the co-moving frame. Figure 6.6 shows a direct comparison of the low-energy data with the distribution obtained in this work.

It should be noted, however, that a direct comparison faces some problems. First, to deduce the width from the MSU data, a modified Lorentzian line shape was used that takes effects of the limited angular acceptance of the spectrometer into account. As a result of this, the stated FWHM is slightly larger. Second, the statistics and the momentum range covered are very different and one should take this into account when comparing the two distributions.

Nevertheless, the discrepancy between the two ^{19}C measurements is apparent. In earlier measurements of longitudinal momentum distributions for the halo nuclei ^{11}Be and ^{11}Li, no significant dependence of the width on beam energy or target material was observed [27]. This is in accordance with the results for the ^{17}C breakup, that are within the errors identical at 84 MeV/u and 903 MeV/u projectile energy.

Both, theoreticians and experimentalists are working on the solution of this puzzle. The possibility of a low-lying resonant state in ^{19}C is considered (see Ref. 72 and Sec. 6.4.1), while at the NSCL a second generation of breakup measurements using the S800 spectrometer together with a γ-ray detection is being analyzed.

6.3.2 Neutron momentum distributions

The second measurement of momentum distributions where ^{19}C was investigated did not measure the momentum of the core-fragments but that of neutrons after a "core-breakup" reaction [50]. The ^{19}C energy was in this case 36.3 MeV/u and a tantalum breakup target was used. Core breakup means that in the breakup reaction the ^{18}C core is destroyed, freeing the valence neutron. A neutron-detector array was employed to measure the angles of the outgoing neutrons, from which the transverse momentum could be deduced. In principle, the transverse momentum distribution should be comparable to that of the longitudinal component. The momentum width that was found for neutrons from the ^{19}C breakup is 64 ± 17 MeV/c. This value is in accordance with our result.

However, it is evident that in this measurement the reaction channel is not well-defined as it is impossible to discriminate neutrons that come from any core breakup. Therefore, the measured momentum distribution should

[1] A longitudinal momentum distribution for ^{17}C was already published in Ref. 14, but due to a poor particle identification this result was revised in Ref. 13 and is therefore not mentioned here.

consist of two components, a broad component from neutrons steming from the ^{18}C core and a narrow component from the loosely bound halo neutrons.

With this in mind, the authors were able to fit the experimental data with a broad component of 165 ± 17 MeV/c and a narrow component of 42 ± 12 MeV/c, which agrees with the result of Ref. 14. The problem with this interpretation, from my understanding, lies in the relative cross sections for the one-neutron removal that had to be assigned to the two components. The values stated in Ref. 50 are 0.24 ± 0.11 b for the narrow and 2.2 ± 0.3 b for the broad component, while for a one-neutron removal from the relatively tightly-bound ^{18}C a much smaller cross section should be expected, compared to the loosely bound ^{19}C.

In this case, the influence of the broad momentum distribution from core neutrons would be smaller and consequently a larger width would have to be assigned to the distribution of the valence neutrons. Considering the statistics, it is very difficult to determine the widths of two components and the ratio of their contribution from this data.

6.4 Theoretical calculations for ^{19}C

After the one-neutron halo in ^{11}Be could be described rather well by theories [26, 80, 59, 65, 47], similar models were applied to describe the structure

Table 6.1: This table lists the momentum widths that were obtained for the one-neutron removal from ^{17,19}C in different experiments. To compare with, the value for the ^{12}C one-neutron removal from this work is listed as well. Please note that the FWHM-value alone does not completely determine the distribution. Remarks on the shapes of the distributions are given in the footnote.

Projectile	Energy (MeV/u)	Target	FWHM (MeV/c)	Ref.
^{12}C	1460	CH_2	220 ± 12^a	this work
^{17}C	84	Be	145 ± 5^b	[13]
^{17}C	903	C	143 ± 6^c	this work
^{19}C	36	Ta	64 ± 17^d	[50]
^{19}C	77	Be	42 ± 4^b	[13]
^{19}C	88	Ta	41 ± 3^b	[13]
^{19}C	911	C	69 ± 3^e	this work

[a] Gaussian
[b] modified Lorentzian [13]
[c] double Gaussian
[d] two Gaussian components [50]
[e] Lorentzian

of ^{19}C [63]. However, due to the limited data available the theoretical investigations could not resolve the ground state configuration of ^{19}C.

The structure of ^{19}C seems to be more complicated than a simple particle-plus-core model suggests, as the core itself, ^{18}C, is already far from stability. There is a low-lying 2^+ state at 1.62 MeV, which indicates that core-polarization might play an important role. The last neutron of ^{19}C is expected to be bound mainly in a $1s_{1/2}$, $0d_{5/2}$ or $0d_{3/2}$ state, coupled to the 0^+ ground state or the 2^+_1 first excited state of the ^{18}C core. Because the spin and parity of the ^{19}C ground state are still unknown, a number of different combinations is possible.

If the valence neutron was bound in a *d*-state, the angular momentum would confine the neutron closer to the core, leading to a wide momentum distribution with a width of the order of 200 MeV/c. Only an *s*-state could produce a narrow distribution, but this would have a width of about 30 MeV/c if coupled to the 0^+ ground state of ^{18}C. This would be too narrow to reproduce the recent results for the momentum distribution. The solution could be a dominant contribution of valence neutron states coupled to the first excited state of ^{18}C. The additional binding of the valence neutron causes a smaller spatial distribution and consequently results in a broadened momentum width.

But here the reaction part needs to be considered as well. The core-shadowing will have a larger effect on broad momentum distributions from *d*-states, while momentum distributions connected to an *s*-state are almost unchanged.

6.4.1 Coupled channels calculation

M. H. Smedberg *et al.* used Hankel radial wave functions, which are the exact solutions of the Schrödinger equation outside the range of the nuclear potential, to calculate the momentum distribution of the core fragment after the ^{19}C breakup [10, 72]. In the transformation of the wave function into the momentum coordinates, a cylindrical segment was cut out of the wave function to account for the core shadowing. The cut-off radius was

Table 6.2: Two possible configurations for the ^{19}C ground state are listed in this table. The resulting spin and parity of the ^{19}C g.s. are given in the right column.

^{18}C J^π	neutron $n\ell_j$	^{19}C J^π
2^+	$1s_{1/2}$	$3/2^+, 5/2^+$
2^+	$0d_{5/2}$	
0^+	$1s_{1/2}$	$1/2^+$
2^+	$0d_{5/2}$	
2^+	$0d_{3/2}$	

estimated from the sum of the core and target radius.

The measured momentum distribution could be reproduced with a $2s_{1/2}$ neutron coupled to the 2^+_1 excited state of ^{18}C as the dominating contribution (with about 65%), yielding a J^π of $3/2^+$ or $5/2^+$ for the ^{19}C ground state.

The most recent calculations, where a low lying resonance state in ^{19}C is assumed at about 0.2 MeV, seem to be able to explain an energy dependence of the measured momentum width [72, 74]. In this picture, the breakup reaction will go partly through this resonant state, in which case the momentum distribution of the core fragments is narrower. At lower beam energies, a larger part of the breakup reactions will involve this resonance, while at higher beam energies nuclear stripping plays the dominant role.

This assumption could be experimentally tested with improved detector setups that record the γ rays from the de-excitation of core fragments at the breakup target, enabling the discrimination of certain reaction channels that involve excited states.

6.4.2 Dynamical core polarization

H. Lenske described the coupling of single particle configurations to excitations of the core nucleus by dynamical core polarization (DCP) in a mean-field and quasi-particle random phase approximation (QRPA) theory [47].

In this calculation, the core–particle interactions were obtained microscopically from random phase approximations (RPA) [48]. This leads to non-static and non-local self-energies which extend the nuclear mean-field description beyond the static Hartree-Fock approach. Dynamical core polarization is well understood for stable nuclei, where it is found to describe rather accurately single particle strength distributions of odd mass nuclei as for example in Refs. 20, 24, 23, 58.

In the DCP approach, the calculations predict a $1/2^+$ ground state obtained at a separation energy $S_\mathrm{n} = 183$ keV for ^{19}C [48]. The first $5/2^+$ state is found about 300 keV above the ground state and is located just beyond the continuum threshold. The $^{18}\mathrm{C}(0^+) \otimes 1s_{1/2}$ leading particle configuration accounts for only 40% of the wave function, while the $^{18}\mathrm{C}(2^+_1) \otimes 0d_{5/2}$ core excited configuration accounts for the major part of the ^{19}C ground state.

The calculation of the longitudinal momentum distribution takes the dynamics of high-energy breakup reactions into account. The breakup reactions are described in an eikonal distorted wave approach. Figure 6.8 shows two calculated momentum distributions that would result from the removal of an s- or d-neutron. The dashed lines represent the momentum distributions in the transparent limit, when no final state interaction or core shadowing is taken into account. The final state interaction tends to broaden especially the momentum distributions from s-states, while the

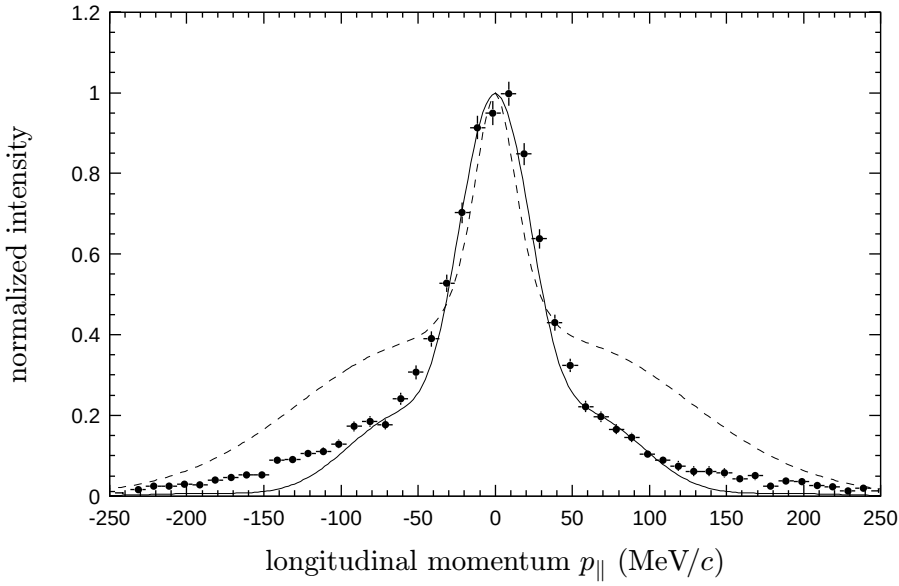

Figure 6.7: The result of the DCP-calculation by H. Lenske as compared to the experimental longitudinal momentum distribution of ^{18}C from the breakup of ^{19}C in a carbon target [47,10]. The solid line shows the distribution obtained from the calculation that takes the reaction mechanism with a carbon target (core shadowing and final state interaction) into account. The dashed line is the distribution in the transparent limit, i.e. without the effects of the reaction mechanism.

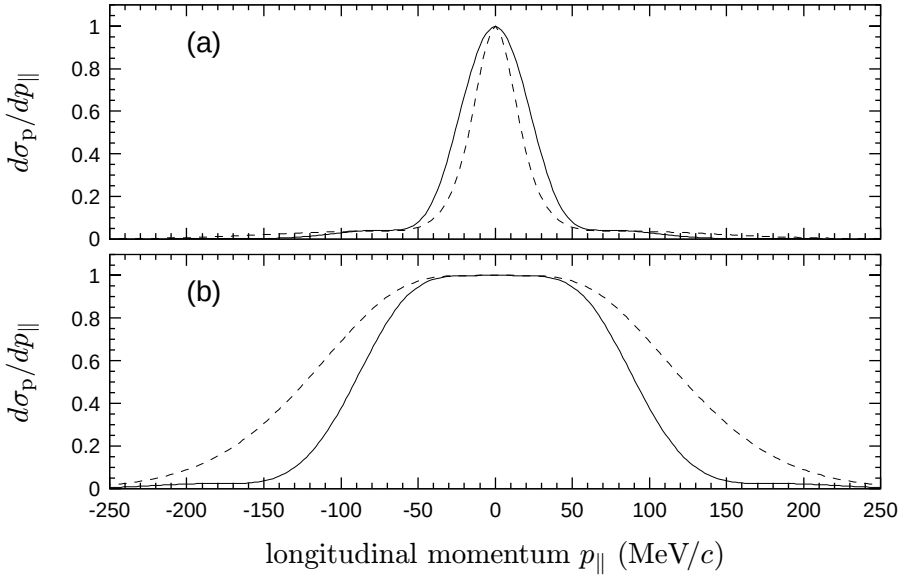

Figure 6.8: The two plots show calculated momentum distributions for the ^{18}C core after ^{19}C breakup in a carbon target in case of a removed $1s_{1/2}$ neutron (a) and a $0d_{5/2}$ neutron (b). The dashed curves give the momentum distributions in the transparent limit, while the solid curves include final state interactions and core-shadowing [47, 46].

core shadowing narrows primarily the distributions from states with larger angular momenta. In total, the reaction mechanism slightly broadens the momentum distributions for s-states, and significantly narrows those for d-states.

The theoretical density distributions plotted in Fig. 6.9 picture ^{19}C not as a very pronounced halo nucleus. Viewed on a linear scale (upper panel), the neutron skin of the core nucleus, ^{18}C, is dominating even though only the $^{18}\mathrm{C}(0^+)\otimes 1s_{1/2}$ configuration is included in this plot. A look at this plot might give the idea that the core knockout, i.e. the removal of a neutron from the core nucleus, could play an important role in the one-neutron removal reactions. However, one has to consider that the halo nucleon is only loosely bound, and therefore it is very unprobable that the remaining ^{18}C after the core knockout of a neutron from ^{19}C survives.

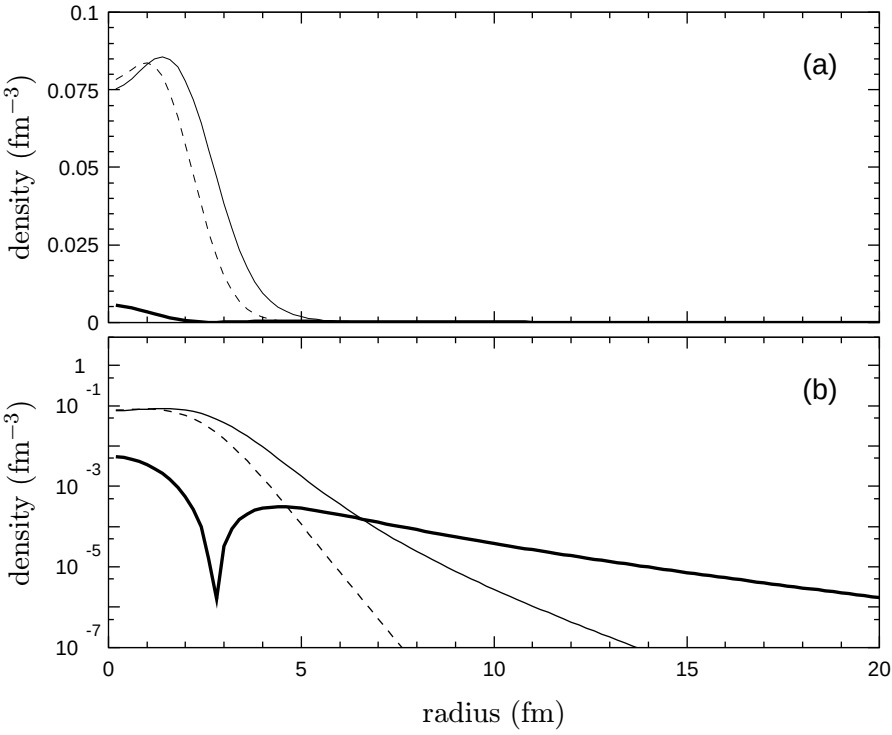

Figure 6.9: This plot shows the particle density distributions obtained from DCP-calculations by H. Lenske [46]. The solid curves represent neutron densities, while the proton densities are shown by dashed lines. The density distributions for the ^{18}C core are plotted with thin lines, the thick line gives the density of a valence neutron in the $1s_{1/2}$ state only. The integrals of the curves are normalized to the corresponding particle number. The bottom panel (b) shows the same curves as plotted in (a), only on a logarithmic scale.

6.4.3 Comparison of the ^{19}C theories

The two theoretical approaches presented here come to different conclusions concerning the ground state configuration. The problem is the proximity of the *s*- and *d*-states in ^{19}C, which makes it difficult to discriminate a certain ground state configuration based on the measured momentum distribution alone.

But both theories lead to the common conclusion that the first excited 2^+ state of the ^{18}C core plays an important role in the nuclear configuration of ^{19}C. In consequence, the spatial extension of the valence neutron would be less than indicated by the ground state separation energy alone and the one-neutron halo of ^{19}C would be less pronounced as in the case of ^{11}Be – a statement that is supported by the measured momentum widths of the longitudinal momentum distributions.

Chapter 7

Results on ^{8}B

The nucleus ^{8}B initiated a large interest as the first one-proton halo nucleus when a very large quadrupole moment was disclosed in NMR measurements [52]. However, this case was discussed with much controversy, as some following investigations could not support the picture of a proton halo [55, 60].

The first measurement of the longitudinal momentum distribution of ^{7}Be core-fragments from the breakup of ^{8}B was undertaken at the FRS in 1994 [70]. The observation of a narrow distribution was another hint at a halo structure.

Here, I present the results of an refined measurement of longitudinal momentum distributions from the breakup of ^{8}B [11, 73]. The results discussed in this work were obtained using the same technique as in the 1994 measurement, but with an improved detection system, an extended experimental setup, and a better stability of the magnetic fields of the spectrometer. We also were able to improve considerably in terms of statistics and momentum range that was covered.

7.1 ^{8}B – some details

The dripline nucleus ^{8}B has an exposed position on the chart of nuclei since both its neighbors, ^{7}B and ^{9}B, are proton-unbound. The valence proton of ^{8}B is bound by only 137 keV, which is a remarkably low value and even smaller than the separation energies for well established neutron halos such as ^{11}Be and ^{11}Li. This is the reason why ^{8}B is regarded as a good proton-halo candidate.

The constraints are the Coulomb barrier that hinders the valence proton to tunnel into the exterior region, and the fact that the last proton in ^{8}B is bound in a $p_{3/2}$-state, so an additional angular momentum barrier is added.

The interaction cross section for ^{8}B has already been measured at a projectile energy of 790 MeV/u by I. Tanihata *et al.* in 1988 [79], but no unusual increase compared to the other boron isotopes was observed. A later measurement of interaction cross sections at much lower energies

between 20 and 60 MeV/u, however, strongly indicated a halo structure [81].

The first momentum distributions of the breakup fragments from ^{8}B were measured at 1471 MeV/u [70] and 41 MeV/u [39]. In principle, both measurements observed a narrow momentum distribution, whereas the interpretations concerning the halo structure of ^{8}B came to contradicting conclusions. While in the measurement at high energy no dependence of the momentum width on the target material was seen, the low energy data showed such a dependence, indicating that at low energies the momentum distribution is significantly influenced by the breakup mechanism.

7.2 The experiment

For the production of the radioactive beam of ^{8}B nuclei, a ^{12}C primary beam from the heavy-ion synchrotron SIS with 1.5 GeV/u was directed onto a 8.0 g/cm^2 beryllium target. The experimental setup for this measurement is identical to the setup used for the measurements of carbon isotopes described in Chapter 6 and depicted in Figs. 3.1, 4.4, and 4.5.

The separated ^{8}B nuclei had a mean energy of 1440 MeV/u at the breakup target with about 4% energy spread (full width). We employed breakup targets of 4.41 g/cm^2 carbon and 8.00 g/cm^2 lead, which were mounted at the dispersive mid-plane of the FRS.

7.2.1 Longitudinal momentum distributions for ^{8}B

For the measurement of the longitudinal momentum distributions of the ^{7}Be reaction products of the proton removal from ^{8}B, two different ion optical settings were used.

With the first ion-optical setting, we intended to determine the full shape of the momentum distribution by including the high-momentum tail. This was done by increasing the magnetic rigidity of the second spectrometer stage in two steps of 1% each. How the three resulting distributions were combined is explained in Sec. 5.2.2. This method was applied only to the measurement of the breakup in a carbon target.

The final distribution from the breakup of ^{8}B in carbon is shown in Fig. 7.1, panel (a). With a double-Gaussian curve I could satisfactorily reproduce the shape of this distribution in a fit, from which a FWHM of 96 ± 6 MeV/c was deduced. It should be noted that two centered Gaussian components were only used in order to achieve a good fit to the data, and not to differentiate between different components of the momentum distribution. The system resolution, including the contribution of location straggling in the breakup target, has a FWHM of 20.2 MeV/c. The correction for the resolution reduces the width to a value of 94 ± 6 MeV/c.

With the second ion-optical setting, we focused on the central region and combined data sets from two settings of the magnetic rigidity. The combination of the two data sets is described in Sec. 5.2.2. This method was

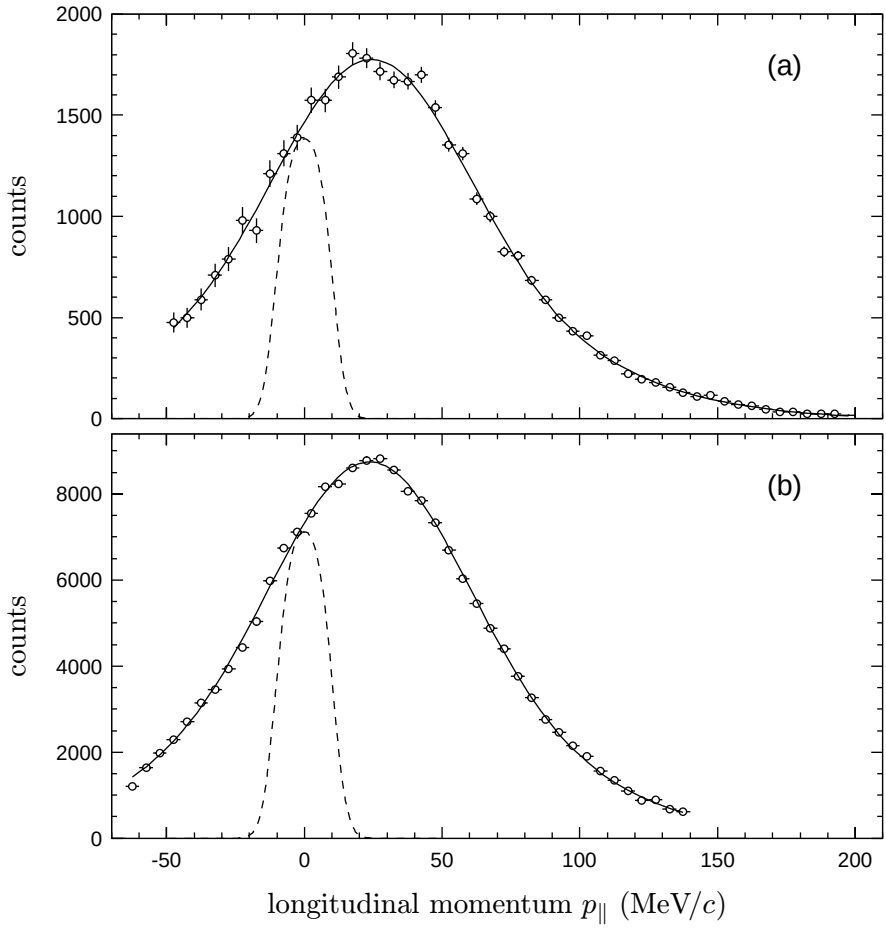

Figure 7.1: Longitudinal momentum distribution of ^{7}Be fragments from the breakup of ^{8}B on a carbon target. The distributions are transformed into the projectile frame. The distribution in panel (a) is a combination of three separate measurements in order to cover the high-momentum tail. The distribution in panel (b) focuses on the central region and provides better statistics. The width parameters of the two independent measurements of 94 ± 6 MeV/c and 95 ± 5 MeV/c (resolution corrected values) agree with each other. Double-Gaussian fits to the data are plotted as solid lines. The dashed curves represent the profile of the respective resolution function.

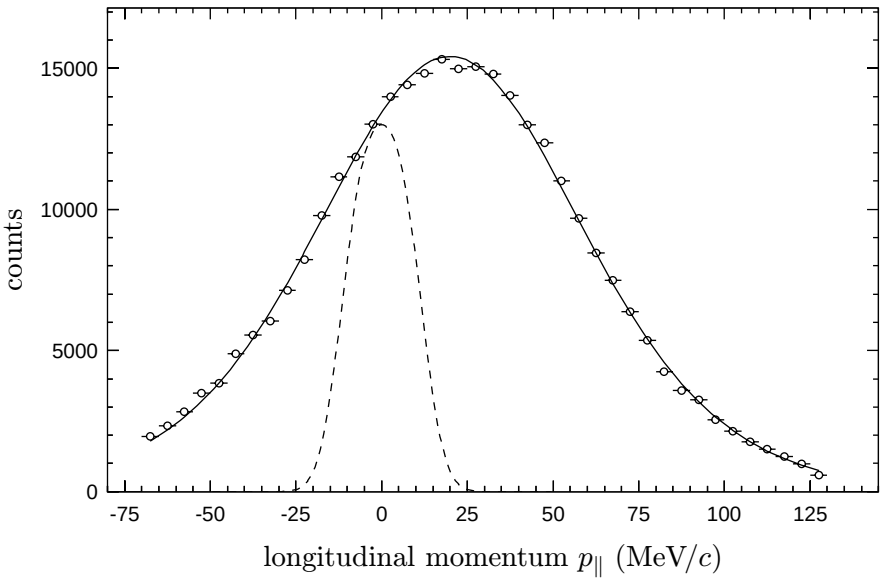

Figure 7.2: Measured longitudinal momentum distribution of ^{7}Be fragments from the breakup of ^{8}B on a lead target. The momentum is given in the projectile co-moving frame. A double-Gaussian fit to the data is plotted as a solid line. The deduced FWHM of this distribution is 92 ± 5 MeV/c, leading to 88 ± 5 MeV/c after the correction for the system resolution. The dashed profile reflects the system resolution with a FWHM of 25.6 MeV/c.

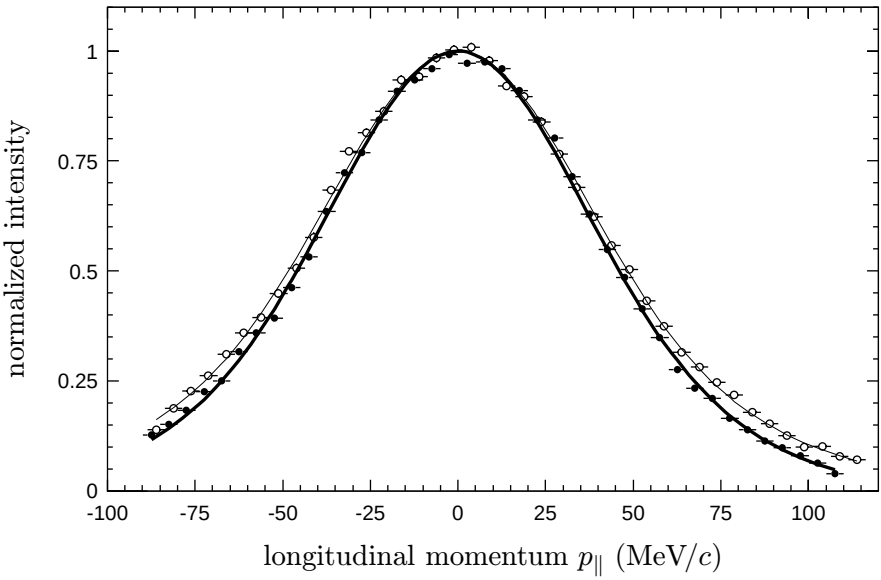

Figure 7.3: The measured longitudinal momentum distribution from the breakup of ^{8}B on a lead target (filled symbols, thick line) are only slightly narrower than the distribution from the measurement with a carbon breakup target (open symbols, thin line). These distribution were normalized at their maxima.

applied to the measurement of momentum distributions from the breakup on carbon and lead targets.

The resulting longitudinal momentum distribution from the breakup on a carbon target, transformed into the projectile co-moving frame, is plotted in Fig. 7.1, panel (b). From a double-Gaussian fit to this distribution, a FWHM of 97 ± 5 MeV/c was obtained, which gives a resolution-corrected value of 95 ± 5 MeV/c. This value is in agreement with the distribution in panel (a).

The one proton removal from ^{8}B was also studied with a lead breakup target. The obtained longitudinal momentum distribution is presented in Figs. 7.2 & 7.3. This distribution is only slightly narrower than the distribution obtained for a breakup on a carbon target. This supports the findings in the earlier measurement of the ^{8}B breakup at relativistic energies, where no difference in momentum widths for light and heavy breakup targets was observed [70]. The value for the FWHM of the momentum distribution that results from this measurement is 92 ± 5 MeV/c, with the resolution of 25.6 MeV/c (FWHM) taken into account, this gives a value of 88 ± 5 MeV/c.

Including the absolute cross section information

With the extended setup at the final focal plane of the FRS, we could also measure the charge changing cross sections of ^{8}B, which in this special case are identical to the one-proton removal cross sections because no other charge-changing reaction channel with $\Delta Z = 1$ exists. Please find the description of the cross section measurement in Appendix B.

The one-proton removal cross sections enable us to put the momentum distributions on an absolute scale, so that not only shape parameters but also the differential cross section $d\sigma_{\mathrm{p}}/dp_{\parallel}$ can be compared with theoretical calculations.

For the one-proton removal cross section of ^{8}B on a carbon target, a value of $\sigma_{\mathrm{p}} = 98 \pm 6$ mb [22] was obtained from the measurement of charge changing cross sections that is described in Appendix B.1.

The longitudinal momentum distributions from the ^{8}B breakup on a carbon target, scaled to the one-proton removal cross section, are shown in Figs. 7.4.

7.2.2 Comparison with other measurements

For the ^{8}B breakup, a number of experimental data, including measurements of longitudinal momentum distributions, exist.

The GSI measurement

The longitudinal momentum distribution of ^{7}Be fragments from the ^{8}B breakup was already measured at the FRS in 1994 [70]. In the recent experiment, we have successfully attempted a refined measurement with im-

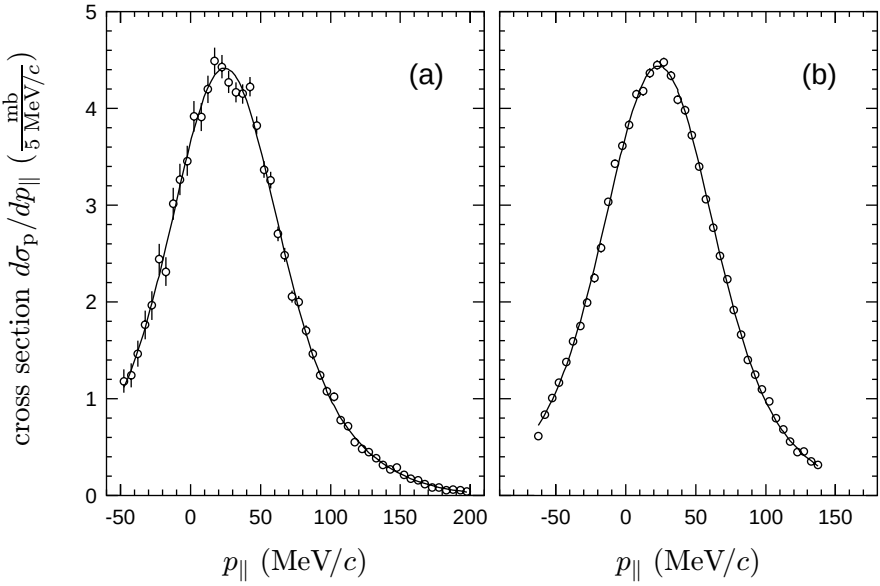

Figure 7.4: This plot shows the scaled momentum distributions for the ^{8}B breakup reaction on a carbon target that were obtained in the two measurements described in Sec. 7.2.1. The error bars on the data points only reflect statistical errors of the momentum measurement, but do not include the uncertainties of the experimental cross section.

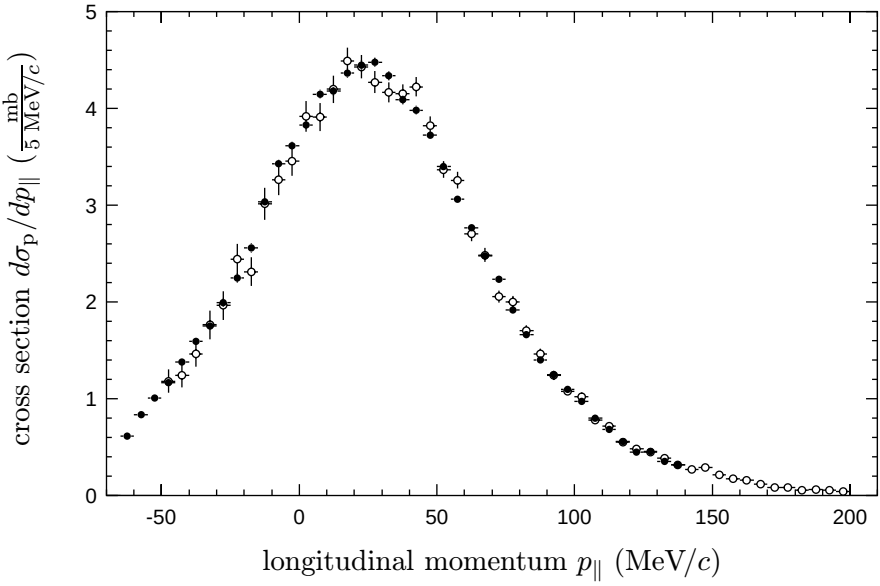

Figure 7.5: The direct comparison of the longitudinal momentum distributions $d\sigma_p/dp_\parallel$ obtained in two independent measurements (open symbols and filled symbols) shows the good agreement between the two data sets.

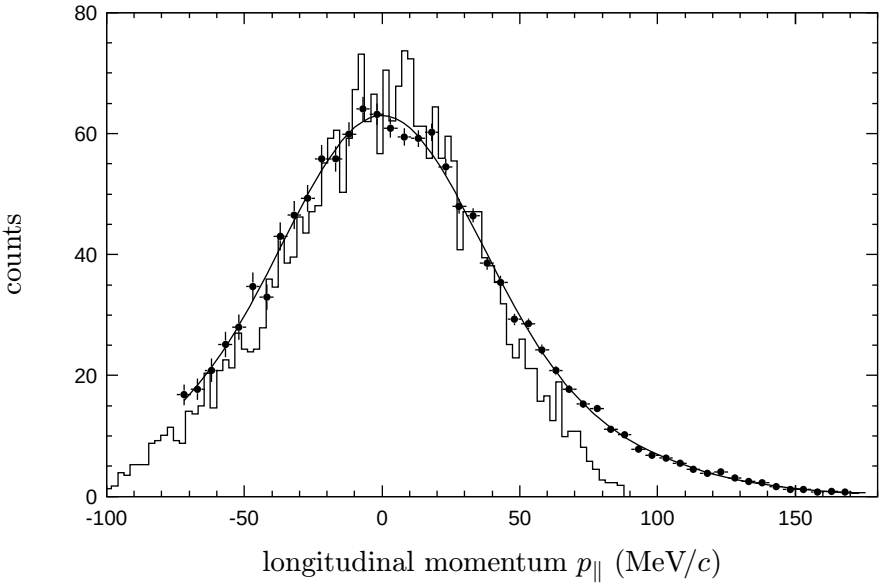

Figure 7.6: Direct comparison of the momentum distribution measured at the FRS in 1995 (from Ref. 70, histogram) with the recent result (filled circles, with a double-Gaussian fit). The two distributions are centered in the projectile co-moving frame and the data set from the new measurement is scaled to match the old distribution. The ordinate values refer to the histogram.

proved statistics and an extended coverage of the high momentum tail. The direct comparison of the two momentum distributions that were obtained in the different experiments, as shown in Fig. 7.6, shows an agreement in the central momentum region, while the new distribution reaches out to 175 MeV/c from the center.

The width of 94 ± 5 MeV/c, which was obtained from the new measurement, is slightly larger than the value of 81 ± 6 MeV/c that was published in Ref. 70. The direct comparison of the distributions, however, shows that the smaller value is caused by the restricted momentum coverage of the older data. It should also be noted that from the old data no conclusive statement about the shape of the distribution in the momentum tails could be drawn, while the extended distribution shows clearly that neither a pure Gaussian nor a Lorentzian curve can reproduce the data. The one-proton removal cross section of ^{8}B for a carbon target of 94 ± 4 mb that is stated in Ref. 70 agrees very well with the value of 98 ± 6 mb that was extracted from the new data.

A comparison with the momentum distribution obtained for fragments from the one-proton removal reaction of the stable nucleus ^{10}B is shown in Fig. 7.7. The ^{10}B breakup was performed at 1450 MeV/c in a carbon target. The distribution exhibits a Gaussian shape with a FWHM of 165 ± 9 MeV/c, about a factor two larger than for the loosely bound ^{8}B.

A look at the momentum distributions for ^{8}B and ^{10}B, scaled to their

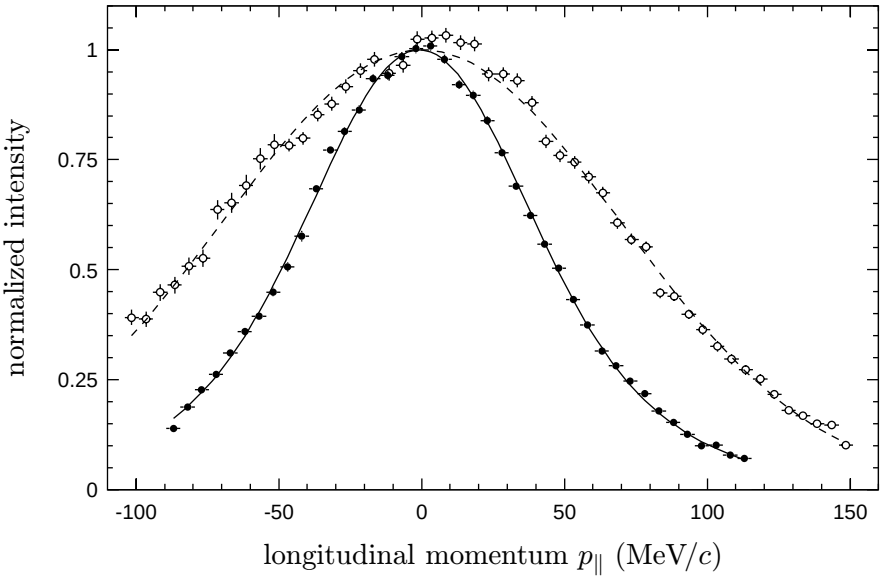

Figure 7.7: This figure shows the obtained momentum distributions for the core fragments from a one-proton removal reaction on ^{8}B (filled symbols) and ^{10}B (open symbols), with a carbon breakup target in both cases. The dashed line is a Gaussian fit to the ^{10}B data with a FWHM of 165 ± 8 MeV/c. The two distributions are normalized at the maximum.

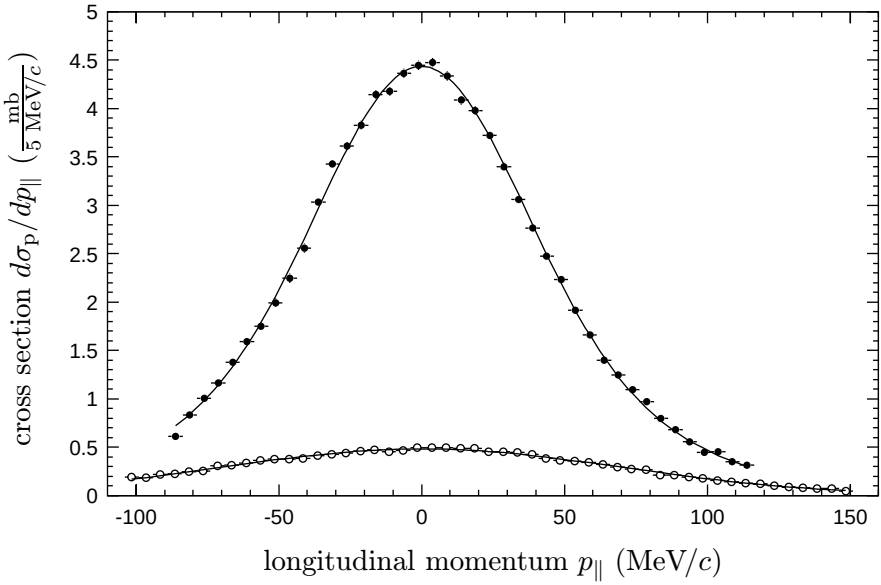

Figure 7.8: The longitudinal momentum distributions of core fragments from the ^{8}B (filled symbols) and ^{10}B (open symbols) one-proton removal reaction on an absolute scale of one-proton removal cross section. Please note that the errors on the cross sections are not shown in this plot.

Table 7.1: Obtained widths for the longitudinal momentum distributions of breakup fragments from one-proton removal reactions.

Projectile	Energy (MeV/u)	Target	FWHM (MeV/c)	Ref.
^{8}B	1471	C, Al, Pb	81 ± 6	[70]
^{8}B	41	Be Au	81 ± 4 67 ± 3	[39]
^{8}B	38	Si	93 ± 7	[57]
^{8}B	1440	C	95 ± 5[a]	this work
^{8}B	1440	Pb	88 ± 5[a]	this work
^{10}B	1450	C	165 ± 8[b]	this work

[a] double Gaussian
[b] Gaussian

respective one-proton removal cross sections of 98 ± 6 mb and 17 ± 3 mb [22], as is shown in Fig. 7.8, is very interesting. With this picture it becomes evident that the special nuclear structure manifests itself not only in a narrow momentum distribution, but also in a largely enhanced one-proton removal cross section as compared to a tightly bound nucleus.

Results from other experiments

The observation of a narrow momentum distribution of the ^{7}Be fragments from the ^{8}B breakup reaction at relativistic energies at GSI [70] was followed by investigations of this reaction at lower energies.

The results that were obtained are summarized in Tab.7.1. It should be noted that a single parameter, i.e. the value of FWHM, in general can not completely characterize a distribution. The information about the shape is required as well, only then the distribution is reproducible. It is therefore difficult to compare two distributions by means of their FWHM alone, in fact it can be quite misleading.

A comparison of the various momentum widths from breakup reactions at different projectile energies shows that the values obtained with light targets agree reasonably well over a large range of energies, while for heavy targets the width is strongly reduced at low projectile energies. This has been attributed to the reaction mechanism, which narrows the momentum distribution significantly. The authors of Ref. 39 argue that no extended wave function is needed to explain the narrow momentum distributions, as this can be reproduced by just taking the core shadowing into account. The core shadowing has a larger impact on p-states than on s-states and is therefore important in the case of ^{8}B.

7.3 ^{8}B and the theories

Because the nucleus ^{8}B was discussed with much controversy, and because of its role in the solar neutrino problem, a large number of publications about theoretical investigations of this nucleus exists. In the short overview given here, I want to restrict myself to two theoretical calculations that were done within our collaboration. Although completely different in their approaches, both lead to the common conclusion that there is an extended proton wave function in ^{8}B.

7.3.1 The mean-field QRPA approach

Similar to the calculations outlined in Sec. 6.4.2, H. Lenske also applied the mean-field QRPA theory [48] to compute the momentum distribution of the core fragments from the ^{8}B breakup.

In the QRPA-picture, the nucleus ^{8}B is described by proton-particle neutron-hole excitations based on ^{8}Be. This leads to a ^{8}B(2^+) ground state. With a $1p_{3/2}$ neutron-hole configuration in ^{8}Be, a correlated $3/2^-$ proton wave function coupled to the ^{7}Be ground state is obtained. The calculations include also small admixtures (about 8%) from $1/2^-$ proton components. The reaction dynamics is described in an eikonal approach, including interferences from nucleon–nucleon scattering.

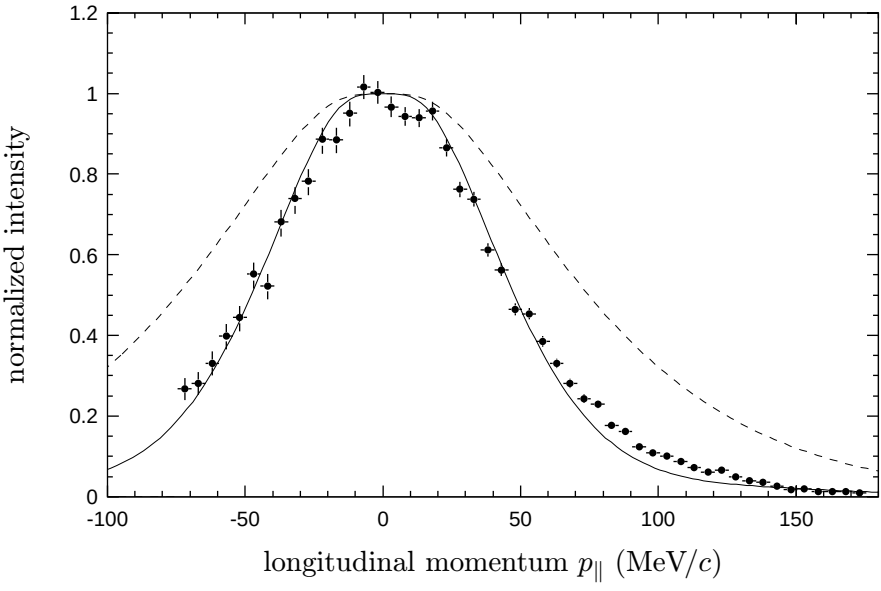

Figure 7.9: In this plot, the measured longitudinal momentum distribution of ^{7}Be fragments from the breakup of ^{8}B on a carbon target is compared to a QRPA calculation by H. Lenske. The dashed curve represents the distribution obtained in the transparent limit, while the solid distribution was calculated taking final state interactions and the reaction dynamics into account [46]. The theoretical curves are folded with the system resolution.

The longitudinal momentum distribution from the ^{8}B breakup on a carbon target is reproduced very nicely, as shown in Fig. 7.9.

7.3.2 The three-body cluster

M. H. Smedberg *et al.* describe ^{8}B using a wave function calculated in an extended three-body model [73, 32].[2] In this approach, the ^{8}B nucleus is viewed as a three-body system consisting of an α particle, a ^{3}He nucleus and a proton. To account for the loosely bound proton, the binary ^{7}Be–p channel is implicitly included. Effects of strong deformation and dynamical polarization of the ^{7}Be core as well as the core excitations are treated simultaneously.

The dominating configurations are a $p_{3/2}$ or a $p_{1/2}$ proton coupled to the ^{7}Be ground state ($J^\pi = 3/2^-$), and a proton in a $p_{3/2}$-orbital bound to the first excited state of ^{7}Be ($J^\pi = 1/2^-$).

The reaction mechanism is found to have a major impact on the longitudinal momentum distribution also in the case of relativistic projectile energies and light breakup targets. Taking core shadowing into account in

[2] The value for the FWHM of the ^{7}Be longitudinal momentum distribution stated in Ref. [73] differs slightly from the value stated here because the data I present here stems from a later and further refined analysis of the experiment.

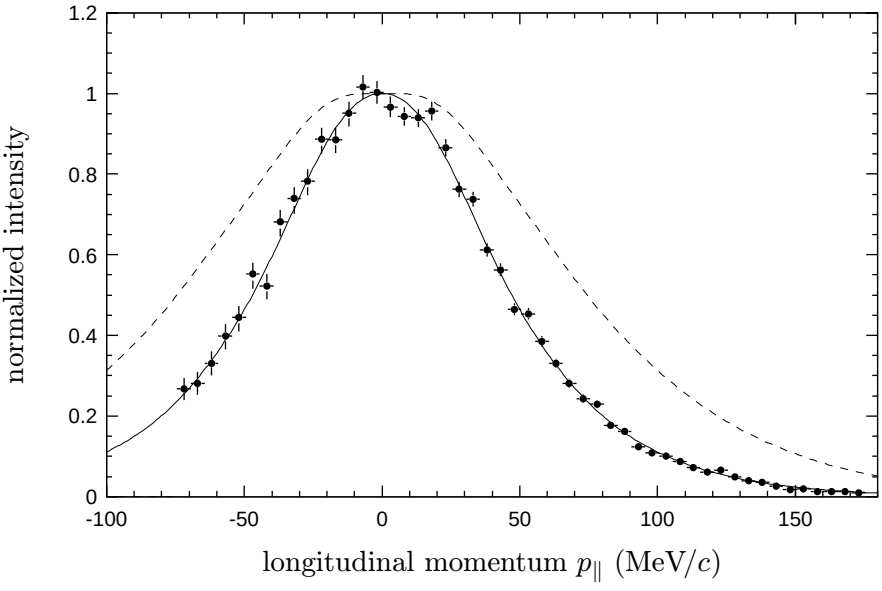

Figure 7.10: Calculation using the three-body cluster model for the ^{7}Be longitudinal momentum distribution after the breakup of ^{8}B in a carbon target [73]. The solid curve corresponds to the calculation that takes core-shadowing into accout. This distribution is folded with the system resolution. The dashed curve gives the calculated distribution in the transparent limit of the Serber model. The measured momentum distribution is plotted with filled circles.

the opaque limit of the Serber model, i.e. treating the target nucleus as a black disk, the calculated momentum distributions are able to reproduce the measured distribution.

The sum of the longitudinal momentum distributions from the three dominating configurations, folded with the system resolution and scaled to the measured distribution, is plotted in Fig. 7.10. The agreement between measurement and theory is striking.

However, since this calculation does not take Coulomb dissociation into account, the calculated cross section misses about 25% of the measured value of 98 ± 6 mb [73].

Comparison of the two theories

In general, both theories are able to describe the measured momentum distribution from the breakup on a carbon target rather well. The small differences in shape completely vanish if one compares the distributions obtained for the transparent limit. Such a comparison is shown in Fig. 7.11. Concerning the momentum distribution, both theories are equivalent in their results and in their conclusion that ^{8}B has a spatially extended proton wave function. To give a final qualitative evaluation of the two, they have to show how well other experimental properties of ^{8}B can be reproduced.

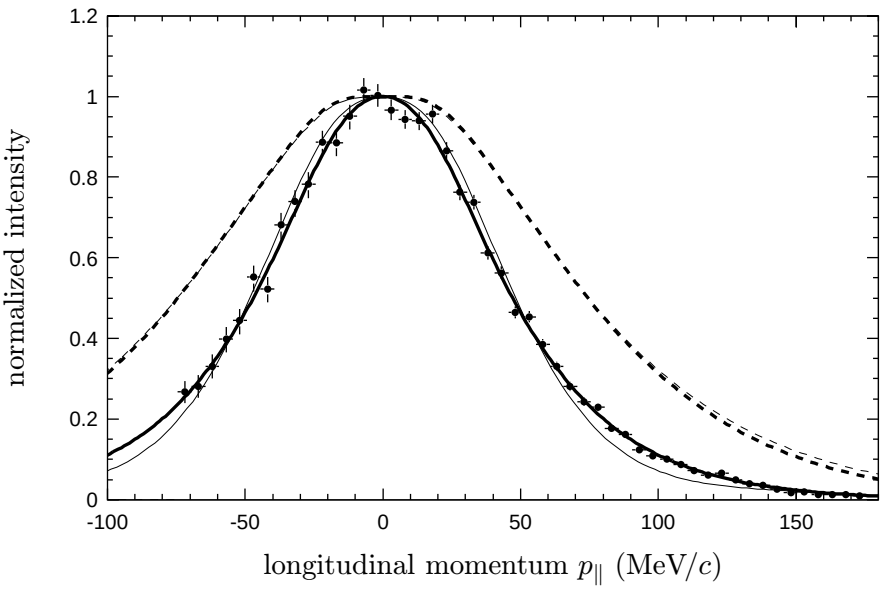

Figure 7.11: Comparison of QRPA (thin lines) and three-body cluster model (thick lines) momentum distributions for ^{8}B. The solid curves include the respective reaction dynamics calculation, while the dashed curves correspond to the transparent limit of the Serber model. In the transparent limit, the resulting distributions are almost indistinguishable.

Appendix A

Ion optics of the energy-loss mode

Here I will only give a brief introduction to ion optics, as much as is needed to describe the energy-loss mode. A thorough discourse on ion optics can be found in H. Wollnik's book, Ref. 83.

A.1 Some basic ideas

To uniquely describe the position and the movement of a particle at a certain time one needs six coordinates: three variables for the position in space, two angles to specify the direction of the motion, and one variable quantizing the motion, e.g., giving the momentum of the particle. An ion-optical system will work on all six of these coordinates and change them in a specific way. The most convenient way to describe such a system is by the use of *transfer matrices*. The vector in the ion-optical coordinates that describes the initial situation of an ion can be transformed by multiplication with the transfer matrix. The resulting vector then describes the ion-optical coordinates of the ion after passing through the system. For a linear transformation, this can be accomplished with the six by six matrix M:

$$\begin{pmatrix} x \\ a \\ y \\ b \\ s \\ \delta_p \end{pmatrix} = \mathsf{M} \begin{pmatrix} x_0 \\ a_0 \\ y_0 \\ b_0 \\ s_0 \\ \delta_{p0} \end{pmatrix}. \tag{A.1}$$

In the ion-optical coordinate system, positions and momenta of an ion are described relative to a reference particle that moves along a reference trajectory with a reference momentum. The position of the ion is defined by the two transverse coordinates x and y which lie in a plane perpendicular to the direction of the reference momentum. The direction of the ion's

momentum relative to that of the reference particle is given by the values a and b as defined in Eq. A.2, these are the tangents of the angles between the reference momentum and the ion's momentum in x- and y-direction, respectively. The magnitude of the momentum is determined by the fractional momentum deviation δ_p, defined in Eq. A.3. The sixth variable is the distance along the reference path, s. Please note that in this case the time is the independent variable.

$$a = \frac{dx}{ds}\,, \qquad b = \frac{dy}{ds}\,, \tag{A.2}$$

$$\delta_p = \frac{p - p_0}{p_0}\,. \tag{A.3}$$

The variable p denotes the component of the particle momentum in the direction of the reference path. This is important to understand later which component of the particle momentum is measured.

A.2 The transfer matrix in first order

For a magnetic system that is symmetric with respect to the horizontal midplane, the x- and y-planes do not mix, therefore the upper left four-by-four submatrix of the matrix M decomposes into two two-by-two matrices. The matrix for such a system then can be written as

$$\mathsf{M} = \begin{pmatrix} m_{11} & m_{12} & 0 & 0 & 0 & m_{16} \\ m_{21} & m_{22} & 0 & 0 & 0 & m_{26} \\ 0 & 0 & m_{33} & m_{34} & 0 & 0 \\ 0 & 0 & m_{43} & m_{44} & 0 & 0 \\ m_{51} & m_{52} & 0 & 0 & 1 & m_{56} \\ 0 & 0 & 0 & 0 & 0 & 1 \end{pmatrix}.$$

The matrix elements m_{ij} represent the solutions for the equation of motion of the charged particle in first order. If higher orders should be included, the dimension of the matrix has to be increased. The coefficients of first order are

$$m_{11} = (x|x) = \frac{\partial x}{\partial x_0}\,, \qquad m_{12} = (x|a) = \frac{\partial x}{\partial a_0}\,, \qquad m_{16} = (x|\delta) = \frac{\partial x}{\partial \delta_{p0}}\,,$$

$$m_{21} = (a|x) = \frac{\partial a}{\partial x_0}\,, \qquad m_{22} = (a|a) = \frac{\partial a}{\partial a_0}\,, \qquad m_{26} = (a|\delta) = \frac{\partial a}{\partial \delta_{p0}}\,,$$

$$m_{33} = (y|y) = \frac{\partial y}{\partial y_0}\,, \qquad m_{34} = (y|b) = \frac{\partial y}{\partial b_0}\,,$$

$$m_{43} = (b|y) = \frac{\partial b}{\partial y_0}\,, \qquad m_{44} = (b|b) = \frac{\partial b}{\partial b_0}\,,$$

$$m_{51} = (s|x) = \frac{\partial s}{\partial x_0}\,, \qquad m_{52} = (s|a) = \frac{\partial s}{\partial a_0}\,, \qquad m_{56} = (s|\delta) = \frac{\partial s}{\partial \delta_{p0}}\,.$$

Inserting these definitions, the matrix becomes

$$\mathsf{M} = \begin{pmatrix} (x|x) & (x|a) & 0 & 0 & 0 & (x|\delta) \\ (a|x) & (a|a) & 0 & 0 & 0 & (a|\delta) \\ 0 & 0 & (y|y) & (y|b) & 0 & 0 \\ 0 & 0 & (b|y) & (b|b) & 0 & 0 \\ (s|x) & (s|a) & 0 & 0 & 1 & (s|\delta) \\ 0 & 0 & 0 & 0 & 0 & 1 \end{pmatrix}.$$

These first order coefficients will be used in the following to calculate the particle position at the final focus of the magnetic spectrometer.

A.3 Momentum measurement using the energy-loss mode

For the description of the imaging of the FRS in the energy loss-mode, I use two transfer matrices. The FRS is divided into two stages as shown in Fig. A.1. The first two dipole magnets belong to the first stage that does the imaging from the entrance F0 to the dispersive mid-plane F2, which is described by the transfer matrix A. The second stage includes the last two dipole magnets and images F2 to the final focal plane F4 and is described by the matrix B.

$$\mathsf{A} \begin{pmatrix} x_{\mathrm{F0}} \\ a_{\mathrm{F0}} \\ y_{\mathrm{F0}} \\ b_{\mathrm{F0}} \\ s_{\mathrm{F0}} \\ \delta_{\mathrm{F0}} \end{pmatrix} = \begin{pmatrix} x_{\mathrm{F2}} \\ a_{\mathrm{F2}} \\ y_{\mathrm{F2}} \\ b_{\mathrm{F2}} \\ s_{\mathrm{F2}} \\ \delta_{\mathrm{F2}} \end{pmatrix}, \qquad \mathsf{B} \begin{pmatrix} x_{\mathrm{F2}} \\ a_{\mathrm{F2}} \\ y_{\mathrm{F2}} \\ b_{\mathrm{F2}} \\ s_{\mathrm{F2}} \\ \delta_{\mathrm{F2}} \end{pmatrix} = \begin{pmatrix} x_{\mathrm{F4}} \\ a_{\mathrm{F4}} \\ y_{\mathrm{F4}} \\ b_{\mathrm{F4}} \\ s_{\mathrm{F4}} \\ \delta_{\mathrm{F4}} \end{pmatrix}. \tag{A.4}$$

To be able to include cases where the second stage of the spectrometer is set to a different magnetic rigidity, e.g., to accept a breakup fragment, the two transfer matrices A and B have different reference momenta p_{A} and p_{B}.

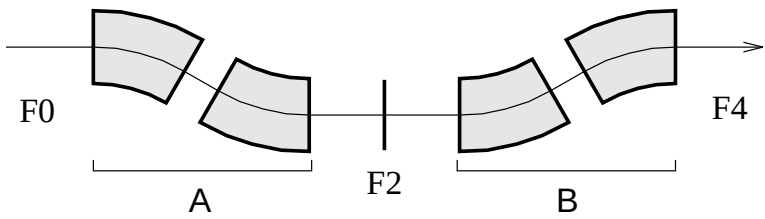

Figure A.1: This schematic view of the two-stage spectrometer FRS corresponds directly to the Eqs. A.4.

A.4 Determination of the x-position

We are interested in the x-positions of our particle. From the matrix multiplication we deduce the x-positions at F2 and F4 in first order:

$$x_{\mathrm{F2}} = (x|x)_{\mathsf{A}} x_{\mathrm{F0}} + (x|a)_{\mathsf{A}} a_{\mathrm{F0}} + (x|\delta)_{\mathsf{A}} \delta_{\mathrm{F0}} \,, \tag{A.5}$$

$$x_{\mathrm{F4}} = (x|x)_{\mathsf{B}} x_{\mathrm{F2}} + (x|a)_{\mathsf{B}} a_{\mathrm{F2}} + (x|\delta)_{\mathsf{B}} \delta_{\mathrm{F2}} \,. \tag{A.6}$$

For a system with point-to-point imaging, the position of the particle at the image plane is independent of the initial angle, therefore the matrix elements $(x|a)_{\mathsf{A}}$ and $(x|a)_{\mathsf{B}}$ are zero:

$$x_{\mathrm{F2}} = (x|x)_{\mathsf{A}} x_{\mathrm{F0}} + (x|\delta)_{\mathsf{A}} \delta_{\mathrm{F0}} \,, \tag{A.7}$$

$$x_{\mathrm{F4}} = (x|x)_{\mathsf{B}} x_{\mathrm{F2}} + (x|\delta)_{\mathsf{B}} \delta_{\mathrm{F2}} \,. \tag{A.8}$$

Replacing x_{F2} in Eq. A.8 yields

$$x_{\mathrm{F4}} = (x|x)_{\mathsf{B}}(x|x)_{\mathsf{A}} x_{\mathrm{F0}} + (x|x)_{\mathsf{B}}(x|\delta)_{\mathsf{A}} \delta_{\mathrm{F0}} + (x|\delta)_{\mathsf{B}} \delta_{\mathrm{F2}} \tag{A.9}$$

$$= (x|x)_{\mathsf{B}}(x|x)_{\mathsf{A}} x_{\mathrm{F0}} + (x|x)_{\mathsf{B}}(x|\delta)_{\mathsf{A}} \frac{p_{\mathrm{F0}} - p_{\mathsf{A}}}{p_{\mathsf{A}}} + (x|\delta)_{\mathsf{B}} \frac{p_{\mathrm{F2}} - p_{\mathsf{B}}}{p_{\mathsf{B}}} \,. \tag{A.10}$$

Now we add the condition for the energy loss mode, namely the dispersion matching of the two stages. This requires that the deviation in x at F4 due to the first dispersive stage is compensated by the dispersion of the second stage. For this, the equation

$$(x|x)_{\mathsf{B}}(x|\delta)_{\mathsf{A}} = -(x|\delta)_{\mathsf{B}} \tag{A.11}$$

must be fulfilled. A look at Eq. A.9 shows us that this condition makes our complete system achromatic if the fractional momentum deviation does not change at the mid-plane F2 ($\delta_{\mathrm{F0}} = \delta_{\mathrm{F2}}$). In this case the x-position at F4 is independent of the particle momentum.

However, if there is a breakup target inserted at F2, the momentum of the particle changes. The momentum behind the target, p_{F2}, is the momentum of the particle before traversing the target, p_{F0}, plus a change in momentum due to the energy loss and nuclear reactions in the target. This momentum change is the quantity that we measure with the energy loss mode. The momentum change is caused by three contributions: the atomic energy loss, the change in mass due to the nucleon removal, and the momentum imparted by the removed nucleon. The momentum change caused by the loss of mass can be excluded by regarding the velocity change in the breakup reaction, as shown in Fig. 2.3.

The momentum of a particle moving at relativistic velocity is

$$\begin{aligned} p &= mv \\ &= \gamma m_0 v \,. \end{aligned}$$

To denote the different rest masses before and after the reaction, I use the indices A and B. The velocity in front of the breakup target is v_{F0}, and the velocity behind v_{F2}, so we define $\Delta v = v_{F2} - v_{F0}$. With this, we obtain for the momentum after breakup:

$$\begin{aligned} p_{F2} &= \gamma_{F2} m_B v_{F2} \\ &= \gamma_{F2} m_B (v_{F0} + \Delta v) \,, \end{aligned} \tag{A.12}$$

with γ_{F2} corresponding to v_{F2}. The velocity change Δv is given in the laboratory rest frame. The intrinsic momentum of the core fragment before the breakup, however, should be given in the halo-system's rest frame. This can be accomplished by transforming the total momentum p_{F2} after the breakup into the halo system's rest frame, which moves with the velocity v_{F0} relative to the laboratory. But before this transformation, we need to calculate the momentum p_{F2}.

Inserting the relations A.11 into Eq. A.10, we obtain for the x-position at F4

$$\begin{aligned} x_{F4} &= (x|x)_B (x|x)_A x_{F0} - (x|\delta)_B \frac{p_{F0} - p_A}{p_A} + (x|\delta)_B \frac{p_{F2} - p_B}{p_B} \\ &= (x|x)_B (x|x)_A x_{F0} - (x|\delta)_B \left(\frac{p_{F0}}{p_A} - 1 \right) + (x|\delta)_B \left(\frac{p_{F2}}{p_B} - 1 \right) \end{aligned}$$

and finally

$$x_{F4} = (x|x)_B (x|x)_A x_{F0} - (x|\delta)_B \frac{p_{F0}}{p_A} + (x|\delta)_B \frac{p_{F2}}{p_B} \,. \tag{A.13}$$

From Eq. A.13, we see which variables determine the position at F4. The first term depends directly on the beam position at the entrance of the FRS. The beam should be centered at the entrance and the beam spot size should be as small as possible, in this case x_{F0} is negligible. The second term of Eq. A.13 depends on the momentum of the secondary beam p_{F0}, which can be dertermined by the measurement of x_{F2}. The third term, finally, contains the variable that we want to extract, the momentum p_{F2}.

A.5 Calculation of the longitudinal momentum

Simplifying Eq. A.13 by requiring that the position of the particle at the entrance of the spectrometer, x_{F0}, is negligible and solving for p_{F2} yields

$$p_{F2} = \frac{x_{F4}}{(x|\delta)_B} p_B + \frac{p_{F0}}{p_A} p_B \,. \tag{A.14}$$

Using $x_{F2} = (x|\delta)_A \delta_{F0}$ (compare with Eq. A.7) and the definition of δ_{F0} according to Eq. A.3, we replace p_{F0} with

$$p_{F0} = p_A \left(1 + \frac{x_{F2}}{(x|\delta)_A} \right) \tag{A.15}$$

Table A.1: This table lists ion optics variables and gives their definitions

x_{F2}	particle x-position at the mid-plane	x_{F4}	particle x-position at the final focus
v_{F0}	particle velocity in front of the breakup target	v_{F2}	particle velocity behind the breakup target
γ_{F0}	Lorentz factor of particle in front of the breakup target	γ_{F2}	Lorentz factor of particle behind the breakup target
p_{F0}	total longitudinal momentum in front of the breakup target	p_{F2}	total longitudinal momentum behind the breakup target
p_{A}	momentum of the reference particle in the first spectrometer stage A	p_{B}	momentum of the reference particle in the second spectrometer stage B
q_{A}	particle charge in front of the breakup target	q_{B}	particle charge behind the breakup target
m_{A}	particle rest mass before the breakup target	m_{B}	particle rest mass behind the breakup target
χ_{A}	reference magnetic rigidity of the first spectrometer stage A	χ_{B}	reference magnetic rigidity of the second spectrometer stage B
$(x\|\delta)_{A}$	dispersion of the first spectrometer stage A	$(x\|\delta)_{B}$	dispersion of the second spectrometer stage B

and obtain

$$p_{F2} = p_{B}\left(1 + \frac{x_{F2}}{(x|\delta)_{A}} + \frac{x_{F4}}{(x|\delta)_{B}}\right) \tag{A.16}$$

This equation was already used in Chapter 3 (Eq. 3.3).

The reference momentum p_{B} is defined by the setting of the magnetic rigidity of the second spectrometer stage, χ_{B}, and by the charge of the particle q_{B} behind the breakup target. The magnetic rigidity is defined as

$$\chi_{B} = \frac{p_{B}}{q_{B}}\,. \tag{A.17}$$

Substituting p_{B}, all variables in the formula are predefined or measured quantities and the momentum can be calculated directly:

$$p_{F2} = q_{B}\chi_{B}\left(1 + \frac{x_{F2}}{(x|\delta)_{A}} + \frac{x_{F4}}{(x|\delta)_{B}}\right) \tag{A.18}$$

As pointed out in section A.1, the momenta in these calculations are the components of the momentum vector in the direction of the reference path.

Equation A.18 gives the momentum p_{F2} in the laboratory frame. To deduce from this the intrinsic momentum of the core fragment before the breakup, p_{F2} has to be transformed into the rest frame of the halo system. This is described in Sec. 3.3.

Appendix B

Extracting cross sections

The setup at the final focal plane, as described in Sec. 4.3.2, was designed to measure charge-changing cross sections parallel to the measurement of momentum distributions. The charge-changing cross section is especially interesting in the case of ^{8}B, the one-proton halo nucleus, because here the charge-changing cross section equals the one-proton removal cross section since ^{6}Be is unbound and ^{7}Be is the only possible reaction product with $Z = 4$.

The measurement of the momentum distribution in energy-loss mode also provides the possibility to extract the one-nucleon removal cross sections, however with inferior accuracy due to the lack of a full particle identification at the breakup target and a necessary transmission correction.

The cross sections that I refer to in Secs. 6.2 and 7.2 were analyzed by D. Cortina-Gil, therefore I will only briefly describe the measurement of cross sections and their analysis. Cross sections, and especially the one-nucleon removal cross sections, can convey very important information on the nuclear structure of loosely bound systems, and should therefore not be excluded here.

B.1 Charge changing cross section

For the measurement of charge-changing cross sections, the detector setup at the final focus of the FRS, as depicted in Fig. 4.5, was used. The secondary beam of nuclei that were to be investigated was separated by the FRS and fully identified applying the method described in Sec. 4.4. This beam impinged on a reaction target placed behind the first MUSIC. The charge of the emerging particles was determined via the measurement of the energy deposited in the second MUSIC behind the reaction target.

From the data obtained in the measurements with this setup, two cross sections can be extracted. First, one can determine the number of emerging particles that have the same charge as the projectile. Compared to the number of incoming projectiles, this yields the *total charge-changing cross section*. Second, one can count all reaction products that have one proton

less than the projectile (irrespective of the neutron number), thus obtaining a *partial charge-changing cross section*.

It is evident that for nuclei at the proton drip line, the total charge-changing cross section is identical to the total interaction cross section, since any removal of a neutron will produce an unbound nucleus. In the same way, the partial charge-changing cross section with a reduction of the proton number by one is identical to the one-proton removal cross section.

The total interaction cross section σ_t is defined by

$$I = I_0\, e^{-\sigma_\mathrm{t} n d}\,, \tag{B.1}$$

where I is the number of transmitted non-reacting projectiles per time unit, I_0 the number of incoming projectiles per time unit, n the number of target atoms per volume unit, and d the target thickness.

The total charge-changing cross section σ_Z is defined analogously:

$$I_0 - I_Z = I_0\, e^{-\sigma_Z n d}\,. \tag{B.2}$$

Here, I_Z denotes the number of particles per time unit that undergo a charge-changing reaction, $I_0 - I_Z$ consequently corresponds to the number of particles that emerge with unchanged charge.

Counting the number of incoming projectiles and emerging particles with unchanged charge in a given time intervall, N_0 and N, respectively, the total charge-changing cross section can be calculated:

$$\frac{N}{N_0} = e^{-\sigma_Z n d}\,, \tag{B.3}$$

$$\sigma_Z = \frac{1}{nd}\,\ln\frac{N_0}{N}\,. \tag{B.4}$$

To extract partial charge changing cross sections σ_i, e.g. for reactions with $\Delta Z = 1$, the number of particles in a certain exit channel, N_i, needs to be counted. Using Eq. B.2, we obtain

$$\frac{N_0 - N_i}{N_0} = e^{-\sigma_i n d}$$

$$\sigma_i = \frac{1}{nd}\,\ln\frac{N_0}{N_0 - N_i}\,. \tag{B.5}$$

In the above equations only the target itself was considered. However, in the measurement nuclear reactions also occur in the detector materials and in the air between the two MUSICs. To correct for those reactions that do not occur in the target, measurements with the target removed were undertaken. Treating the surrounding materials as one compound target, we can rewrite Eq. B.2:

$$I_0 - I_Z = I_0\, e^{-\sigma_Z n d}\, e^{-\tilde{\sigma}_Z \tilde{n} \tilde{d}} \tag{B.6}$$

with $\tilde{\sigma}_Z$, $\tilde{n}$, and $\tilde{d}$ characterizing the materials in the beam *except* the target. The effect of these materials can be determined in a measurement

with removed target, from which the values $\widetilde{N}_0$ and $\widetilde{N}$ are taken. Inserting $\widetilde{N}/\widetilde{N}_0 = e^{-\tilde{\sigma}_Z \tilde{n} \tilde{d}}$ into Eq. B.6 gives

$$\frac{N}{N_0} = e^{-\sigma_Z n d} \frac{\widetilde{N}}{\widetilde{N}_0} \tag{B.7}$$

and we obtain

$$\sigma_Z = \frac{1}{nd} \ln \frac{N_0 \widetilde{N}}{N \widetilde{N}_0} \,. \tag{B.8}$$

In the same way the measurement of the partial charge-changing cross section σ_i can be corrected for reactions in surrounding materials. In this case, Eq. B.5 needs to be changed to

$$\sigma_i = \frac{1}{nd} \ln \frac{N_0(\widetilde{N}_0 - \widetilde{N}_i)}{(N_0 - N_i)\widetilde{N}_0} \,. \tag{B.9}$$

B.2 One-nucleon removal cross sections

The one-nucleon removal cross sections can be obtained from the measurements of the momentum distributions after one-nucleon removal in the breakup target at the dispersive mid-plane. The extraction of cross sections from this data is, however, hampered by two facts: the transmission between the dispersive mid-plane F2 and the final focal plane F4 needs to be taken into account, and there is no full particle identification in front of the breakup target, which prohibits the direct determination of the incoming projectile rate. Due to these reasons the one-nucleon removal cross sections can only be extracted with inferior accuracy.

The formulas to determine the one-nucleon removal cross sections are identical to those presented in Sec. B.1. The transmission between F2 and F4 was calculated in a MOCADI simulation. Using settings where the projectile nucleus was transmitted to F4 and identified there, particle scalers at F0 or F2 can be calibrated, taking transmission losses into account, to yield the count rate of the selected projectile.

At the time of writing this thesis, the analysis of cross sections is not yet completed. Therefore a complete list of all cross section values can not be given.

Bibliography

[1] S. P. Ahlen. Theoretical and experimental aspects of the energy loss of relativistic heavily ionizing particles. *Reviews of Modern Physics*, 52:121, 1980.

[2] D. Aleksandrov, T. Aumann, L. Axelsson, T. Baumann, M. J. G. Borge, L. V. Chulkov, J. Cub, W. Dostal, B. Eberlein, Th. W. Elze, H. Emling, H. Geissel, V. Z. Goldberg, M. Golovkov, A. Grünschloß, M. Hellström, J. Holeczek, R. Holzmann, B. Jonson, A. A. Korsheninnikov, J. V. Kratz, G. Kraus, R. Kulessa, Y. Leifels, A. Leistenschneider, T. Leth, I. Mukha, G. Münzenberg, F. Nickel, T. Nilsson, G. Nyman, B. Petersen, M. Pfützner, A. Richter, K. Riisager, C. Scheidenberger, G. Schrieder, W. Schwab, H. Simon, M. H. Smedberg, M. Steiner, J. Stroth, A. Surowiec, T. Suzuki, O. Tengblad, and M. V. Zhukov. Invariant mass spectrum and α–n correlation function studied in the fragmentation of ^{6}He on a carbon target. *Nucl. Phys. A*, 633:234–246, 1998.

[3] R. Anne, S. E. Arnell, R. Bimbot, S. Dogny, H. Emling, H. Esbensen, D. Guillemaud-Mueller, P. G. Hansen, P. Hornshøj, F. Humbert, B. Jonson, M. Keim, M. Lewitowicz, P. Møller, A. C. Mueller, R. Neugart, T. Nilsson, G. Nyman, F. Pougheon, K. Riisager, M.-G. Saint-Laurent, G. Schrieder, O. Sorlin, O. Tengblad, K. W. Rolander, and D. Wolski. Dissociation reactions of the ^{11}Be one-neutron halo. The interplay between structure and reaction mechanism. *Phys. Lett. B*, 304:55, 1993.

[4] R. Anne, S. E. Arnell, R. Bimbot, H. Emling, D. Guillemaud-Mueller, P. G. Hansen, L. Johannsen, B. Jonson, M. Lewitowicz, S. Mattsson, A. C. Mueller, R. Neugart, G. Nyman, F. Pougheon, A. Richter, K. Riisager, M. G. Saint-Laurent, G. Schrieder, O. Sorlin, and K. Wilhelmsen. Observation of forward neutrons from the break-up of the ^{11}Li neutron halo. *Phys. Lett. B*, 250(1,2):19–23, 1990.

[5] R. Anne, R. Bimbot, S. Dogny, H. Emling, D. Guillemaud-Mueller, P. G. Hansen, P. Hornshøj, F. Humbert, B. Jonson, M. Keim, M. Lewitowicz, P. Møller, A. C. Mueller, R. Neugart, T. Nilsson, G. Nyman, F. Pougheon, K. Riisager, M.-G. Saint-Laurent, G. Schrieder, O. Sorlin, O. Tengblad, and K. Wilhelmsen-Rolander. Exclusive

and restricted-inclusive reactions involving the ^{11}Be one-neutron halo. *Nucl. Phys. A*, 575:125, 1994.

[6] E. Arnold, J. Bonn, R. Gegenwart, W. Neu, R. Neugart, E.-W. Otten, G. Ulm, K. Wendt, and the ISOLDE Collaboration. Nuclear spin and magnetic moment of ^{11}Li. *Phys. Lett. B*, 197(3):311–314, 1987.

[7] E. Arnold, J. Bonn, A. Klein, R. Neugart, M. Neuroth, E. W. Otten, P. Lievens, H. Reich, W. Widdra, and the ISOLDE Collaboration. Quadrupole moment of ^{11}Li. *Phys. Lett. B*, 281:16–19, 1992.

[8] G. Audi, O. Bersillon, J. Blachot, and A. H. Wapstra. The NUBASE evaluation of nuclear and decay properties. *Nucl. Phys. A*, 624:1, 1997.

[9] L. Axelsson, M. J. G. Borge, S. Fayans, V. Z. Goldberg, S. Grévy, D. Guillemaud-Mueller, B. Jonson, K.-M. Källman, T. Lönnroth, M. Lewitowicz, P. Manngård, K. Markenroth, I. Martel, A. C. Mueller, I. Mukha, T. Nilsson, G. Nyman, N. A. Orr, K. Riisager, G. V. Rogatchev, M.-G. Saint-Laurent, I. N. Serikov, O. Sorlin, O. Tengblad, F. Wenander, J. S. Winfield, and R. Wolski. Study of the unbound nucleus ^{11}N by elastic resonance scattering. *Phys. Rev. C*, 54(4):R1511–R1514, Oct. 1996.

[10] T. Baumann, M. J. G. Borge, H. Geissel, H. Lenske, K. Markenroth, W. Schwab, M. H. Smedberg, T. Aumann, L. Axelsson, U. Bergmann, D. Cortina-Gil, L. Fraile, M. Hellström, M. Ivanov, N. Iwasa, R. Janik, B. Jonson, G. Münzenberg, F. Nickel, T. Nilsson, A. Ozawa, A. Richter, K. Riisager, C. Scheidenberger, G. Schrieder, H. Simon, B. Sitar, P. Strmen, K. Sümmerer, T. Suzuki, M. Winkler, H. Wollnik, and M. V. Zhukov. Longitudinal momentum distributions of ^{16,18}C fragments after one-neutron removal from ^{17,19}C. *Phys. Lett. B*, 439:256–261, Nov. 1998.

[11] T. Baumann, H. Geissel, H. Lenske, K. Markenroth, T. Aumann, L. Axelsson, U. Bergmann, D. Cortina-Gil, L. Fraile, M. Hellström, M. Ivanov, N. Iwasa, R. Janik, B. Jonson, G. Münzenberg, F. Nickel, T. Nilsson, A. Ozawa, A. Richter, K. Riisager, C. Scheidenberger, G. Schrieder, W. Schwab, H. Simon, B. Sitar, M. H. Smedberg, P. Strmen, K. Sümmerer, T. Suzuki, M. Winkler, and M. V. Zhukov. Probing the nuclear structure of ^{8}B and ^{19}C. In *Proceedings of the 2nd International Conference on Exotic Nuclei and Atomic Masses, ENAM98*. American Institute of Physics, 1998. To be published.

[12] T. Baumann, V. Hlinka, M. Ivanov, R. Janik, L. Lúčan, W. Schwab, B. Sitár, P. Strmeň, and I. Szarka. Development of TPC for heavy ion tracking. *Acta Physica Universitatis Comenianae*, XXXVII:3–18, 1996.

[13] D. Bazin, W. Benenson, B. A. Brown, J. Brown, B. Davids, M. Fauerbach, P. G. Hansen, P. Mantica, D. J. Morrissey, C. F. Powell, B. M. Sherrill, and M. Steiner. Probing the halo structure of ^{19,17,15}C and ^{14}B. *Phys. Rev. C*, 57(5):2156, 1998.

[14] D. Bazin, B. A. Brown, J. Brown, M. Fauerbach, M. Hellström, S. E. Hirzebruch, J. H. Kelley, R. A. Kryger, D. J. Morrissey, R. Pfaff, C. F. Powell, B. M. Sherrill, and M. Thoennessen. One-neutron halo of ^{19}C. *Phys. Rev. Lett.*, 74(18):3569, May 1995.

[15] C. A. Bertulani and G. Baur. Electromagnetic processes in relativistic heavy ion collisions. *Phys. Reports*, 163(5,6):299–408, 1988.

[16] T. Bjerge and K. J. Broström. *Nature*, 138:400, 1936.

[17] B. Blank, J.-J. Gaimard, H. Geissel, K.-H. Schmidt, H. Stelzer, K. Sümmerer, D. Bazin, R. D. Moral, J. P. Dufour, A. Fleury, F. Hubert, H.-G. Clerc, and M. Steiner. Charge-changing cross sections of the neutron-rich isotopes ^{8,9,11}Li. *Z. Phys. A*, 343:375–379, 1992.

[18] B. Blank, C. Marchand, M. S. Pravikoff, T. Baumann, F. Boué, H. Geissel, M. Hellström, N. Iwasa, W. Schwab, K. Sümmerer, and M. Gai. Total interaction and proton-removal cross-section measurements for the proton-rich isotopes ^{7}Be, ^{8}B, and ^{9}C. *Nucl. Phys. A*, 624:242–256, 1997.

[19] M. J. G. Borge, J. Deding, P. G. Hansen, B. Jonson, G. Martínez Pinedo, P. Møller, G. Nyman, A. Poves, A. Richter, K. Riisager, O. Tengblad, and the ISOLDE Collaboration. Beta-decay to the proton halo state in ^{17}F. *Phys. Lett. B*, 317:25–30, 1993.

[20] C. Brendel, P. von Neumann-Cosel, A. Richter, G. Schrieder, H. Lenske, H. H. Wolter, J. Carter, and D. Schull. Quasi-elastic nucleon transfer and single charge exchange in ^{48}Ti + ^{42}Ca collisions. *Nucl. Phys. A*, 477:162, 1988.

[21] L. V. Chulkov, T. Aumann, D. Aleksandrov, L. Axelsson, T. Baumann, M. J. G. Borge, R. Collatz, J. Cub, W. Dostal, B. Eberlein, Th. W. Elze, H. Emling, H. Geissel, V. Z. Goldberg, M. Golovkov, A. Grünschloß, M. Hellström, J. Holeczek, R. Holzmann, B. Jonson, A. A. Korsheninnikov, J. V. Kratz, G. Kraus, R. Kulessa, Y. Leifels, A. Leistenschneider, T. Leth, I. Mukha, G. Münzenberg, F. Nickel, T. Nilsson, G. Nyman, B. Petersen, M. Pfützner, A. Richter, K. Riisager, C. Scheidenberger, G. Schrieder, W. Schwab, H. Simon, M. H. Smedberg, M. Steiner, J. Stroth, A. Surowiec, T. Suzuki, and O. Tengblad. Large spin alignment of the unbound ^{5}He fragment after fragmentation of 240 MeV/nucleon ^{6}He. *Phys. Rev. Lett.*, 79(2):201–204, July 1997.

[22] D. Cortina-Gil, 1999. Private communication.

[23] F. J. Eckle, H. Lenske, G. Eckle, G. Graw, R. Hertenberger, H. Kader, H. J. Maier, F. Merz, H. Nann, P. Schiemenz, and H. H. Wolter. Investigation of single-particle strength distributions in a high-resolution ^{40}Ca($\vec{\mathrm{d}}$,p) study at $E_{\mathrm{d}} = 20$ MeV. *Nucl. Phys. A*, 506:159, 1990.

[24] F. J. Eckle, H. Lenske, G. Eckle, G. Graw, R. Hertenberger, H. Kader, F. Merz, H. Nann, P. Schiemenz, and H. H. Wolter. Single-particle strength distributions in ^{41}Ca. *Phys. Rev. C*, 39:1662, 1989.

[25] H. Esbensen. Momentum distributions in stripping reactions of single-nucleon halo nuclei. *Phys. Rev. C*, 53(4):2007–2010, Apr. 1996.

[26] H. Esbensen, B. A. Brown, and H. Sagawa. Positive parity states in ^{11}Be. *Phys. Rev. C*, 51:1274, 1995.

[27] H. Geissel. Relativistische exotische Kerne als Projektilstrahlen; Neue Perspektiven zum Studium der Kerneigenschaften. GSI Report 97-03, Gesellschaft für Schwerionenforschung, 1997.

[28] H. Geissel, P. Armbruster, K. H. Behr, A. Brünle, K. Burkard, M. Chen, H. Folger, B. Franczak, H. Keller, O. Klepper, B. Langenbeck, F. Nickel, E. Pfeng, M. Pfützner, E. Roeckl, K. Rykaczewski, I. Schall, D. Schardt, C. Scheidenberger, K.-H. Schmidt, A. Schröter, T. Schwab, K. Sümmerer, M. Weber, G. Münzenberg, T. Brohm, H.-G. Clerc, M. Fauerbach, J.-J. Gaimard, A. Grewe, E. Hanelt, B. Knödler, M. Steiner, B. Voss, J. Weckenmann, C. Ziegler, A. Magel, H. Wollnik, J. P. Dufour, Y. Fujita, D. J. Viera, and B. Sherrill. The GSI projectile fragment separator (FRS): A versatile magnetic system for relativistic heavy ions. *Nucl. Instr. and Meth.*, B 70:286, 1992.

[29] H. Geissel, G. Münzenberg, and K. Riisager. Secondary exotic nuclear beams. *Annu. Rev. Nucl. Part. Sci.*, 45:163–203, 1995.

[30] W. Gelletly. Broken halo reveals all. *Nature*, 376:119, 1995.

[31] A. S. Goldhaber. Statistical models of fragmentation processes. *Phys. Lett. B*, 53(4):306–308, Dec. 1974.

[32] L. V. Grigorenko, B. V. Danilin, V. D. Efros, N. B. Shul'gina, and M. V. Zhukov. Structure of the ^{8}Li and ^{8}B nuclei in an extended three-body model and astrophysical S_{17} factor. *Phys. Rev. C*, 57:R2099, 1998.

[33] P. G. Hansen. Nuclear structure at the drip lines. *Nucl. Phys. A*, 553:89c–106c, 1993.

[34] P. G. Hansen. Momentum content of single-nucleon halos. *Phys. Rev. Lett.*, 77(6):1016–1019, Aug. 1996.

[35] P. G. Hansen, A. S. Jensen, and B. Jonson. Nuclear halos. *Annu. Rev. Nucl. Part. Sci.*, 45:591–634, 1995.

[36] P. G. Hansen and B. Jonson. The neutron halo of extremely neutron-rich nuclei. *Europhys. Lett.*, 4:409–414, 1987.

[37] J. Hüfner and M. C. Nemes. Relativistic heavy ions measure the momentum distribution on the nuclear surface. *Phys. Rev. C*, 23(6):2538–2547, June 1981.

[38] N. Iwasa, H. Geissel, G. Münzenberg, C. Scheidenberger, Th. Schwab, and H. Wollnik. MOCADI, a universal Monte Carlo code for the transport of heavy ions through matter within ion-optical systems. *Nucl. Instr. and Meth.*, B 126:284, 1997.

[39] J. H. Kelley, S. M. Austin, A. Azhari, D. Bazin, J. A. Brown, H. Esbensen, M. Fauerbach, M. Hellström, S. E. Hirzebruch, R. A. Kryger, D. J. Morrissey, R. Pfaff, C. F. Powell, E. Ramakrishnan, B. M. Sherrill, M. Steiner, T. Suomijärvi, and M. Thoennessen. Study of the breakup reaction ^{8}B $\rightarrow$ ^{7}Be + p: Absorption effects and $E2$ strength. *Phys. Rev. Lett.*, 77(25):5020–5023, 1996.

[40] J. M. Kidd, P. J. Lindstrom, H. J. Crawford, and G. Woods. Fragmentation of carbon ions at 250 MeV/nucleon. *Phys. Rev. C*, 37(6):2613–2622, 1988.

[41] R. Klapisch, C. Thibault-Philippe, C. Detraz, J. Chaumont, R. Bernas, and E. Beck. Half-life of ^{11}Li, of ^{27}Na, and of the new isotopes ^{28}Na, ^{29}Na, ^{30}Na, and ^{31}Na produced in high-energy nuclear reactions. *Phys. Rev. Lett.*, 23:652, 1969.

[42] T. Kobayashi, O. Yamakawa, K. Omata, K. Sugimoto, T. Shimoda, N. Takahashi, and I. Tanihata. Projectile fragmentation of the extremely neutron-rich nucleus ^{11}Li at 0.79 GeV/nucleon. *Phys. Rev. Lett.*, 60(25):2599–2602, 1988.

[43] O. Kofoed-Hansen and K. O. Nielsen. *K. Dan. Vidensk. Selsk. Mat. Fys. Medd.*, 26(7), 1951.

[44] A. A. Korsheninnikov, E. Y. Nikolskii, T. Kobayashi, A. Ozawa, S. Fukuda, E. A. Kuzmin, S. Momota, B. G. Novatskii, A. A. Ogloblin, V. Pribora, I. Tanihata, and K. Yoshida. Spectroscopy of the halo nucleus ^{11}Li by an experimental study of ^{11}Li + p collisions. *Phys. Rev. C*, 53(2):R537–R540, Feb. 1996.

[45] R. A. Kryger, A. Azhari, A. Galonsky, J. H. Kelley, R. Pfaff, E. Ramakrishnan, D. Sackett, B. M. Sherrill, M. Thoennessen, J. A. Winger, and S. Yokoyama. Neutron decay of ^{10}Li produced by fragmentation. *Phys. Rev. C*, 47:R2439, 1993.

[46] H. Lenske, 1998. Private communication.

[47] H. Lenske. Structure and reactions of exotic nuclei. *J. Phys. G*, 24:1429–1438, 1998.

[48] H. Lenske and G. Schrieder. Probing the structure of exotic nuclei by transfer reactions. *Eur. Phys. J. A.*, 2:41–53, 1998.

[49] K. R. Lykke, R. D. Mead, and W. C. Lineberger. Observation of dipole-bound states of negative ions. *Phys. Rev. Lett.*, 52(25):2221–2224, June 1984.

[50] F. M. Marqués, E. Liegard, N. A. Orr, J. C. Angélique, L. Axelsson, G. Bizard, W. N. Catford, N. M. Clarke, G. Costa, M. Freer, S. Grévy, D. Guillemaud-Mueller, G. J. Gyapong, F. Hanappe, P. G. Hansen, B. Heusch, B. Jonson, C. L. Brun, F. R. Lecolley, F. Lefebvres, M. Lewitowicz, G. Martínez, A. C. Mueller, T. Nilsson, A. Ninane, G. Nyman, B. Petersen, F. Pougheon, K. Riisager, M. G. Saint-Laurent, Y. Schutz, M. Smedberg, O. Sorlin, L. Stuttgé, and D. D. Warner. Neutrons from the breakup of ^{19}C. *Phys. Lett. B*, 381:407, 1996.

[51] D. J. Millener, J. W. Olness, E. K. Warburton, and S. S. Hanna. Strong $E1$ transitions in ^{9}Be, ^{11}Be, and ^{13}C,. *Phys. Rev. C*, 28(2):497–505, Aug. 1983.

[52] T. Minamisono, T. Ohtsubo, I. Minami, S. Fukuda, A. Kitagawa, M. Fukuda, K. Matsuta, Y. Nojiri, S. Takeda, H. Sagawa, and H. Kitagawa. Proton halo of ^{8}B disclosed by its giant quadrupole moment. *Phys. Rev. Lett.*, 69(14):2058–2061, 1992.

[53] E. J. Moniz, I. Sick, R. R. Whitney, J. R. Ficenec, R. D. Kephart, and W. P. Trower. Nuclear Fermi momenta from quasielastic electron scattering. *Phys. Rev. Lett.*, 26(8):445–448, 1998.

[54] R. Morlock, R. Kunz, A. Mayer, M. Jaeger, A. Müller, J. W. Hammer, P. Mohr, H. Oberhummer, G. Staudt, and V. Kölle. Halo properties of the first $1/2^+$ state in ^{17}F from the ^{16}O(p,γ)^{17}F reaction. *Phys. Rev. Lett.*, 79(20):3837, 1997.

[55] H. Nakada and T. Otsuka. $E2$ properties of nuclei far from stability and the proton-halo problem of ^{8}B. *Phys. Rev. C*, 49(2):886–894, 1994.

[56] T. Nakamura, T. Motobayashi, Y. Ando, A. Mengoni, T. Nishio, H. Sakurai, S. Shimoura, T. Teranishi, Y. Yanagisawa, and M. Ishihara. Coulomb excitation of ^{11}Be. *Phys. Lett. B*, 394:11, 1997.

[57] F. Negoita, C. Borcea, F. Carstoiu, M. Lewitowicz, M. G. Saint-Laurent, R. Anne, D. Bazin, J. M. Corre, P. Roussel-Chomaz, V. Borrel, D. Guillemaud-Mueller, H. Keller, A. C. Mueller, F. Pougheon, O. Sorlin, S. Lukyanov, Yu. Penionzhkevich, A. Fomichev, N. Skobelev,

O. Tarasov, Z. Dlouhy, and A. Kordyasz. ^{8}B proton halo via reaction and breakup cross section measurement. *Phys. Rev. C*, 54(4):1787–1797, 1996.

[58] P. V. Neumann-Cosel, A. Richter, H.-J. Schmidt-Brucken, G. Schrieder, H. Lenske, H. H. Wolter, J. Carter, R. Jahn, B. Kohlmeyer, and D. Schull. Quasi-elastic single-nucleon transfer in ^{48}Ti + ^{42,44}Ca collisions well above the Coulomb barrier. *Nucl. Phys. A*, 516:385, 1990.

[59] F. M. Nunes, I. J. Thompson, and R. C. Johnson. Core excitation in one neutron halo systems. *Nucl. Phys. A*, 596:171, 1996.

[60] I. Pecina, R. Anne, D. Bazin, C. Borcea, V. Borrel, F. Carstoiu, J. M. Corre, Z. Dlouhy, A. Fomitchev, D. Giullemaud-Mueller, H. Keller, A. Kordyasz, M. Lewitowicz, S. Lukyanov, A. C. Mueller, Y. Penionzhkevich, P. Roussel-Chomaz, M. G. Saint-Laurent, N. Skobelev, O. Sorlin, and O. Tarasov. Quasielastic scattering of ^{8}B and ^{7}Be on ^{12}C at 40 MeV/nucleon. *Phys. Rev. C*, 52(1):191–198, July 1996.

[61] M. Pfützner, H. Geissel, G. Münzenberg, F. Nickel, Ch. Scheidenberger, K.-H. Schmidt, K. Sümmerer, T. Brohm, B. Voss, and H. Bichsel. Energy deposition by relativistic heavy ions in thin argon absorbers. *Nucl. Instr. and Meth.*, B 86:213–218, 1994.

[62] A. M. Poskanser, S. W. Cosper, E. K. Hyde, and J. Cerny. New isotopes: ^{11}Li, ^{14}B, and ^{15}B. *Phys. Rev. Lett.*, 17:1271, 1966.

[63] D. Ridikas, M. H. Smedberg, J. S. Vaagen, and M. V. Zhukov. ^{19}C: the heaviest one-neutron halo nucleus? *Europhys. Lett.*, 37:385, 1997.

[64] D. Ridikas, M. H. Smedberg, J. S. Vaagen, and M. V. Zhukov. Exploratory coupled channels calculations for loosely bound carbon isotopes. *Nucl. Phys. A*, 628:363, 1998.

[65] D. Ridikas, J. S. Vaagen, and J. M. Bang. Phase equivalent potentials for one-neutron halo systems. *Nucl. Phys. A*, 609:21, 1996.

[66] K. Riisager. Nuclear halo states. *Rev. Mod. Phys.*, 66(3):1105–1116, July 1994.

[67] K. Riisager, M. J. G. Borge, H. Gabelmann, P. G. Hansen, L.Johannsen, B. Jonson, W. Kurcewicz, G. Nyman, A. Richter, and O. Tengblad. First observation of beta-delayed deuteron emission. *Phys. Lett. B*, 235(1,2):30–34, 1990.

[68] C. Schaerf and R. Scrimaglio. High resolution energy loss magnetic analyser for scattering experiments. *Nucl. Instr. and Meth.*, 30:359–360, 1964.

[69] C. Scheidenberger, Th. Stöhlker, W. E. Meyerhof, H. Geissel, P. H. Mokler, and B. Blank. Charge states of relativistic heavy ions in matter. *Nucl. Instr. and Meth.*, B 142:441–462, 1998.

[70] W. Schwab, H. Geissel, H. Lenske, K.-H. Behr, A. Brünle, K. Burkard, H. Irnich, T. Kobayashi, G. Kraus, A. Magel, G. Münzenberg, F. Nickel, K. Riisager, C. Scheidenberger, B. M. Sherrill, T. Suzuki, and B. Voss. Observation of a proton halo in ^{8}B. *Z. Phys. A*, 350:283–284, 1995.

[71] R. Serber. The production of high energy neutrons by stripping. *Phys. Rev.*, 72:1008–1016, 1947.

[72] M. Smedberg. *Probing the drip-line through momentum distributions.* PhD thesis, Department of Experimental Physics, Chalmers University of Technology, Göteborg University, 1998.

[73] M. H. Smedberg, T. Baumann, T. Aumann, L. Axelsson, U. Bergmann, M. J. G. Borge, D. Cortina-Gil, L. Fraile, H. Geissel, L. Grigorenko, M. Hellström, M. Ivanov, N. Iwasa, R. Janik, B. Jonson, H. Lenske, K. Markenroth, G. Münzenberg, T. Nilsson, A. Richter, K. Riisager, C. Scheidenberger, G. Schrieder, W. Schwab, H. Simon, B. Sitar, P. Strmen, K. Sümmerer, M. Winkler, and M. V. Zhukov. New results on the halo structure of ^{8}B. *Phys. Lett. B*, 452:1–7, 1999.

[74] M. H. Smedberg and M. V. Zhukov. Effects of a low-lying resonance in ^{19}C on the ^{18}C momentum distribution after fragmentation. Technical Report CTHSP-98/06, Department of Physics, Chalmers University of Technology, Göteborg University, Nov. 1998. Submitted to *Phys. Rev. C.*

[75] T. J. M. Symon, Y. P. Viyogi, G. D. Westfall, P. Doll, D. E. Greiner, H. Faraggi, P. J. Lindstrom, D. K. Scott, H. J. Crawford, and C. McParland. Observation of new neutron-rich isotopes by fragmentation of 205-MeV/nucleon ^{40}Ar ions. *Phys. Rev. Lett.*, 42:40, 1979.

[76] I. Tanihata, H. Hamagaki, O. Hashimoto, S. Nagamiya, Y. Shida, N. Yoshikawa, O. Yamakawa, K. Sugimoto, T. Kobayashi, D. Greiner, N. Takahashi, and Y. Nojiri. Measurements of interaction cross sections and radii of He isotopes. *Phys. Lett. B*, 160(6):380–384, 1985.

[77] I. Tanihata, H. Hamagaki, O. Hashimoto, Y. Shida, N. Yoshikawa, K. Sugimoto, O. Yamakawa, T. Kobayashi, and N. Takahashi. Measurements of interaction cross sections and nuclear radii in the light p-shell region. *Phys. Rev. Lett.*, 55(24):2676–2679, Dec. 1985.

[78] I. Tanihata, D. Hirata, T. Kobayashi, S. Shimoura, K. Sugimoto, and H. Toki. Revelation of thick neutron skins in nuclei. *Phys. Lett. B*, 289:261, 1992.

[79] I. Tanihata, T. Kobayashi, O. Yamakawa, S. Shimoura, K. Ekuni, K. Sugimoto, N. Takahashi, T. Shimoda, and H. Sato. Measurement of interaction cross sections using isotope beams of Be and B and isospin dependence of the nuclear radii. *Phys. Lett. B*, 206(4):592–596, 1988.

[80] N. Vinh Mau. Particle-vibration coupling in one neutron halo nuclei. *Nucl. Phys. A*, 592:33, 1995.

[81] R. E. Warner, J. H. Kelley, P. Zecher, F. D. Bechetti, J. A. Brown, C. L. Carpenter, A. Galonsky, J. Kruse, A. Muthukrishnan, A. Nadasen, R. M. Ronningen, P. Schwandt, B. M. Sherrill, J. Wang, and J. S. Winfield. Evidence for a proton halo in ^{8}B: Enhanced total reaction cross sections at 20 to 60 MeV/nucleon. *Phys. Rev. C*, 52(3):R1166–R1169, 1995.

[82] G. D. Westfall, T. J. M. Symons, D. E. Greiner, H. H. Heckman, P. J. Lindstrom, J. Mahoney, A. C. Shotter, D. K. Scott, H. J. Crawford, C. McParland, T. C. Awes, C. K. Gelbke, and J. M. Kidd. Production of neutron-rich nuclides by fragmentation of 212 MeV/amu ^{48}Ca. *Phys. Rev. Lett.*, 43:1859, 1979.

[83] H. Wollnik. *Optics of charged particles.* Academic Press, Inc., 1987.

[84] T. Yamazaki, R. S. Hayano, K. Itahashi, K. Oyama, A. Gillitzer, H. Gilg, M. Knülle, M. Münch, P. Kienle, W. Schott, H. Geissel, N. Iwasa, and G. Münzenberg. Discovery of deeply bound π^- states in the ^{208}Pb(d,^{3}He) reaction. *Z. Phys. A*, 355:219–221, 1996.

[85] M. Zinser, F. Humbert, T. Nilsson, W. Schwab, H. Simon, T. Aumann, M. J. G. Borge, L. V. Chulkov, J. Cub, Th. W. Elze, H. Emling, H. Geissel, D. Guillemaud-Mueller, P. G. Hansen, R. Holzmann, H. Irnich, B. Jonson, J. V. Kratz, R. Kulessa, Y. Leifels, H. Lenske, A. Magel, A. C. Mueller, G. Münzenberg, F. Nickel, G. Nyman, A. Richter, K. Riisager, C. Scheidenberger, G. Schrieder, K. Stelzer, J. Stroth, A. Surowiec, O. Tengblad, E. Wajda, and E. Zude. Invariant-mass spectroscopy of ^{10}Li and ^{11}Li. *Nucl. Phys. A*, 619:151, 1997.

[86] M. Zinser, F. Humbert, T. Nilsson, W. Schwab, Th. Blaich, M. J. G. Borge, L. V. Chulkov, Th. W. Elze, H. Emling, H. Freiesleben, H. Geissel, K. Grimm, D. Guillemaud-Mueller, P. G. Hansen, R. Holzmann, H. Irnich, B. Jonson, J. G. Keller, H. Klingler, J. V. Kratz, R. Kulessa, D. Lambrecht, Y. Leifels, A. Magel, M. Mohar, A. C. Mueller, G. Münzenberg, F. Nickel, G. Nyman, A. Richter, K. Riisager, C. Scheidenberger, G. Schrieder, B. M. Sherrill, H. Simon, K. Stelzer, J. Stroth, O. Tengblad, W. Trautmann, E. Wajda, and E. Zude. Study of the unstable nucleus ^{10}Li in stripping reactions of the radioactive projectiles ^{11}Be and ^{11}Li. *Phys. Rev. Lett.*, 75(9):1719–1722, 1995.

Acknowledgements

I would like to thank first of all Hans Geissel for his large personal effort. Without him the experiments that this work is based on would not have been possible. I gratefully recognize the guidance of this thesis by Hermann Wollnik, and I appreciate his advice from many conversations. I also want to thank Gottfried Münzenberg, who was always very supportive and who provides a welcoming atmosphere for the KP2 department.

The research that went into this work was supported by a large number of people. I would like to mention here Horst Lenske and thank him for his theoretical input and the many helpful discussions I had with him. I am very thankful to Björn Jonson for his guidance of our collaboration and the support I received from him. Thank you, Martin Smedberg, for your contribution to this work!

I want to thank Dolores Cortina-Gil for her contribution to the experiment and the analysis and for her encouragement during the writing of this thesis. Thank you Wolfgang Schwab for helping me to get a start and for your continued interest. I have to thank Marian Ivanov and the team from Bratislava for their technical contribution. And thank you to all other collaborators who have put their effort into this work!

I am grateful of having been able to work in a team of very helpful and encouraging colleagues. I have to mention here Frédéric Boué, Marc Hausmann, Frank Nickel, Torsten Radon, Christoph Scheidenberger, Klaus Sümmerer, and Helmut Weick.

I could always get help concerning technical questions from Karl-Heinz Behr, Adolf Brünle, and Karlheinz Burkhard, whom I want to thank here. This list would be incomplete without thanking Siggi Raiss for being much more than a secretary! I am indebted to many others who work at GSI and who helped me during my stay. And I want to thank all those who I became friends with, for sharing their language and their culture with me. Without you, GSI would not be as enjoyable as it is!

Finally, I have to thank Krista, for she gave me strong encouragement and a big support throughout the complete time I spent on this work. And I have to thank her for proof-reading this thesis!